A THEORETICAL AND COMPUTATIONAL STUDY OF THE INTERACTION BETWEEN BIOMEMBRANES AND CURVED PROTEINS

Caterina Tozzi

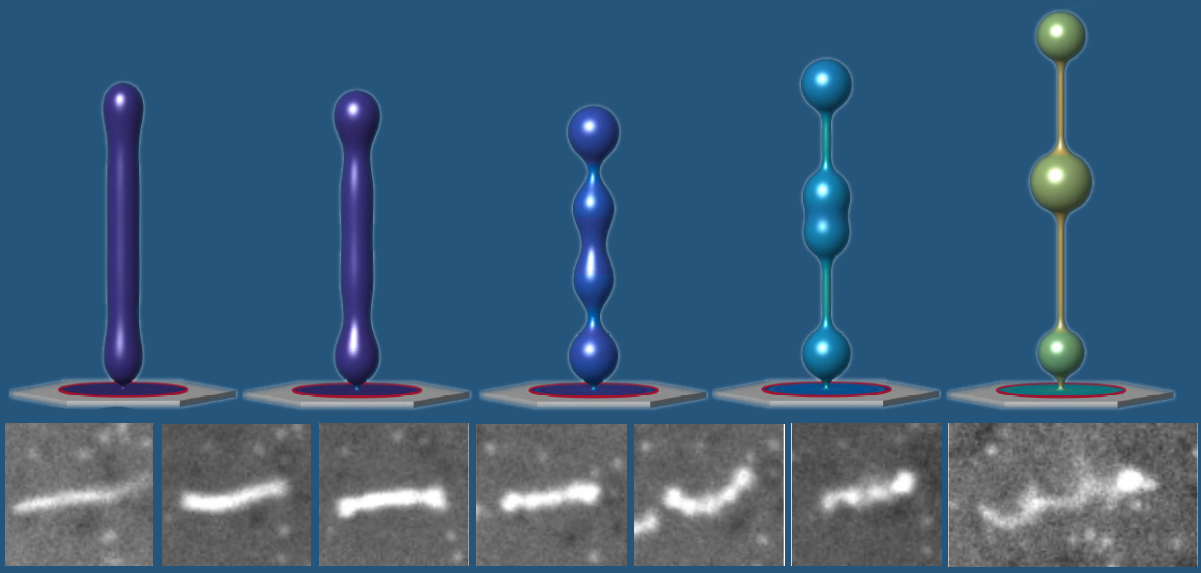

Doctoral Thesis
Barcelona, April 2021

A THEORETICAL AND COMPUTATIONAL STUDY OF THE INTERACTION BETWEEN BIOMEMBRANES AND CURVED PROTEINS

Caterina Tozzi

Doctoral Thesis
Advisor: Marino Arroyo
Barcelona, April 2021

Departament d'Enginyeria Civil i Ambiental
Programa de Doctorat de Matemàtica Aplicada

Abstract

A theoretical and computational study of the mechanics of biomembranes interacting with curved proteins

Caterina Tozzi

Organelles are the smallest functional parts of eukaryotic cells. Among them, some are membrane-bound such as the nucleus, the endoplasmic reticulum, or the Golgi apparatus, each of them with essential biological functions. In order to accomplish cell functions, membranes enclosing these organelles continuously adapt their shapes through the out-of-equilibrium interaction with macro-molecules, notably proteins.

During the life of cells, proteins are main actors in membrane bending dynamics since they have the ability to impinge their curvature onto the membrane, and generate transiently highly curved structures, such as tubes and spherical buds. How proteins can remodel the different organelles has been broadly studied in equilibrium, but a clear understanding of the complex chemo-mechanical problem that drives membrane reshaping out-of-equilibrium is still lacking.

In the first Part of the thesis we develop a general theoretical and computational framework for the dynamics of curved proteins adhered to lipid membranes. The theory is based on a nonlinear Onsager's principle, a variational method for irreversible thermodynamics. The resulting governing equations and numerical simulations provide a foundation to understand the dynamics of curvature sensing, curvature generation, and more generally membrane curvature mechano-chemistry, as illustrated by a selection of test cases. We show that continuum modeling is a powerful instrument to describe the protein-membrane interaction. However, this model does not account for the orientational order of proteins and its derivation lacks a microscopic basis.

To address these limitations, in the second Part of the thesis we develop a mean-field density functional theory to predict the orientational order and evaluate the free-energy of ensembles of elongated and curved objects, such

as BAR proteins, on curved membranes. This kind of protein may adopt different states of orientational order, from isotropic to nematic. The theory is tightly coupled to the microscopic properties of the proteins and explains how a density-dependent isotropic-to-nematic transition is modified by the anisotropic underlying curvature of the membrane. This work lays the ground to understand the interplay between the molecular organization of proteins and the membrane shape dynamics. We explore the coexistence of isotropic and nematic phases on differently curved lipid membranes. We explain, both experimentally and through modelling, how a BAR protein binds on differently curved membrane templates and reshapes them based while modifying their microscopic organization. Our results broaden our understanding of the reshaping dynamics by BAR proteins on mechanically constrained membranes, and provide a framework to understand biological responses involving BAR proteins to membrane-mediated mechanical stimuli.

Contents

List of Figures

Chapter 1

Introduction

Lipid membranes and intrinsically-curved proteins

Cells are complex structures based on a hierarchical compartmentalisations into subunits, called organelles, which play specialised biological functions, such as the nucleus, the Golgi apparatus, the endoplasmic reticulum or mitochondria [3]. The organelles compartmentalisation is supported by lipid membranes, soft materials made of lipids that when exposed to water self-assemble into two specular sheets, where the hydrophobic tails of lipids are directed to the center of the bilayer and the hydrophilic phosphate head points to the external environment (see Fig. 1.1). The thickness of these structures ranges between 2 and 5 nm, equivalent to the length of two lipids, while on the other dimension they can range from 100nm, in cases of small vesicles, to 100 μm, in large eukaryotic cells. Because of this size discrepancy, lipid bilayers can be modeled as continuous surfaces. Often, lipid bilayers organise in spherical structures called vesicles, although they equally assume shapes with higher degree of topological complexity [4]. Lipid membranes are semi-permeable layers that mechanically confine the organelles from the cytoplasm and the cell from the exterior environment and simultaneously regulate the chemical exchanges at cellular and subcellular scales. In living cells, lipid

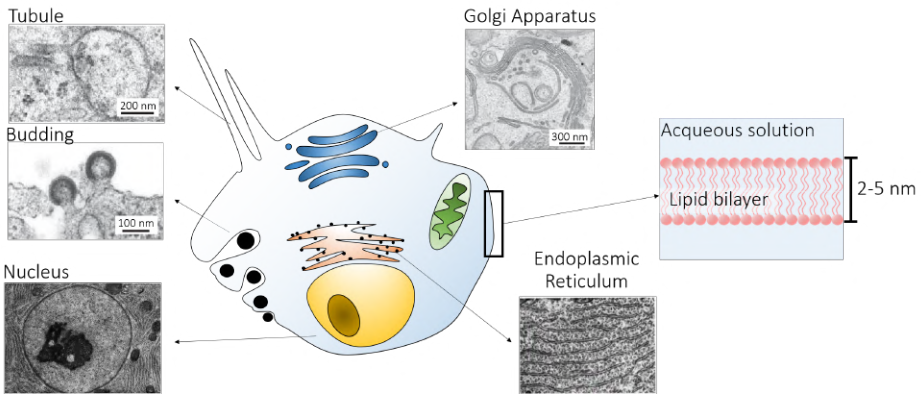

Figure 1.1: A schematic view of the different organelles and membrane structures that we can find in cells (center), and transmission electron micrographs of some of them. Nucleus and Endoplasmic Reticulum from "The Cell, 2nd Edition by Don W. Fawcett". Mitochondria from "Molecular biology of the cell, 6th edition by Bruce Alberts". Golgi Apparatus from "Membrane curvature and mechanisms of dynamic cell membrane remodelling, Nature by McMahon and Gallop". Cartoon to zoom into the specular layers composing the lipid membrane.

membranes also fulfil a mechanical role dynamically regulating their shapes in order to accommodate external stimuli and internal cell functions such as vesicular transport, cell division or to unfold membrane reservoirs under stress [5]. The ability of membranes to provide adaptability and stability during the dynamic shape transformations derives from their mechanical duality. On one hand their fluid composition preserves their integrity during the remodelling. Indeed lipids can easily flow and tilt, distributing inohomogeneously between the two leaflets of the membrane during reshaping. On the other hand, out of plane, membranes accommodate deformation in the form of bending and stretching, like elastic solid shells [6]. Cytoskeletal dynamics, changes of pH in the surrounding environment [7] or protein recruitments can be the onset for lipid unbalance between the two monolayers forming defects and a consequent membrane bending [8]. In some cases the shape changes are drastic and permanent as the case of microvilli or the dendritic tree, but usually highly curved membrane features last for a limited period of time, as the case of

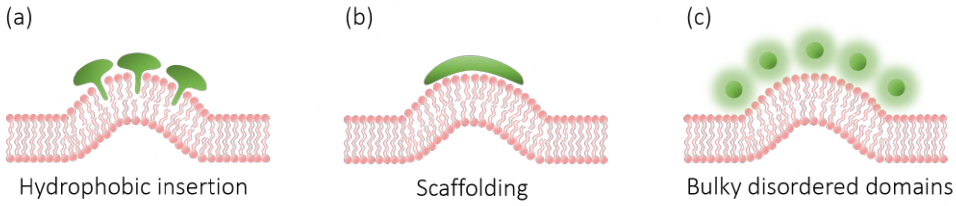

Figure 1.2: The phospholipid bilayer is shaped by protein interaction. (a) Hydrophobic insertion, (b) scaffolding of intrinsically curved proteins, (c) entropic repulsion of bulky disordered domains.

vesicular trafficking or caveolar structures, where intrinsically curved proteins impinge their curvatures on the membrane. Under specific cell needs, proteins can assemble and form a protein coat able to generate local membrane curvature and temporarily stabilize highly curved shapes, as tubular structures [9] or caveolae necks [10], and later disassemble when the proteins coat dissolves. Proteins can curve lipid membranes through different mechanisms, one is through wedge-like hydrophobic insertions into the upper part of one of the monolayer, that induces a packing imbalance between the monolayers and favore bending [11, 12, 8]. Another mechanism by which a protein or a protein coat impinge high curvature on a surface is by scaffolding, where two necessary conditions to force the membrane bending are strong affinity of the proteins with the polar head of the lipids, so that the proteins-membrane binding energy exceeds the membrane-bending energy, and bending rigidity of the protein coat to be stronger then the membrane bending rigidity [4]. Other mechanisms by which proteins bend membranes are related to asymmetrical crowding of bulky disordered domains [13], where the entropic proteins interaction induces bending to reduce the crowding of proteins, or to anchored polymers [14] as in the glycocalyx [15] interacting at a distance from the bilayer mid-plane (see Fig. 1.2).

Highly nonlinear membrane chemo-mechanics

As argued above the interaction between membrane and curved proteins poses an intriguing chemo-mechanical problem: the membrane experiences drastic changes in shape implicating nonlinear geometries, while membrane hydrodynamics and other chemical inputs, as proteins sorption or crowding, elicit chemical nonlinearity. All these processes are tightly coupled between them and act at the same time, leading to a highly nonlinear chemo-mechanical problem. To better understand the dynamics behind this interplay many biophysical studies have been performed under controlled conditions, where artificial lipid membranes were exposed to purified proteins [16]. At low proteins concentration it has been observed that proteins can sense curvature and preferentially bind or diffuse to particular membrane curvature [17] as probed in assays involving polydisperse vesicle suspensions [18], vesicles with membrane tethers [19, 20] or supported lipid bilayers on wavy substrates [21]. At higher concentration, proteins can impinge their curvature on the lipid membrane driving curvature generation, when incubated with liposomes [9], can stabilise membrane tubes [13, 22], and can dynamically trigger protein-rich tubular protrusions out of tense vesicles [23, 20, 24]. The ability of proteins to *sense* and *generate curvature* is also related with the mechanical state of the membrane. The shape transformations induced by protein binding require a buffer of area from the adjacent membrane and the curvature generation process works against the membrane tension and can be inhibited when the membrane tension is large enough. This kind of mechano-chemical coupling, tested in-vitro by exposing aspirated vesicles to BAR proteins [24], has physiological implications during the mechano-protection of stressed cells by the release of membrane area through disassembly of caveolae [5], or in the regulation of clathrin-mediated endocytosis by membrane tension [25].

BAR domains, a special class of proteins

Some curved proteins such as those containing the BAR domain (Amphiphysin, Endophilin, F-CHo) and others like dynamin, EHD2, etc. are called "banana shaped" because they are curved and elongated. These specific proteins can impinge anisotropic curvatures on the membranes upon binding through a scaffolding effect [26], which allows them to tubulate liposomes[9], stabilise tubular necks in Caveolae [10] or bind to necks of budding vesicles and drive endocytic transport [27]. The generation of anisotropic curvature has been associated with a nematic ordering of the elongated proteins along the high-curvature direction at very high coverage [28, 29]. Besides anisotropic curvature, elongated proteins can also create isotropically curved (spherical) domains, as F-BARs in the initial stages of assembly of clathrin coats [30] or during fast endocytosis by endophilin [31]. This suggests a multi-functionality of curved and elongated proteins and a correlation between curvature anisotropy, density, and nematic order. Controlled in-vitro experiments capturing this interplay have been elusive. Giant Unilamellar Vesicles (GUVs) exposed to curved and elongated proteins exhibit very little change in membrane shape below a tension-dependent protein coverage threshold, above which very thin protein-rich tubules are violently shed by the vesicle [24], and in GUVs-tether systems, the high membrane tension strongly reduces the ability of the membrane to change shape [32, 20].

Modelling lipids membrane embedded with proteins

A number of theoretical and computational studies at various scales has been developed to understand the interaction between curved proteins and membranes. At the nanoscale, all-atom molecular dynamics have described curvature generation by single domains [33] and curvature maintenance by multiple proteins [34]. Reaching a micron, coarse-grained molecular dynamics have followed the aggregation of multiple proteins to cooperatively form protein-rich curved domains [35, 36, 37, 38]. Models treating proteins as discrete objects

in a continuum membrane have examined membrane-mediated protein-protein interactions [39, 40, 41], or the spontaneous curvature induced by anchored polymers [42, 43]. A fundamental obstacle to upscale such models to multiple interacting proteins, however, is the non-additive nature of membrane-mediated pairwise interactions [44]. Reaching larger scales, continuum models combining the Helfrich curvature energy [45, 6] with thermodynamic models of mixtures [46, 47] have been quite successful in recapitulating and interpreting quantitative in-vitro measurements, see [48, 49] for two recent reviews. These models suggest that, rather than two different mechanisms, curvature sensing and generation are two manifestations of the same mechano-chemical coupling. They have provided a background to understand the emergence of heterogeneous protein-rich curved domains using linear stability analysis [50, 51], or curvature sorting of proteins in equilibrium and at fixed shape between tubes and vesicles [32, 52, 20, 53] or on wavy surfaces [54]. Also in equilibrium, protein-membrane interactions allowing for shape changes were studied in [55]. With a few exceptions under rather restrictive conditions [56, 57], previous theories of the interaction between curved proteins and membranes have focused on equilibrium. Yet, cellular functions are fundamentally out-of-equilibrium.

Coarse grained MD and Monte-Carlo simulations have been used to understand the interplay between elongated curved proteins and membrane shaping, including the relative role of scaffolding and helical insertions in curvature sensing and generation [58, 59, 29], or the self-organization of membranes and protein ensembles [60, 61, 41, 37, 62, 63]. Complementary to such micro- or mesoscale models, continuum models can provide further analytical insight and have the potential to reach longer time- and length-scales. However, previous continuum models examining the interplay between membrane shape and orientational order make strong assumptions on protein density and nematic order [64, 65], and are phenomenological in nature, introducing free energy functionals lacking a microscopic basis [66, 67]. Thus, there is a need for the development of effective field theories capturing the microscopic details of protein interactions on lipid membranes.

Structure of the thesis

We first present a summary chapter to introduce the Onsager's variational formalism, a powerful method to describe the dynamics of dissipative systems, such as the one describing lipid bilayers. This framework provides a systematic way to write the governing equations of complex systems, where the dynamics emerge from the competition between energy release rate and dissipation. This theory was more extensively introduced in [68, 69, 70].

The thesis is organised in two Parts. Part I focuses on the interaction of isotropically curved protein and membranes. In particular how such proteins interact with dynamical surfaces and their ability to sense and generate curvature.

We use the Onsager's framework to describe the protein-membrane highly coupled problem and we build a nonlinear and self-consistent continuum theory that combines the chemistry and the mechanics involved in the system. The main ingredients in the free energy include the curvature energy of the membrane with a protein-induced spontaneous curvature, the entropy of mixing of proteins, and protein-protein interactions. We present a selection of numerical calculations showing the ability of the theory to describe curvature sensing, generation, and more generally the intimate chemo-mechanical coupling of the membrane-protein system under the restriction of axisymmetry. The work is a report of the published paper:

- *"Out-of-equilibrium mechanochemistry and self-organization of fluid membranes interacting with curved proteins"*, Tozzi, Caterina, Nikhil Walani, and Marino Arroyo, New journal of physics 21.9 (2019): 093004.

Continuum modelling is a promising way to capture the dynamical reshaping of membranes embedded with proteins, but at the same time it can be disconnected from the relevant microscopic details, as in the case of BAR proteins, where their molecular organisation directly affects the membrane shape transitions. To this end, in Part II of the thesis we develop a mean-

field density functional theory, that is an extension of the work presented by Nascimiento [2], to predict the orientational order and evaluate the free-energy of ensembles of elongated and curved objects on bent membranes. This theory depends on the microscopic properties of the particles and explains how a density-dependent isotropic-to-nematic transition is modified by anisotropic curvature. The theory also allows us to examine the coexistence of isotropic and nematic phases on differently curved templates.
This work has been published here:

- *"A theory of ordering of elongated and curved proteins on membranes driven by density and curvature"*, Caterina Tozzi, Nikhil Walani, Anabel-Lise Le Roux, Pere Roca-Cusachs, Marino Arroyo, Soft Matter, 2021 (doi.org/10.1039/D0SM01733G).

In Chapter 6 and 7 we describe the isotropic-to-nematic transition of proteins on curved membranes of fixed shape. The theory can be used to understand the organization of elongated and curved proteins on membranes whose shape is restricted, as in the case of small vesicles [71], of supported lipid bilayers on wavy substrate [72], or of living cells on substrate with topographical features [73]. However, the membrane dynamics is a main ingredient to capture the two-way interplay between membrane shape and protein coverage and order. To address this point we present a self-consistent continuum chemo-mechanical model based on our mean-field theory, with the scope of predicting the role of BAR proteins isotropic-nematic organisation in membrane remodelling. We focus on the out-of-equilibrium dynamics accounting for membrane elasticity and hydrodynamics, proteins sorption, orientational order and diffusion. We study theoretically and experimentally the dynamical binding of BAR proteins on mechanically bent lipid membranes. The results allow us to characterize a variety of dynamical reshaping events depending on membrane shape and proteins arrangement. The experimental work presented in this thesis was performed by our collaborators at the Institute for Bioengineering of Catalonia (IBEC).
A more extensive description is in our publication:

- *"Dynamic Mechanochemical feedback between curved membranes and BAR protein self-organization"*, Anabel-Lise Le Roux, Caterina Tozzi, Nikhil Walani, Xarxa Quiroga, Dobryna Zalvidea, Xavier Trepat, Margarita Staykova, Marino Arroyo, Pere Roca-Cusachs, bioRxiv (2020).

.

In summary, the work done in this thesis aims at a complete and deep understanding of the mechanisms involved in protein-membrane interaction. We have developed two general theoretical frameworks that capture the different chemo-mechanical responses of lipid membranes interacting in one case with isotropically bent proteins and in the other with uniaxially elongated proteins. Furthermore, we have also developed a mean-field theoretical study that relates the microscopic properties of the proteins with the free energy of the membrane-protein system. In this way we have been able to explore the density-dependent isotropic-to-nematic phase transition that characterizes BAR proteins in a dense packing limit or on anisotropic curvatures.

Part I

Isotropically curved proteins

Chapter 2

A model for the mechanics of lipid membranes and intrinsically-curved proteins

In this chapter we present a general continuum model that describes the protein-membrane chemo-mechanical interaction, built following Onsager's variational formalism [68, 69, 70], a variational method used for irreversible thermodynamical problems. A major point of this principle is that it can be applied to fully non-linear settings suitable to describe complex soft-matter problems, including elasticity, low Reynolds number hydrodynamics and reaction-diffusion system. The fundamental idea of the Onsager's formalism is to derive the time evolution of the system through a minimization problem that includes energy released, energy dissipated and energy exchanged by the system. In our model the main ingredients in the free energy include the curvature energy of the membrane with a protein-induced spontaneous curvature, the entropy of mixing of proteins, and protein-protein interactions. As it evolves, the system dissipates energy through the drag between proteins and the membrane, and through lipid shear viscosity as the membrane changes shape. We particularize

this general theory to an axisymmetric configuration.

2.1 Setup, Kinematics and Balance Laws

We model the lipid bilayer as a material surface Γ parametrized by $\boldsymbol{r}(\theta^\alpha, t)$, where (θ^1, θ^2) are Lagrangian coordinates labelling material particles and t denotes time. The model proposed here does not explicitly describe each of the two monolayers [74, 75]. Accounting for the bilayer architecture may be pertinent to some molecular curving mechanisms, such as shallow insertions into one of the monolayers, whereas the model developed here could apply to interactions that equally affect both monolayers such as scaffolding or full insertion of transmembrane proteins [76]. Using standard differential geometry [77], we use this parametrization to define the tangent vectors at each material point as $\boldsymbol{g}_\alpha = \partial \boldsymbol{r}/\partial\theta^\alpha$, which form the natural basis of the tangent space, and the metric tensor with covariant components $g_{\alpha\beta} = \boldsymbol{g}_\alpha \cdot \boldsymbol{g}_\beta$. The components $g^{\beta\gamma}$ of the inverse of the metric tensor follow from the relations $g_{\alpha\beta}g^{\beta\gamma} = \delta^\gamma_\alpha$. The unit normal to the surface is $\boldsymbol{n} = (\boldsymbol{g}_1 \times \boldsymbol{g}_2)/\sqrt{g}$, where $g = \det g_{\alpha\beta}$. The local curvature of the surface $\boldsymbol{k}$ is characterized by the second fundamental form, which measures changes in the normal and whose components in the natural basis are $k_{\alpha\beta} = \boldsymbol{n}\cdot\partial\boldsymbol{g}_\alpha/\partial\theta^\beta$. The invariants of the second fundamental form are its trace $H = \operatorname{tr}\boldsymbol{k} = k_{\alpha\beta}g^{\alpha\beta}$ (twice the mean curvature) and its determinant $K = \det\{\boldsymbol{k}\} = \det k_{\alpha\beta}g^{\beta\gamma}$ (Gaussian curvature). Throughout the text, ∇ denotes the covariant derivative or surface gradient and $\nabla\cdot$ the surface divergence.

The dynamics of the surface are determined by its Lagrangian velocity, which can be decomposed into tangential and normal components as

$$\boldsymbol{V} = \frac{\partial \boldsymbol{r}}{\partial t} = \boldsymbol{v} + v_n\boldsymbol{n}. \tag{2.1}$$

As a result of this flow, the metric tensor changes with time. Its material time derivative, a partial derivative in our Lagrangian setting, is called the rate-of-deformation tensor of the surface [78, 75],

$$\boldsymbol{d} = \frac{1}{2}\frac{\partial \boldsymbol{g}}{\partial t} = \frac{1}{2}(\nabla\boldsymbol{v} + \nabla\boldsymbol{v}^T) - v_n\boldsymbol{k}, \tag{2.2}$$

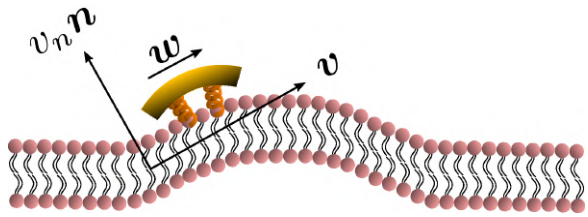

Figure 2.1: The state of the system, given by the shape of the bilayer mid-surface and by the protein area fraction, can evolve as a result of the membrane velocity ($\boldsymbol{V}$), tangential ($\boldsymbol{v}$) and normal (v_n), and of the diffusive velocity of proteins relative to the membrane ($\boldsymbol{w}$).

and includes the usual term accounting for deformation resulting from tangential flows, and a term accounting for deformation resulting from shape changes, which involves the normal velocity and the curvature. The rate of change of local area follows as

$$\operatorname{tr} \boldsymbol{d} = \nabla \cdot \boldsymbol{v} - v_n H. \tag{2.3}$$

We adopt a mean field description of proteins in terms of a scalar field $\phi(\theta^\alpha, t)$ measuring their local area fraction. In doing so, we assume that proteins are isotropic, or in a regime in which entropic effects dominate over orientational order. In the second Part of the thesis we will account for the nematic order of proteins, pertinent for instance to elongated membrane proteins with BAR domains [9, 37, 41].

Balance of mass

Denoting by $\rho_l(\theta^\alpha, t)$ the lipid areal density, balance of mass of lipids requires $\partial\rho_l/\partial t + \rho_l \operatorname{tr} \boldsymbol{d} = 0$. Note that in this equation $\partial\rho_l/\partial t$ coincides with the material time-derivative since we consider a Lagrangian parametrization. This equation ignores the area fraction occupied by protein insertions, which except for channels is much smaller than the area fraction occupied by the membrane protein at the periphery of the bilayer, see Fig. 2.1. At moderate tensions we can assume that lipids are inextensible, and hence their density constant.

Consequently, lipid membrane inextensibility requires that

$$\operatorname{tr} \boldsymbol{d} = 0. \tag{2.4}$$

Since proteins are a diffusive species, balance of mass of proteins can be expressed as

$$\frac{\partial \phi}{\partial t} + \phi \ \operatorname{tr} \boldsymbol{d} + \nabla \cdot (\phi \boldsymbol{w}) = 0 \quad \text{on} \quad \Gamma, \tag{2.5}$$

where $\boldsymbol{w}$ is the diffusive velocity relative to the Lagrangian coordinates and we have ignored protein sorption. Again, because of our Lagrangian parametrization, $\partial\phi/\partial t$ coincides with the material time-derivative $\dot{\phi}$.

2.2 Energetics, dissipation and power input

To describe the dynamics of protein-membrane interactions, as introduced before, we adopt the nonlinear Onsager's formalism of dissipative dynamics [79, 70, 69], according to which the time evolution of the system follows a minimization principle where energy release and dissipation compete. In the present context, the state variables $\boldsymbol{r}$ and ϕ determine the elastic energy (associated to bending) and the chemical energy (entropy and self-interactions) of the system, whereas the variables characterizing changes in the state of the system, here $\boldsymbol{V}$ and $\boldsymbol{w}$, determine energy dissipation through shear viscous forces in the membrane and friction as proteins move relative to the membrane. Onsager's formalism provides a transparent method to derive the governing equations even in the presence of strong nonlinearity, here caused mechanically by the very large deformations of the membrane and chemically by molecular crowding in protein-rich domains.

Energetics

To describe the bending energy of the membrane, we follow a classical Helfrich model [45, 6, 80], ignoring the Gaussian curvature terms for simplicity but including a spontaneous curvature that depends on protein density. Assuming

a linear dependence of preferred curvature on protein density, a common form of the bending energy is

$$\mathcal{F}_b = \int_\Gamma \frac{\kappa}{2}(H - \bar{C}\phi)^2 \, dS, \tag{2.6}$$

where κ is the bending modulus and $\bar{C}$ encodes the curving strength of proteins. Other variants of this model have been proposed [48] and further discussed in Section 4.5.

For the free energy of the proteins on the surface, we adopt a Flory-Huggins [46, 47] model accounting for the entropy of mixing and for protein-protein interactions

$$\mathcal{F}_p = \int_\Gamma \left\{ \frac{k_B T}{a_p}[\phi \log \phi + (\phi_m - \phi) \log (\phi_m - \phi)] + \frac{\chi}{2a_p}\phi^2 + \frac{\mu_0}{a_p}\phi \right\} dS. \tag{2.7}$$

In this equation, $k_B T$ is the thermal energy, a_p is the area on the membrane of a single protein so that ϕ/a_p is the number density, the term involving ϕ_m (a saturation area fraction) accounts for the entropy of uncovered spaces, χ determines the strength and sign (attractive or repulsive) of protein-protein interactions, and μ_0 is a reference chemical potential. Variants of this model have been used to understand the linear stability of fully mixed states [50, 51] or to examine protein sorting by curvature at fixed shape [32, 54, 20].

Depending on the parameters and the boundary conditions, the model can lead to phase separation. For instance, negative χ promotes demixing and coexistence of a protein-rich and depleted phases. To regularize phase boundaries, we consider a term penalizing the gradient, which can be interpreted as a non-local interaction of proteins

$$\mathcal{F}_{\text{nl}} = \int_\Gamma \frac{\Lambda}{2a_p}|\nabla\phi|^2 \, dS, \tag{2.8}$$

Λ being a material parameter. The length scale of this interaction is of the order $\sim \sqrt{\Lambda/|\chi|}$, which, for a planar membrane, determines the thickness of the interface between protein-rich and depleted domains. Without this term, there is no energetic penalty to domain boundaries and the equations may

become ill-posed [81]. Total free energy of this system is then given by

$$\mathcal{F} = \mathcal{F}_b + \mathcal{F}_p + \mathcal{F}_{\text{nl}} = \int_\Gamma W(H, \phi, |\nabla\phi|^2)\, dS, \tag{2.9}$$

where W represents the total energy density of the membrane-protein composite system. We note that this form of energy density is not the most general that can be conceived for diffusing proteins on an inextensible fluid membrane without orientational order. For instance, the energy could also depend on the scalar invariant $\nabla\phi \cdot \boldsymbol{k}\nabla\phi$ [82].

A central thermodynamic quantity that drives protein diffusion and sorption is the chemical potential μ [69], measuring the amount of work required to add a molecule at a particular membrane location. The chemical potential can be identified from the variational derivative of $\mathcal{F}$ with respect to ϕ as

$$\delta_\phi \mathcal{F} = \int_\Gamma \mu \frac{\delta\phi}{a_p}\, dS = \int_\Gamma \Big[D_2 W\ \delta\phi + D_3 W\ \delta(|\nabla\phi|^2) \Big]\, dS, \tag{2.10}$$

where $D_i W$ denotes the partial derivative of W with respect to its i-th argument. Because this variation is taken at fixed shape, $\delta(|\nabla\phi|^2) = 2\nabla\phi \cdot \nabla\delta\phi$. Using the notation $W_H = D_1 W$, $W_\phi = D_2 W$, and $W_{\nabla\phi} = 2D_3 W\ \nabla\phi$, and integrating by parts, we obtain

$$\delta_\phi \mathcal{F} = \int_\Gamma (W_\phi - \nabla \cdot W_{\nabla\phi})\delta\phi\, dS + \int_{\partial\Gamma} (\delta\phi) W_{\nabla\phi} \cdot \boldsymbol{\nu}\, dl \tag{2.11}$$

with $\boldsymbol{\nu}$ representing the in-plane normal at the edge $\partial\Gamma$. Ignoring the boundary term, comparison of the two equations above allows us to identify the chemical potential from Eq. 2.9 as,

$$\mu = a_p(W_\phi - \nabla \cdot W_{\nabla\phi}) = \mu_0 - a_p\kappa\bar{C}(H - \bar{C}\phi) + k_B T \log\frac{\phi}{\phi_m - \phi} + \chi\phi - \Lambda\Delta\phi, \tag{2.12}$$

where Δ denotes the surface Laplacian. This expression clearly shows the contributions to the chemical potential given by bending elasticity, entropy and protein self-interactions.

Dissipation

Having described the mechanisms through which membrane and proteins store energy, we now detail the dynamical modes through which the system dissipates energy. Lipid bilayers in a fluid phase behave like interfacial viscous Newtonian fluids [7, 83]. Here, we ignore dissipative forces resulting from inter-monolayer slippage [74, 75, 84]. Having assumed that the membrane is locally inextensible, $\mathrm{tr}\,\boldsymbol{d} = 0$, the dissipation potential accounting for in-plane shear can be written as

$$\mathcal{D}_m = \int_\Gamma \eta\, \boldsymbol{d} : \boldsymbol{d}\, dS, \tag{2.13}$$

where η is the in-plane shear viscosity of the membrane and the rate-of-deformation tensor $\boldsymbol{d}$ is given by Eq. 2.2 [83].

Protein transport is characterized by the collective protein velocity $\boldsymbol{w}$ relative to the lipids in the membrane, which has already appeared in the statement of balance of proteins, see Eq. 2.5. As a single protein moves relative to the lipids, it experiences a drag force given by $-\xi\boldsymbol{w}$, where ξ is the molecular drag coefficient. By superposition in a dilute approximation, a collection of proteins characterized by local number density ϕ/a_p experiences a drag force per unit area given by $-\xi\phi\boldsymbol{w}/a_p$. The associated dissipation potential can then be written as

$$\mathcal{D}_p = \int_\Gamma \frac{\xi}{2a_p}\phi|\boldsymbol{w}|^2\, dS. \tag{2.14}$$

For simplicity, we ignore the dissipation occurring in the bulk fluid. This approximation could break down if fast shape changes occurred over length-scales larger than the Saffman-Dellbrück length, of about 1 to 10 microns [83, 85]. In most situations, however, fast curvature generation by proteins leads to much smaller geometric features [24, 86, 87]. Thus, the total dissipation potential of the system is given by:

$$\mathcal{D}[\boldsymbol{v}, v_n, \boldsymbol{w}] = \mathcal{D}_m + \mathcal{D}_p. \tag{2.15}$$

Power input

Let us consider a membrane patch Γ, possibly with smooth boundary $\partial\Gamma$. In absence of body forces or sorption of proteins from the bulk, power can only be supplied to the system through edge tractions, moments or flux of proteins at a given chemical potential. Assuming that Γ is a material surface, and thus no lipids can flow through $\partial\Gamma$, we write the power input functional as

$$\mathcal{P}_{\text{ext}} = \int_{\partial\Gamma} \frac{\mu_b}{a_p}(\phi \boldsymbol{w})\cdot\boldsymbol{\nu}\, dl - \int_{\partial\Gamma} (F_\tau \boldsymbol{v}\cdot\boldsymbol{\tau} + F_\nu \boldsymbol{v}\cdot\boldsymbol{\nu} + F_n v_n)\, dl + \int_{\partial\Gamma} M\boldsymbol{\nu}\cdot\dot{\boldsymbol{n}}\, dl, \quad (2.16)$$

where μ_b is a fixed chemical potential for proteins at the boundary, e.g. maintained by a protein reservoir, $\boldsymbol{\tau}$ is a unit tangent vector along $\partial\Gamma$ so that $\boldsymbol{\nu} = \boldsymbol{\tau} \times \boldsymbol{n}$, F_τ, F_ν and F_n are traction components at the boundary, M is a bending moment per unit length, and $\dot{\boldsymbol{n}}$ represents the material time derivative of the surface normal. We can express the last integral in terms of our dynamical variables $\boldsymbol{v}$ and v_n using the relation

$$\boldsymbol{\nu}\cdot\dot{\boldsymbol{n}} = -\nabla v_n \cdot \boldsymbol{\nu} - \tau(\boldsymbol{v}\cdot\boldsymbol{\tau}) - \kappa_\nu(\boldsymbol{v}\cdot\boldsymbol{\nu}), \quad (2.17)$$

where $\tau = \boldsymbol{k}\boldsymbol{\nu}\cdot\boldsymbol{\tau}$ is the geodesic torsion of the boundary curve and $\kappa_\nu = \boldsymbol{k}\boldsymbol{\nu}\cdot\boldsymbol{\nu}$ its normal curvature [88, 89]. Each of these terms can be defined on Neumann parts of the boundary $\partial\Gamma$.

2.3 Governing equations

Onsager's variational principle

The Onsager's recipe, used to derive the dissipative dynamics of the problem, accounts for the minimization of the Rayleghian functional as

$$\mathcal{R} = \dot{\mathcal{F}} + \mathcal{D} + \mathcal{P}_{\text{ext}}, \quad (2.18)$$

where $\dot{\mathcal{F}}$ is the rate of change of the energy [69, 70]. To enforce local inextensibility, see Eq. 2.4, and possibly the incompressibility of the fluid enclosed by the membrane, we introduce a Lagrange multiplier field σ (contributing to

membrane tension) and a Lagrange multiplier p (pressure difference) to form the Lagrangian

$$\mathcal{L} = \dot{\mathcal{F}} + \mathcal{D} + \mathcal{P}_{\text{ext}} + \int_\Gamma \sigma \operatorname{tr} \boldsymbol{d}\, dS - p \int_\Gamma v_n\, dS. \tag{2.19}$$

Since Γ is a material surface, the rate of change of energy can be written as

$$\dot{\mathcal{F}} = \int_\Gamma (\dot{W} + W \operatorname{tr} \boldsymbol{d})\, dS \tag{2.20}$$

where $\dot{W}$ is the material time-derivative of the energy density and is given by

$$\dot{W} = W_H \dot{H} + W_\phi \dot{\phi} + D_3 W \, \frac{d}{dt} \left(|\nabla \phi|^2 \right). \tag{2.21}$$

Note carefully that, because $|\nabla\phi|^2 = g^{\alpha\beta}\phi_{,\alpha}\phi_{,\beta}$ with $\phi_{,\alpha} = \partial\phi/\partial\theta^\alpha$ involves the inverse of the metric tensor, which depends on the membrane configuration, the time derivative in the last term involves not only $\dot{\phi}$ but also the velocity of the surface. Indeed,

$$\frac{d}{dt}\left(g^{\alpha\beta}\phi_{,\alpha}\phi_{,\beta} \right) = -2\nabla\phi \cdot \boldsymbol{d} \cdot \nabla\phi + 2\nabla\phi \cdot \nabla\dot{\phi}. \tag{2.22}$$

Using the above equation, the relation $\dot{H} = \boldsymbol{v} \cdot \nabla H + \Delta v_n + v_n(H^2 - 2K)$ [83], balance of mass of proteins in Eq. 2.5 and the divergence theorem, we can express the rate of change of the energy by explicitly highlighting its dependence on the variables $\boldsymbol{w}$ and $\boldsymbol{V} = \boldsymbol{v} + v_n \boldsymbol{n}$

$$\begin{aligned}
\dot{\mathcal{F}} = & \int_\Gamma \frac{\nabla\mu}{a_p} \cdot (\phi \boldsymbol{w})\, dS \\
& + \int_\Gamma \left[W_H \nabla H + \nabla\left(\frac{\mu\phi}{a_p} \right) - \nabla W + 2 D_3 W \nabla \cdot (\nabla\phi \otimes \nabla\phi) \right] \cdot \boldsymbol{v}\, dS \\
& + \int_\Gamma \left[\Delta W_H + W_H(H^2 - 2K) + \frac{\mu}{a_p}\phi H - W H + 2 D_3 W \boldsymbol{k} : (\nabla\phi \otimes \nabla\phi) \right] v_n\, dS \\
& - \int_{\partial\Gamma} \frac{\mu}{a_p} (\phi \boldsymbol{w}) \cdot \boldsymbol{\nu}\, dl - \int_{\partial\Gamma} 2 D_3 W (\nabla\phi \cdot \boldsymbol{\nu}) \nabla \cdot (\phi \boldsymbol{w})\, dl + \int_{\partial\Gamma} \left(W - \frac{\mu\phi}{a_p} \right) \boldsymbol{v} \cdot \boldsymbol{\nu}\, dl \\
& - \int_{\partial\Gamma} (\nabla W_H \cdot \boldsymbol{\nu}) v_n\, dl + \int_{\partial\Gamma} W_H (\nabla v_n \cdot \boldsymbol{\nu})\, dl - \int_{\partial\Gamma} 2 D_3 W (\nabla\phi \cdot \boldsymbol{v})(\nabla\phi \cdot \boldsymbol{\nu})\, dl.
\end{aligned} \tag{2.23}$$

In the literature dealing with the Cahn-Hilliard equation, related to our model, the second term in the fourth line is set to zero by requiring the natural high-order boundary condition $\nabla\phi \cdot \boldsymbol{\nu} = 0$ on $\partial\Gamma$ [90]. As a result, the last integral over the edge also vanishes. Similarly, we can express the constraint of local area conservation as

$$\int_\Gamma \sigma \operatorname{tr} \boldsymbol{d}\, dS = -\int_\Gamma \nabla\sigma \cdot \boldsymbol{v}\, dS - \int_\Gamma \sigma v_n H\, dS + \int_{\partial\Gamma} \sigma \boldsymbol{v} \cdot \boldsymbol{\nu}\, dl. \tag{2.24}$$

To obtain the governing equations of the system, we substitute the above relations in Eq. (2.19), minimize the Lagrangian with respect to $\{\boldsymbol{w}, \boldsymbol{v}, v_n\}$ and maximize it with respect to $\{\sigma, p\}$. Surface integrals in the two expressions above contribute to the Euler-Lagrange governing equations whereas boundary terms identify the Neumann boundary conditions. The resulting equations for the specific choice of W given in Section 2.2 are discussed below.

Transport of proteins

Minimizing the Lagrangian with respect to the diffusive velocity, $\delta_{\boldsymbol{w}}\mathcal{L} = 0$, we obtain the diffusive flux of membrane proteins consistent with Fick's law

$$\phi\boldsymbol{w} = -\frac{\phi\nabla\mu}{\xi} \text{ in } \Gamma. \tag{2.25}$$

Substituting the above relation in Eq. 2.5 and using the inextensibility of the lipid membrane we obtain

$$\frac{\xi}{a_p}\dot{\phi} - \nabla\cdot(\phi\nabla\mu) = 0, \tag{2.26}$$

which can be expanded recalling Eq. 2.12 and rearranged to yield the transport equation for proteins

$$\xi\dot{\phi} + \nabla\cdot\left[a_p\kappa\bar{C}\nabla H\phi - \left(\chi^{\text{eff}}\phi + \frac{k_BT\phi_m}{\phi_m-\phi}\right)\nabla\phi + \Lambda\phi\nabla(\Delta\phi)\right] = 0, \tag{2.27}$$

where we have defined the effective interaction between proteins as $\chi^{\text{eff}} = \chi + a_p\kappa\bar{C}^2$. For vanishing spontaneous curvature ($\bar{C}$=0), this governing equation ceases to depend explicitly on the curvature of the underlying surface,

although it does depend on its geometry through the covariant derivative, and it reduces to a nonlinear Cahn-Hilliard equation [91] on the surface with a density-dependent diffusion coefficient

$$D(\phi) = \frac{1}{\xi}\left(\chi^{\text{eff}}\phi + \frac{k_B T \phi_m}{\phi_m - \phi}\right). \tag{2.28}$$

For $\chi = 0$, $\Lambda = 0$ and $\phi \ll \phi_m$, Eq. 2.27 reduces to the linear diffusion equation. For $\bar{C} \neq 0$, the curvature gradient introduces a bias in the diffusion with drift velocity

$$\boldsymbol{w}^{\text{drift}} = a_p \kappa \bar{C} \nabla H / \xi, \tag{2.29}$$

driving curved proteins along or against the curvature gradient depending on the sign of $\bar{C}$. At steady state, drift and diffusive transport must balance and yield a divergence-free flux.

In-plane force balance

Minimization of the Lagrangian respect to the in-plane velocity, $\delta_{\boldsymbol{v}}\mathcal{L} = 0$, yields

$$\nabla\sigma - \frac{\phi\nabla\mu}{a_p} + 2\eta\nabla\cdot\boldsymbol{d} = \boldsymbol{0}, \tag{2.30}$$

where the first term accounts for the tension required to impose lipid membrane inextensibility, the second term is a force density on the fluid membrane resulting from the relative motion of proteins, see Eq. 2.25, and the third term represents tangential dissipative forces due to membrane viscosity, which strongly depend on curvature and involve both tangential and normal velocities as discussed in detail elsewhere [83, 92].

In the common situation of an incompressible Stokes flow with a dilute diffusing species, the drag force density due to protein motion, the second term in Eq. 2.30, does not contribute to the hydrodynamics because $\phi\nabla\mu$ can be expressed as a gradient and grouped with the Lagrange multiplier enforcing incompressibility in all the governing equations [69]. Here, however, this is not the case. Indeed, introducing Eq. 2.12 into 2.30 we obtain

$$\nabla\sigma^{\text{eff}} - \frac{\Lambda}{a_p}\nabla\cdot(\nabla\phi\otimes\nabla\phi)^{\text{dev}} + \frac{\xi}{a_p}\phi\boldsymbol{w}^{\text{drift}} + 2\eta\nabla\cdot\boldsymbol{d} = \boldsymbol{0} \tag{2.31}$$

where $(\boldsymbol{a}\otimes\boldsymbol{a})^{\text{dev}} = \boldsymbol{a}\otimes\boldsymbol{a} - (|\boldsymbol{a}|^2/2)\boldsymbol{g}$ is the deviatoric component of this rank-one tensor, and we identify the effective membrane tension (the hydrostatic part of the stress tensor) as

$$\sigma^{\text{eff}} = \sigma + \frac{k_B T}{a_p}\phi_m \log(\phi_m - \phi) - \frac{\chi^{\text{eff}}}{2a_p}\phi^2 + \frac{\Lambda}{a_p}\phi\Delta\phi. \tag{2.32}$$

Since the third term in Equation 2.31 cannot be expressed as a gradient, the drift contribution to protein transport generates a tangential force density introducing an explicit coupling between hydrodynamics and protein transport. This protein-induced force just requires the presence of curved proteins and a curvature gradient and can drive flows out-of-equilibrium. Furthermore, as a result of the fundamental in-plane/out-of-plane coupling mediated by curvature [92], this force density can induce out-of-plane forces and shape changes. At steady state, since $\boldsymbol{w}^{\text{drift}}$ is in general different from zero, Eq. 2.31 shows that we can expect a non-uniform effective membrane tension in the presence of gradients of curvature. The second term in Eq. 2.31 further contributes to a non-uniform and also non-hydrostatic membrane tension in equilibrium, in this case associated to gradients in ϕ.

Going back to the notion of effective tension σ^{eff}, one way to think about it is just as a Lagrange multiplier enforcing local inextensibility. However, Eq. 2.32 provides further insight about this tension. The first term, σ can be interpreted as the membrane tension of the lipids. The second term is the osmotic tension due to the presence of proteins. In the limit $\phi \ll \phi_m$, this term becomes $-k_B T\phi/a_p$, recovering the Van't Hoff's equation. The third term accounts for the fact that attractive/repulsive proteins increase/decrease surface tension. The last term is a non-local tension that can become significant at phase boundaries. Thus, σ^{eff} is a measure of tension in the composite membrane-protein system. We refer to Appendix A.1 for a complementary and detailed derivation of the stress in the present theory.

Force balance normal to the surface

Minimization with respect to the normal component of the velocity, $\delta_{v_n}\mathcal{L} = 0$, yields

$$\begin{aligned}\kappa\left[\Delta(H-\bar{C}\phi)+(H-\bar{C}\phi)\left(\frac{H^2}{2}-2K\right)-\frac{H^2\bar{C}\phi}{2}\right]\\ -\sigma^{\text{eff}}H-p+\frac{\Lambda}{a_p}\boldsymbol{k}:(\nabla\phi\otimes\nabla\phi)^{\text{dev}}-2\eta\boldsymbol{d}:\boldsymbol{k}=0,\end{aligned}\tag{2.33}$$

where the first term corresponds to an out-of-plane force density due to membrane curvature elasticity, and hence coupled to the protein density, the second to fourth terms account for Laplace's law, and the last term is a normal viscous force density due to membrane shear, studied in detail in [83, 92].

Boundary Conditions

In the chemo-mechanical problem studied here, we can impose Dirichlet boundary conditions in part of the boundary $\partial\Gamma$ for the different fields. For instance, reasonable Dirichlet conditions for the mechanical part of the problem include fixing $\boldsymbol{v}\cdot\boldsymbol{\tau}=\hat{v}_\tau$, $\boldsymbol{v}\cdot\boldsymbol{\nu}=\hat{v}_\nu$, $v_n=\hat{v}_n$ and $\nabla v_n\cdot\boldsymbol{\nu}=\hat{\omega}$ on a part of $\partial\Gamma$, where $\hat{v}_\tau$, $\hat{v}_\nu$, $\hat{v}_n$ and $\hat{\omega}$ are Dirichlet data. For the chemical problem, the Dirichlet boundary condition is prescribing $\phi\boldsymbol{w}\cdot\boldsymbol{\nu}=\hat{j}_b$ on part of $\partial\Gamma$.

On parts of the boundary where Dirichlet boundary conditions are not specified, we obtain the following Neumann boundary conditions by extremizing the Lagrangian and collecting terms at the boundary:

$$\begin{aligned}\mu_b=\mu,\qquad M=W_H,\qquad F_\nu=W-\frac{\mu\phi}{a_p}+\sigma-\kappa_\nu M+2\eta\,\boldsymbol{\nu}\cdot\boldsymbol{d}\cdot\boldsymbol{\nu},\\ F_n=-\nabla W_H\cdot\boldsymbol{\nu},\qquad F_\tau=-\tau M+2\eta\,\boldsymbol{\tau}\cdot\boldsymbol{d}\cdot\boldsymbol{\nu}.\end{aligned}\tag{2.34}$$

The first condition sets the chemical potential in the Neumann part of the boundary, whereas the next four equations set the applied torque and force per unit length. The in-plane force can be further recast in a form clearly showing the contributions of the effective surface tension and bending energy

as

$$F_\nu = \frac{\kappa}{2}H^2 + \sigma^{\text{eff}} - \kappa_\nu M + 2\eta\, \boldsymbol{\nu}\cdot\boldsymbol{d}\cdot\boldsymbol{\nu}. \tag{2.35}$$

For surfaces at equilibrium with flat boundaries, the forces normal to the boundary per unit length transmitted by the membrane is tangential and given by σ^{eff}.

Time-scales of shape and protein density relaxation

The chemo-mechanical model described by the transport equation for proteins (2.27), membrane inextensibility (2.4), force balance in-plane (2.31) and out-of-plane (2.33) exhibits multiple intrinsic relaxation time-scales. To examine the competition of mechanical and chemical relaxation time-scales, we consider the simplest cases of shape disturbances whose relaxation is driven by bending elasticity and dragged by membrane viscosity, and of protein density disturbances entropically penalized and dragged by the friction between proteins and the lipid membrane. Such mechanical relaxation occurs during the characteristic time $\tau_m = \eta\bar{S}/\kappa$, where $\bar{S}$ is the surface area of the disturbance. The characteristic time for protein diffusion is $\tau_p = \xi\bar{S}/(k_BT)$. Their ratio is thus

$$\frac{\tau_m}{\tau_p} = \frac{k_BT\eta}{\kappa\xi} \approx \frac{\eta}{20\xi}, \tag{2.36}$$

where we have used the common estimate for the bending stiffness $\kappa \approx 20k_BT$. In turn, ξ is related to the membrane surface viscosity η through the Saffman-Delbrück theory [93], which states that

$$\xi = \frac{4\pi\eta}{\log(2L_{\text{sd}}/\ell_a) - \gamma}, \tag{2.37}$$

where $L_{\text{sd}} \approx 5$ μm is the ratio of membrane and bulk viscosity, $\ell_a \approx 1$ nm is the effective radius of the protein and $\gamma \approx 0.577$ is the Euler Mascheroni constant. Using this estimation we obtain, $\xi \approx 2\pi\eta$, which results in $\tau_m/\tau_p \approx 1/(40\pi)$. Thus, mechanical relaxation occurs nearly two orders of magnitude faster than protein relaxation by diffusion. Although other phenomena accounted for in our general theory (such as protein self-interaction, drift by curvature

gradients, or mechanical forces due to the presence of curved proteins on the membrane) can influence the dynamics of the system, this simple estimate establishes that in general protein transport can be expected to be the slow process.

2.4 Axisymmetric formulation

Under the assumption of axisymmetry, pertinent to many structures resulting from protein-membrane interactions, the shape of the membrane can be parametrized in terms of the distance to the z axis and the z coordinate of its generating curve $(\rho(u,t), z(u,t))$, where u is a Lagrangian coordinate labeling material particles in the interval $[0,1]$ and t is time. Protein area fraction does not depend on the azimuthal angle and thus can be expressed as $\phi(u,t)$. For closed surfaces, smoothness of the surface at the poles is guaranteed by the conditions $\rho(0,t) = 0$, $z'(0,t) = 0$ and $\rho(1,t) = 0$, $z'(1,t) = 0$, where $(\cdot)'$ denotes the partial derivative with respect to u. For an open patch, we replace the condition at $u = 1$ by $z(1,t) = 0$, $z'(1,t) = 0$. The diffusive protein velocity can be expressed as $\boldsymbol{w}(u,t) = w(u,t)\boldsymbol{t}(u,t)$, where $\boldsymbol{t} = (\rho', z')/a$ is the unit tangent vector to the generating curve and $a(u) = \sqrt{\rho'(u)^2 + z'(u)^2}$ is the speed of this curve.

From the generating curve, we can compute the mean curvature of the surface as

$$H = \frac{1}{a}\left(\frac{b}{a^2} + \frac{z'}{\rho}\right), \tag{2.38}$$

where $b(u) = -\rho''(u)z'(u) + \rho'(u)z''(u)$ [85]. Noting that the element of area is $dS = 2\pi a\rho\, du$, this expression allows us to compute the bending energy $\mathcal{F}_b[\rho, z; \phi]$ in Eq. (2.6).

As a reference surface $\bar{\Gamma}$ with local radius $\bar{\rho}$ and speed $\bar{a}$ is mapped to the current surface Γ with radius ρ and speed a, the local areal stretch at each point is $J = (a\rho)/(\bar{a}\bar{\rho})$. Thus, membrane inextensibility can be expressed as $J = 1$, or $a\rho = \bar{a}\bar{\rho}$. As shown in [85], the membrane dissipation potential in Eq. 2.13 for an axisymmetric inextensible membrane described with

Lagrangian coordinates can be expressed as

$$\mathcal{D}_m[\dot{\rho};\rho,z] = \int_0^1 2\eta \left(\frac{\dot{\rho}}{\rho}\right)^2 2\pi a\rho\, du. \tag{2.39}$$

Balance of mass of proteins in Eq. 2.5 for an inextensible membrane can be expressed in the present setting as $0 = \dot{\phi} + (\rho\phi w)'/(a\rho)$. Plugging the expression for $\boldsymbol{w}$ issued from Onsager's principle, we rewrite Eq. 2.27 under axisymmetry as

$$\xi\dot{\phi} + \frac{1}{a\rho}\left\{\frac{\rho}{a}a_p\kappa\bar{C}\phi H' - \frac{\rho}{a}\left[\chi^{\text{eff}}\phi + \frac{k_BT\phi_m}{(\phi_m-\phi)}\right]\phi' + \frac{\rho}{a}\Lambda\phi L'(\phi)\right\}' = 0, \tag{2.40}$$

where

$$L(\phi) = \frac{1}{a\rho}\left[\left(\frac{\rho}{a}\right)'\phi' + \frac{\rho}{a}\phi''\right] \tag{2.41}$$

is the surface Laplacian of ϕ.

Chapter 3

Numerical approximation

Here, we discretize the governing equations for the protein-membrane dynamical model with a Galerking method. In particular we use B-Spline approximations to numerically rapresents the physical fields in the space-discretized form and backward Euler approximation for time-discretization.

To perform numerical calculations, we use a Galerkin finite element approach based on a B-Spline approximation of the different fields. We numerically represent the state variables as

$$\{\phi(u,t), \rho(u,t), z(u,t)\} = \sum_{J=1}^{N} B_J(u)\{\phi_J(t), \rho_J(t), z_J(t)\}, \tag{3.1}$$

where B_J are cubic B-spline basis functions, and $\{\phi_J(t), \rho_J(t), z_J(t)\}$ are the $J-$th control points of the state variables at time t [94]. This approximation provides C^2 continuity, enough for our formulation, which requires at least C^1 continuity for square integrable curvatures and protein Laplacians.

To move forward in time, we adopt a staggered approach in which we first evolve the protein density field at fixed membrane shape, and then update shape at fixed protein distribution. To obtain the concentration of proteins ϕ^{n+1} at time t^{n+1}, we assume a given shape of membrane $\{\rho^n, z^n\}$ at time

$t^n = t^{n+1} - \Delta t^n$, use a backward Euler approximation to discretize Eq. 2.40 in time, multiply this equation with a test function $\psi(u)$, integrate over the surface and integrate by parts. For simplicity of our exposition, we assume no flux of proteins through the boundary to obtain

$$\begin{aligned}
&\xi \int_0^1 (a^n \rho^n) \left(\frac{\phi^{n+1} - \phi^n}{\Delta t^n} \right) \psi \, du + \int_0^1 \frac{\rho^n}{a^n} \left(\chi^{\text{eff}} \phi^{n+1} + \frac{k_B T \phi_m}{\phi_m - \phi^{n+1}} \right) \phi^{n+1'} \psi' \, du \\
&+ \int_0^1 a_p \kappa \bar{C} H^n \left[\left(\frac{\rho^n}{a^n} \right)' \phi^{n+1} \psi' + \frac{\rho^n}{a^n} \phi^{n+1'} \psi' + \frac{\rho^n}{a^n} \phi^{n+1} \psi'' \right] du \\
&+ \int_0^1 \frac{\Lambda}{a^n \rho^n} \left[\left(\frac{\rho^n}{a^n} \right)' \phi^{n+1'} + \frac{\rho^n}{a^n} \phi^{n+1''} \right] \left[\left(\frac{\rho^n}{a^n} \right)' \phi^{n+1} \psi' \right. \\
&\left. + \frac{\rho^n}{a^n} \phi^{n+1'} \psi' + \frac{\rho^n}{a^n} \phi^{n+1} \psi'' \right] du = 0.
\end{aligned} \tag{3.2}$$

We note that we have further integrated by parts the term involving H' to lower the smoothness requirements of the theory. Replacing Eq. 3.1 into 3.2 and choosing the test function $\psi = B_I$, we obtain N discrete equations for $\phi_J,\ I = 1, \dots N$ as

$$\sum_{J=1}^{N} \left[M_{IJ} + \Delta t^n K_{IJ}(\phi^{n+1}) \right] \phi_J^{n+1} = \xi \int_0^1 a^n \rho^n \phi^n B_I \, du, \tag{3.3}$$

where

$$
\begin{aligned}
M_{IJ} &= \xi \int_0^1 a^n \rho^n B_I B_J \, du \\
K_{IJ}(\phi^{n+1}) &= \int_0^1 \frac{\rho^n}{a^n}\left(\chi^{\text{eff}}\phi^{n+1} + \frac{k_B T \phi_m}{\phi_m - \phi^{n+1}}\right) B_I' B_J' \, du \\
&\quad + \int_0^1 a_p \kappa \bar{C} H^n \left[\left(\frac{\rho^n}{a^n}\right)' B_I' B_J + \left(\frac{\rho^n}{a^n}\right) B_I' B_J' + \left(\frac{\rho^n}{a^n}\right) B_I'' B_J\right] du \\
&\quad + \int_0^1 \frac{\Lambda \phi^{n+1}}{a^n \rho^n}\left[\left(\frac{\rho^n}{a^n}\right)' B_I' + \frac{\rho^n}{a^n} B_I''\right]\left[\left(\frac{\rho^n}{a^n}\right)' B_J' + \frac{\rho^n}{a^n} B_J''\right] du \\
&\quad + \int_0^1 \Lambda \, L(\phi^{n+1}) B_I' B_J' \, du.
\end{aligned}
\tag{3.4}
$$

Since the matrix K_{IJ} depends on the unknown, the system of equations in Eq. 3.3 is nonlinear and we solve it using Newton's method.

To solve the mechanical problem, we fix protein area fraction to ϕ^{n+1} and write down an incremental Lagrangian accounting for the rate of change of the free energy, for membrane dissipation, and for local area and volume constraints

$$
\begin{aligned}
\mathcal{L}_m[\rho^{n+1}, z^{n+1}, \sigma^{n+1}, p^{n+1}] = &\frac{\mathcal{F}[\rho^{n+1}, z^{n+1}; \phi^{n+1}] - \mathcal{F}[\rho^n, z^n; \phi^{n+1}]}{\Delta t^n} \\
&+ \mathcal{D}_m\left[\frac{\rho^{n+1} - \rho^n}{\Delta t^n}; \rho^n, z^n\right] - \frac{p^{n+1}}{\Delta t^n}(V^{n+1} - V^n) \\
&+ \frac{1}{\Delta t^n}\int_0^1 \sigma^{n+1}(a^{n+1}\rho^{n+1} - a^n \rho^n) 2\pi \, du.
\end{aligned}
\tag{3.5}
$$

The Lagrange multiplier σ^{n+1} is also discretized in space using B-splines. However, rather than cubic, we use quadratic B-spline basis functions for this field to obtain a stable formulation [95, 96]. To move forward in time, we obtain the mechanical unknown at time t^{n+1} by numerically solving the algebraic optimization problem

$$
\{\rho_I^{n+1}, z_I^{n+1}, \sigma_I^{n+1}, p^{n+1}\} = \underset{\tilde{p}^{n+1}, \tilde{\sigma}_I^{n+1}}{\text{argmax}} \; \underset{\tilde{\rho}_I^{n+1}, \tilde{z}_I^{n+1}}{\text{argmin}} \; \mathcal{L}_m[\tilde{\rho}_I^{n+1}, \tilde{z}_I^{n+1}, \tilde{\sigma}_I^{n+1}, \tilde{p}^{n+1}].
\tag{3.6}
$$

As described above, this Lagrangian method will in general lead to significant distortions of the numerical grid. For robustness and accuracy of the numerical methods, we periodically perform mesh reparametrizations of the generating curve.

Chapter 4

Numerical experiments

In this Chapter we examine a series of specific numerical examples that reproduce the main processes realted to the protein-membrane complex: curvature sensing, curvature generation and the intimate chemo-mechanical positive feedback of the membrane-protein system. We introduce two variants of the continuum model proposed in Chapter 2, one accounting for protein's bending elasticity and the other addressing membrane bending by crowding of bulky off-membrane protein domains [97, 98].

4.1 Selection of parameters

We choose as the energy scale the bending rigidity of the membrane $\kappa = 20\ k_BT$. As the length and time-scales, we choose $\ell_0 = 50$ nm and $\tau_p = \ell_0^2\xi/(k_BT)$. Considering a membrane viscosity of $\eta = 5 \cdot 10^{-9}$ N s/m and the relation $\xi = 2\pi\eta$ discussed in Section 2.3, we obtain that $\xi \approx 3 \cdot 10^{-8}$ N s/m, the diffusion coefficient of proteins is $D = k_BT/\xi \approx 1.3 \cdot 10^{-13}$ m^2/s and $\tau_p \approx 0.02$ s. In the absence of measurements, we choose $\Lambda/a_p = 1k_BT$ large enough so that, when phase separation occurs, domain boundaries have a finite thickness and simulations are devoid of numerical oscillations indicative of ill-

conditioning, and small enough so that the dynamics of the problem are not significantly affected by this parameter. With these units, in our calculations we set the non-dimensional coefficients $\bar{\kappa} = 1$, $\bar{\bar{C}} = 2$ (corresponding to $1/\bar{C} \approx 25$ nm), $\bar{a}_p = 0.04$ (corresponding to $a_p \approx 100$ nm^2), $\overline{k_B T}/\bar{a}_p = 1.25$, $\bar{\xi}/\bar{a}_p = 1.25$ and $\bar{\eta} = 1/(40\pi)$. We finally note that, to avoid numerical solutions with unreasonably thin necks, thinner than the bilayer thickness, we introduce a term that limits the minimum radius of a neck structure to about $\epsilon \sim 7.5$ nm by adding an energy contribution of the form

$$\mathcal{F}_{\text{neck}} = \int_{\Gamma_s} \frac{\gamma}{(\rho - \epsilon)^2}\, dS, \tag{4.1}$$

where Γ_s is the entire surface excluding a small region near the poles and $\gamma = 0.1\ k_B T$. We checked that this potential only affected the solutions close to the neck.

4.2 Curvature sensing and generation starting from a prolate vesicle

Curvature sensing is a phenomenon by which curved membrane proteins migrate to regions of the membrane with higher/preferred curvature. Hence, a necessary condition is the existence of a curvature gradient. We first considered a prolate vesicle as shown in Fig. 4.1(a). This vesicle is obtained by minimization of bending energy at constant area $S = 4\pi R_0^2$, with $R_0 = 500$ nm, at fixed reduced volume $v = 0.93$. At $t = 0$, the vesicle is covered with a homogeneous area fraction of curved proteins ($\bar{\phi} = 0.15$) with spontaneous curvature $\bar{C} = 1/25$ nm^{-1}. We assume that the proteins are non-interacting and thus choose $\chi = -a_p \kappa \bar{C}^2$ so that $\chi^{\text{eff}} = 0$. The initial homogeneous distribution of proteins is preferred entropically, but is not optimal from the point of view of bending energy, which favors protein migration towards the poles. The competition between these two free energy contributions leads to a non-uniform chemical potential of proteins and drives protein transport. Since $\nabla\phi = \mathbf{0}$ at $t = 0$, protein transport is initially due exclusively to gradients in curvature with the diffusive velocity coinciding with the drift velocity

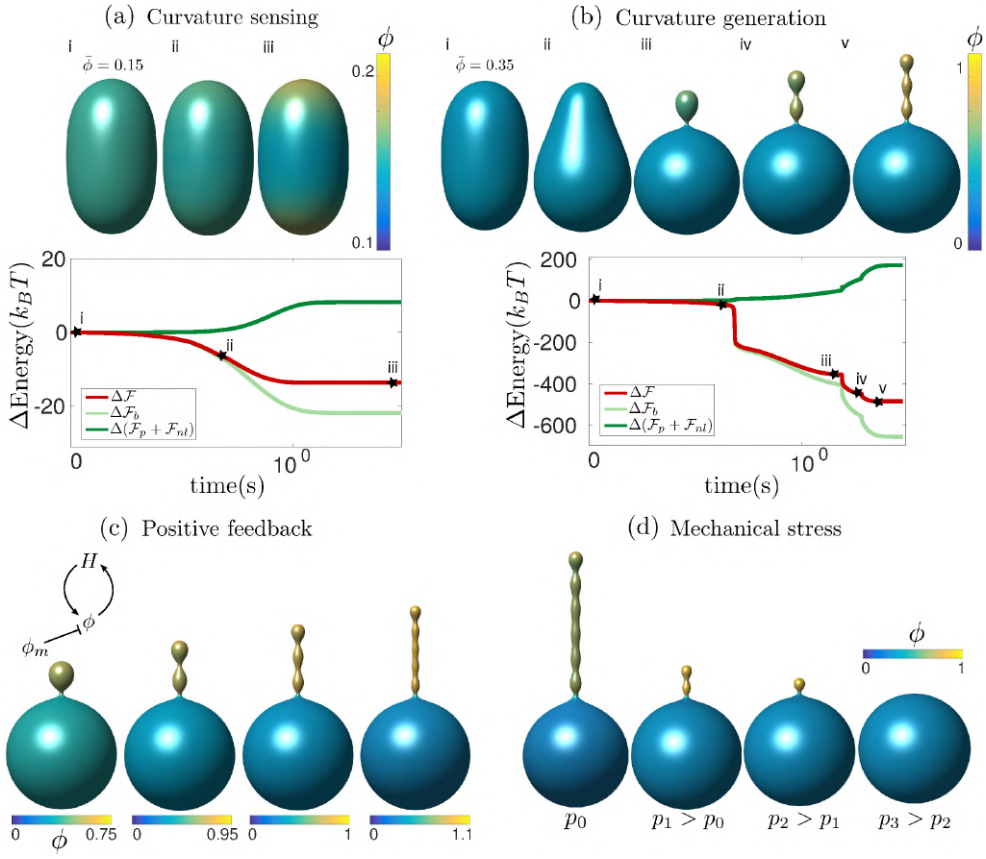

Figure 4.1: Snapshots of shape and protein coverage during the relaxation dynamics on a prolate membrane vesicle, and time evolution of changes in energies (total, bending and chemical) for an average and initially uniform protein area fraction of (a) $\bar{\phi} = 0.15$ and (b) $\bar{\phi} = 0.35$. (c) Final equilibrium states depending on the saturation density $\phi_m = \{0.75, 0.95, 1, 1.1\}$, which stops the feedback between curvature generation and protein transport. (d) Equilibrium states as vesicle pressure is incremented by steps, while allowing for volume changes, showing a mechanically-induced dissolution of a highly curved and protein-rich membrane domain.

$\boldsymbol{w}^{\text{drift}} = a_p \kappa \bar{C} \nabla H / \xi$. Estimating the average gradient of mean curvature from the prolate shape, we estimate the time required for drift transport to induce a gradient in protein density as $\tau_1 \approx R_0 / |\boldsymbol{w}^{\text{drift}}| \approx 0.3$ s. Sub-

sequently, the dynamics are governed by a competition between drift and diffusive transport, driving proteins towards equilibrium over a time scale $\tau_2 \approx R_0^2/D(\bar{\phi}) \approx 1.36$ s. Thus, we estimate that the total time scale of relaxation is given by $\tau \approx \tau_1 + \tau_2 \approx 1.66$ s. These estimates are consistent with the results shown in Fig. 4.1(a), where we show a few selected snapshots of protein distribution during the equilibration dynamics, along with the time-evolution of the changes in the total energy, $\Delta\mathcal{F}$, and of different components of it. The figure shows that equilibration takes place in a time commensurate to τ, and that protein migration towards the poles is driven by bending energy, which decreases during the dynamics, but opposed by $\mathcal{F}_p + \mathcal{F}_{nl}$. In this example, where the total number of proteins on the membrane is low, their area fraction in the protein-rich poles is far from the saturation area fraction $\phi_m = 1$ and membrane shape does not change.

To examine the ability of proteins to generate membrane shape, we revisited the previous example but increased the amount of protein by setting an initial homogeneous area fraction of $\bar{\phi} = 0.35$, see Fig. 4.1(b). At early times, the dynamics parallel those of the previous example, with drift motion of proteins towards the poles, followed by balancing diffusive fluxes. However, now the amount of protein creates a sufficiently large spontaneous curvature $\bar{C}\phi$ to modify the shape of the vesicle, which develops a symmetry-breaking transition (ii). At this point, a positive feedback is established during which higher curvature attracts more proteins, which in turn locally increase curvature, and so on. We observe that during this process, the systems develops a cascade of rapid pearling events of duration τ_m, which create new curvature gradients and thus are followed by the partial equilibration of protein coverage over a time-scale of τ_p. Similar pearled tubular morphologies have been experimentally and computationally observed in bilayers with isotropic spontaneous curvature caused by anchored polymers [14, 99], in cells as a result of crowding of the grycocalyx [15] or by asymmetric lipid swelling due to changes in pH [100]. We note that if proteins induce anisotropic spontaneous curvature, for instance because they are elongated and adopt nematic order, experiments and molecular models suggest that one can expect tubular

protein-rich protrusions of uniform radius [9, 37, 41] rather than pearled protrusions as we find here. We leave models capturing nematic ordering of curved proteins for future work. This pearling cascade and positive feedback loop between curvature and protein coverage continues until proteins almost reach their saturation density ϕ_m in the highly curved domain. In equilibrium, the system reaches a heterogeneous state where a protein-rich and highly curved pearled tube coexists with a depleted vesicle.

To further examine the role of the saturation area fraction ϕ_m in setting the equilibrium state, we repeated the previous simulation considering different values of ϕ_m. Figure 4.1(c) shows that the depth of the pearling cascade is indeed controlled by this parameter. For $\phi_m = 0.75$, the saturation density and equilibrium is reached after the first pearl has formed. As the saturation area coverage is increased, the number of pearls, and the tube length and curvature progressively increase. Thus, in a model governed by the energies in Eqs. (2.6,2.7), protein saturation controlled by ϕ_m limits the positive feedback loop between curvature and area coverage.

Curvature generation by membrane proteins involves recruitment of membrane area into protein-rich protrusions, and therefore should depend on membrane tension as shown experimentally [24]. To examine this mechanical coupling, we started from an equilibrium state showing a highly curved protein-rich tube and increased the pressure difference in steps, thus allowing for volume changes in the vesicle. Initially, $p_0 = 13$ Pa and $\sigma^{\text{eff}} \approx 0.003$ mN/m. Figure 4.1(d) shows that as pressure, and thus tension, increase, membrane area is released from the protein-rich tube, which becomes shorter and more concentrated ($p_1 = 55$ Pa, $p_2 = 65$ Pa). Beyond $p_3 = 250$ Pa corresponding to $\sigma^{\text{eff}} \approx 0.064$ mN/m, the entire protrusion is eliminated and the proteins uniformly spread over the membrane. This example thus shows the mechanically-induced dissolution of a protein-rich curved domain.

The transition between states of low curvature and homogeneous protein distribution and localized states has been classically analyzed assessing the linear stability of the uniform state [50, 24], summarized in Appendix A.2. According to this analysis, a purely mechanical instability (Euler buckling)

takes place when $\sigma^{\text{eff}} < 0$, while a purely chemical instability (phase separation) takes place when $D(\bar{\phi}) < 0$, see Eq. (2.28). In addition to these standard instabilities, the system can also exhibit a chemo-mechanical instability involving shape and protein patterning, which in the ideal case of a planar infinite membrane can happen when Appendix (A.2) [24]

$$\kappa|\bar{C}| - \left[\frac{\kappa}{a_p}\underbrace{\left(\chi^{\text{eff}} + \frac{k_B T \phi_m}{(\phi_m - \bar{\phi})\bar{\phi}}\right)}_{a^{\text{eff}}}\right]^{\frac{1}{2}} \geq \sqrt{\frac{\sigma^{\text{eff}}\Lambda}{a_p}}. \tag{4.2}$$

This equation allows us to understand qualitatively the mechanically-induced disappearance of a mechano-chemical pattern as σ^{eff} increases in Fig. 4.1(d), as well as the emergence of such a pattern when $\bar{\phi}$ increases as in Fig. 4.1(a,b), where $\chi^{\text{eff}} = 0$.

4.3 Sensing on a tube and shape stabilization

To further study the mechano-chemistry of membrane-protein interactions, we then considered a setup that mimics controlled in-vitro experiments, where a curvature gradient is established by pulling a highly curved membrane tether out of a vesicle [22, 101, 32, 20]. We consider the same vesicle size and reduced volume as in the previous examples, and gradually increase the distance between the poles. As in experiments [102], our simulations show that beyond an extension, the system breaks symmetry and a thin tube elongates from one of the poles, see Fig. 4.2(a)-i. Starting from this configuration, we load the vesicle with a uniform distribution of proteins with area coverage $\bar{\phi} = 0.15$. The protein dynamics are similar to the previous examples, with a progressive enrichment of the highly curved tube over a time period of about the diffusive time-scale $\tau_2 \approx 4\pi R_0^2/D(\bar{\phi}) \approx 17$ s, where now proteins need to migrate a longer distance on average to one of the two poles, Fig. 4.2(c). At equilibrium and for this low protein coverage, proteins have barely modified the shape of the vesicle-tube system, Fig. 4.2(a)-iii. However, their presence has a noticeable mechanical effect in the force required to keep the tether in place, which

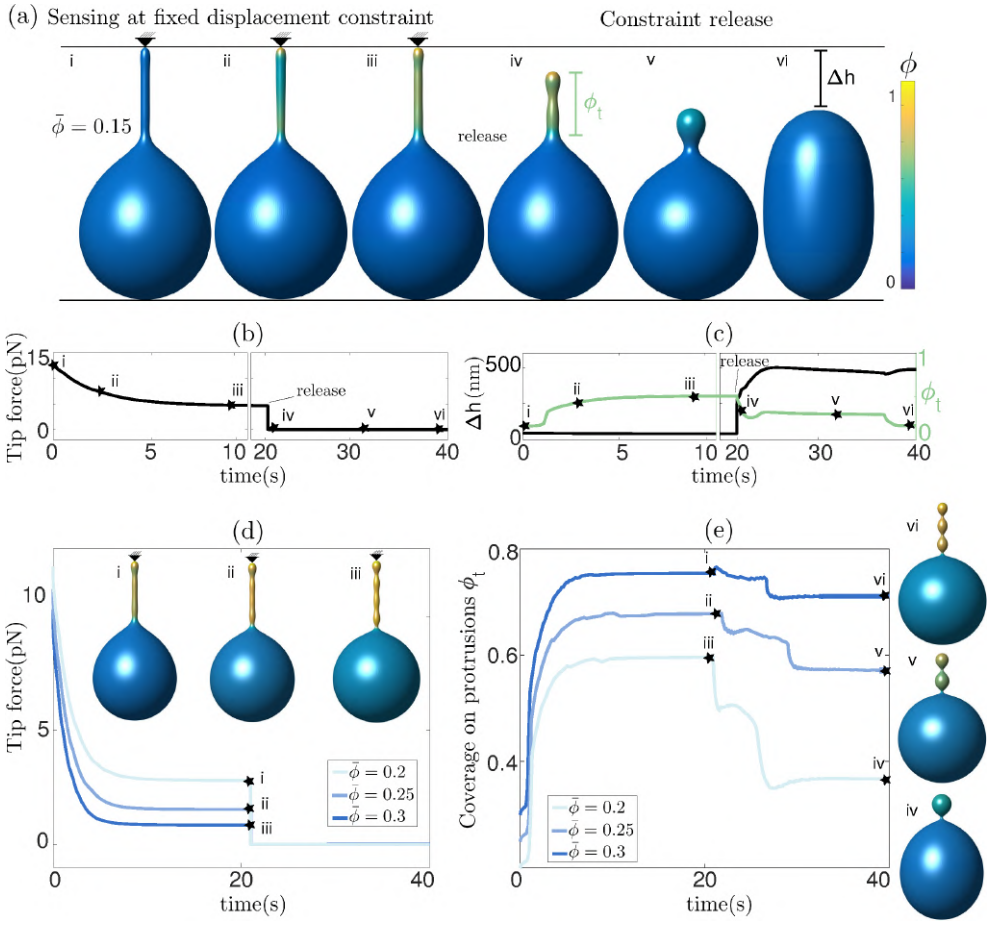

Figure 4.2: (a) Dynamics of curvature sensing by proteins on a vesicle with a tube stabilized by a displacement constraint at a lower average density $\bar{\phi} = 0.15$. Dynamics of the reaction force (b), average tubular density ϕ_t and height changes (Δh) (c) before and after the release of the displacement constraint. (d) Evolution of reaction force for higher average densities $\bar{\phi} = \{0.2, 0.25, 0.3\}$ and (e) average tubular density for different average densities showing a density-dependent stabilization of protein-rich curved protrusions.

decreases by more than two-fold, Fig. 4.2(b). This kind of behavior has been experimentally observed for BAR proteins and dynamin [22, 20, 101]. For this protein coverage, however, the amount of protein is insufficient to stabilize the

tube and following the release of the displacement constraint, the tube retracts and the protein-rich domain dissolves into the vesicle, Fig. 4.2(a-c). At higher protein coverage, the proteins drawn to the tube are able to modify visibly its shape by inducing slight pearling, they further reduce the tether force, and the larger protein amount is able to stabilize highly curved and protein-rich protrusions upon release of the constraint, Fig. 4.2(d,e), in agreement with in-vitro experiments [20, 101]. Furthermore, the transition to a strongly pearled protrusion upon force removal (iii-iv) closely mimics the shape transformations in membrane protrusions bent by crowding of the glycocalyx upon disassembly of enclosed actin filaments [15].

4.4 Bud formation and tension-induced dissolution

Buds constitute a prototypical membrane motif, and are involved in endo/exocytosis [103] or in tensional buffering of the plasma membrane through caveolae [5]. Although the formation of such buds requires the synergistic interaction of multiple proteins and lipids, they can be abstracted as curved protein-rich membrane domains [87, 104]. To understand the fundamental mechanism of bud formation, we consider a flat discoidal patch of membrane covered with a homogeneous distribution of proteins ($\bar{\phi} = 0.1$) at $t = 0$. We assume that the membrane is flat at its edge and that proteins cannot flow in or out from the boundary. We apply radial tractions at the boundary corresponding to an isotropic membrane tension of $\sigma^{\text{eff}} \approx 3 \cdot 10^{-3}$ mN/m, at the lower end of membrane tension in mammalian cells [105].

According to Eq. (4.2), the parameters $\bar{C} = 2/25$ nm^{-1} and $a^{\text{eff}}/a_p \approx 0.4$ mN/m should make the initially uniform and flat state unstable, leading to a chemo-mechanical pattern. In agreement with this prediction from the linear stability analysis, our nonlinear, yet axisymmetric, calculations show the spontaneous formation of a budded protein-rich domain as shown in Fig. 4.3(a), reminiscent of caveolae. As shown in the figure, this process leads to a significant reduction in the projected area of the membrane patch, and thus during bud formation chemical energy is released to perform mechanical work against

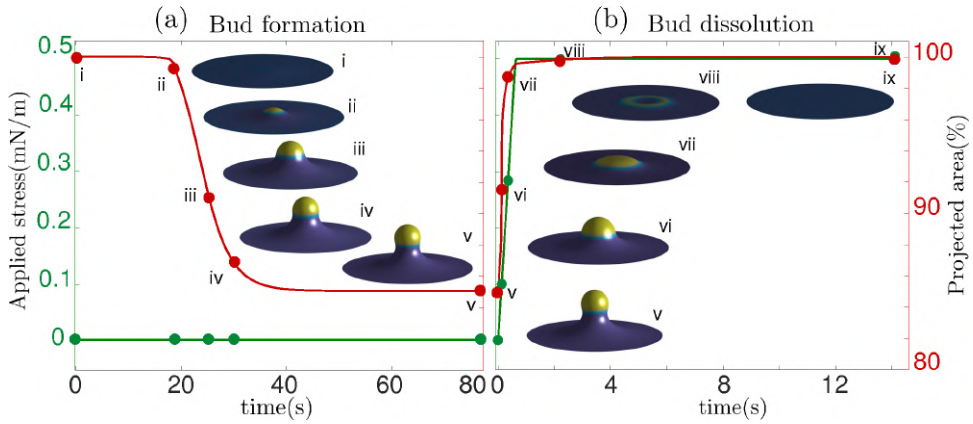

Figure 4.3: (a) Spontaneous formation of budded protein-rich domain from a flat membrane with homogeneously distributed proteins in the initial state and (b) dissolution of the bud under sudden stress increase, releasing projected membrane area.

the applied tension.

A critical function of caveolae is the mechano-protection of cells subjected to stretching of the plasma membrane [5]. These budded domains provide a membrane reservoir, which upon tension increase, can be released to buffer membrane tension and avoid lysis [106]. To test the ability of our model to reproduce this phenomenology, we suddenly increased membrane tension to 0.5 mN/m within 0.6 s. As a result and in agreement with Eq. (4.2), the budded domain rapidly disassembles, leaving a flat patch with uniformly distributed proteins, Fig. 4.3(b), consistent with the increased mobility of caveolar components following tension-induced disassembly [5].

4.5 Two alternative models of membrane-protein interaction

Proteins with bending elasticity

The curvature model considered up to this point, based on Eq. (2.6), assumes that protein cooperativity increases the spontaneous curvature of the surface.

However, an alternative model can be conceived in which curved proteins have a stiffness of their own, which results in an effective density-dependent stiffness of the protein shell on the membrane [48]. In this case, the curvature energy of the composite membrane-protein system can be written as

$$\mathcal{F}_b = \int_\Gamma \frac{\kappa}{2} H^2 \, dS + \int_\Gamma \frac{\kappa_p(\phi)}{2} (H - C_p)^2 \, dS, \tag{4.3}$$

where C_p is the intrinsic curvature of proteins and $\kappa_p(\phi)$ a density-dependent stiffness of the protein coat. The resulting membrane shape is hence the result of the competition between elastic bending energies of proteins and of the lipid bilayer. This model has been used to study the response of membranes with stiff protein coats [107]. Assuming a linear dependence of κ_p on the protein area fraction, $\kappa_p(\phi) = \bar{\kappa}_p \phi$, and a chemical energy given by Eqs. (2.7,2.8) as before, the chemical potential of proteins now takes the form

$$\mu = \mu_0 + a_p \bar{\kappa}_p (H - C_p)^2 + k_B T \log \frac{\phi}{\phi_m - \phi} + \chi\phi - \Lambda \Delta \phi. \tag{4.4}$$

Invoking Onsager's principle with the same dissipation potentials as before, we obtain an alternative protein transport equation

$$\xi \dot{\phi} + \nabla \cdot \left[a_p \bar{\kappa}_p (C_p - H) \nabla H \phi - \left(\chi\phi + \frac{k_B T \phi_m}{\phi_m - \phi} \right) \nabla \phi + \Lambda \phi \nabla (\Delta \phi) \right] = 0, \tag{4.5}$$

where the density-dependent diffusion coefficient

$$D(\phi) = \frac{1}{\xi} \left(\chi\phi + \frac{k_B T \phi_m}{\phi_m - \phi} \right) \tag{4.6}$$

has the same structure as the one in Eq. 2.28. In contrast, the drift velocity $\boldsymbol{w}^{\text{drift}} = a_0 \bar{\kappa}_p (C_p - H) \nabla H / \xi$ is now qualitatively different, in that its sign relative to ∇H can change in space and time depending on the sign of $C_p - H$, whereas in the previous model ($\boldsymbol{w}^{\text{drift}} = a_0 \kappa \bar{C} \nabla H / \xi$) it just depended on the sign of the constant $\bar{C}$. Focusing on the case in which both $\bar{C}$ and C_p are positive for concreteness, in the model based on Eq. (2.6) the drift term always favors protein transport towards regions of higher curvature, whereas in the model based on Eq. (4.3) this will be the case only as long as membrane

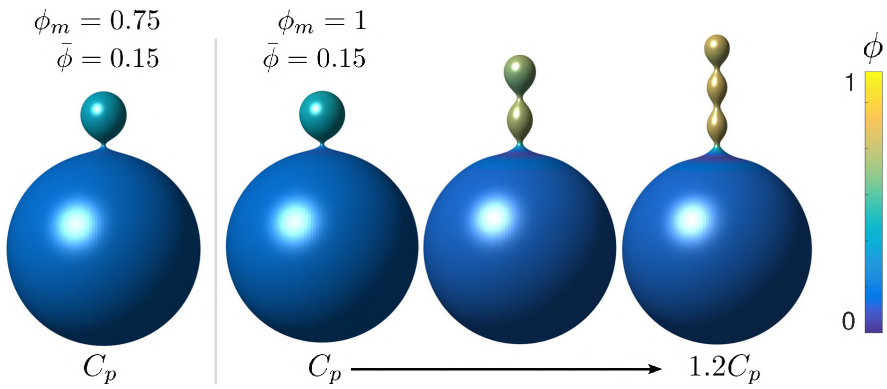

Figure 4.4: Comparison of the equilibrium shapes obtained for different values of the saturation area fraction ϕ_m and spontaneous curvature C_p for the model governed by the bending energy in Eq. (4.3).

curvature is smaller than the preferred protein curvature. As a result, in the model presented in this Section the positive feedback between curvature and protein coverage stops once membrane curvature reaches C_p. Recall that, as discussed in Section 4.2, in the previous model this positive feedback was only stopped by the saturation of protein coverage as ϕ approached ϕ_m. We tested this idea computationally by examining the equilibrium shape predicted by the model based on Eq. (4.3) with $\kappa_p = 40 k_B T$ and $C_p = 1/25$ nm^{-1}, of a slightly deflated vesicle with the same reduced volume $v = 0.93$ and an average protein concentration $\bar{\phi}$. Figure 4.4 shows that the system equilibrates at a state with a protein-rich domain where $H \approx C_p/2$ and where $\phi \approx 0.5$ is lower than $\phi_m = 0.75$. The curvature of the protein-rich domain is controlled by the competition of membrane and protein elasticity, which in turn depends on protein coverage. This calculation shows that in this model ϕ_m does not select the curvature of the protein-rich domain. To further confirm this, we observe that increasing $\phi_m = 1$ does not change the equilibrium state. In contrast, increasing C_p by 17.5% and 20% led to more curved protrusions with a larger number or pearls. Eventually, as protrusions become increasingly concentrated in protein at high values of C_p, protein density reaches saturation and hence ϕ_m starts playing a role.

Membrane bending by protein crowding

Up to this point, we have assumed that proteins interact at the mid-plane of the lipid membrane. However, this approximation clearly breaks down for membrane proteins with bulky disordered domains [13, 23] or anchoring long polymers [15]. In this situation, the interaction between proteins leading to bending can be overwhelmingly dominated by the entropic repulsion of these disordered domains/polymers, which interact a few nanometers away from the lipid membrane. Figure 4.5(a) illustrates this mechanism.

Ignoring reconfigurations of the disordered domain/polymer blob [42], we assume that they interact on a surface Γ^+ at a distance d from the surface representing the lipid membrane, Γ. Thus, the free energy of the proteins can be written as

$$\begin{aligned}\mathcal{F}_p = &\int_{\Gamma^+} \frac{k_B T}{a_p}\Big[\phi^+ \log\big(\phi^+\big) + (\phi_m - \phi^+)\log\big(\phi_m - \phi^+\big)\Big]\, dS^+ \\ &+ \int_{\Gamma^+} \frac{\chi}{2a_p}(\phi^+)^2\, dS^+ + \int_{\Gamma^+} \frac{\mu_0}{a_p}\phi^+\, dS^+,\end{aligned} \tag{4.7}$$

where ϕ^+ is the area fraction of proteins on Γ^+, a_p is the area on this surface of each bulky protein domain, and ϕ_m is the saturation area fraction of bulky domains on Γ^+.

We next refer this energy to the bilayer mid-surface. If the separation between Γ and Γ^+ is small, $dH \ll 1$, then the area element of Γ^+ is related to that of Γ according to

$$dS^+ \approx (1 + dH)\, dS. \tag{4.8}$$

Denoting by $n^+ = \phi^+/a_p$ the number density of proteins on Γ^+, the above relation shows that we can express the number density on Γ using the relation $n^+ \approx n/(1 + dH) \approx n(1 - dH)$. This relation clearly shows how curvature changes density, as illustrated in Fig. 4.5(a) where positive/negative curvature increases/decreases n^+ at fixed n. Even if the area fraction does not make strict sense on Γ, we can formally define it on the bilayer mid-plane as $\phi = a_p n$

and hence

$$\phi^+ \approx \frac{\phi}{1+dH} \approx \phi(1-dH). \tag{4.9}$$

Denoting by $\boldsymbol{w}$ the diffusive velocity of proteins relative to the bilayer velocity at the membrane mid-plane, protein balance of mass is still given on Γ by Eq. (2.5).

Using Eqs. 4.8 and 4.9, noting that for small dH we have that $\log(1+dH) \approx dH$, further assuming that $\log[\phi_m - \phi(1-dH)] \approx \log(\phi_m - \phi) + \phi dH/(\phi_m - \phi)$, which holds true provided that ϕ is not too close to ϕ_m, and neglecting terms proportional to $(dH)^2$, we can rewrite Eq. (4.7) as integral over the lipid surface Γ as

$$\begin{aligned}\mathcal{F}_p = &\int_\Gamma \frac{k_B T}{a_p}[\phi\log\phi + (\phi_m-\phi)\log(\phi_m-\phi) + \phi_m dH\log(\phi_m-\phi)]\,dS \\ &+ \int_\Gamma \frac{\chi}{2a_p}\phi^2(1-dH)\,dS + \int_\Gamma \frac{\mu_0}{a_p}\phi\,dS.\end{aligned}$$

Combining this chemical energy with a simple Helfrich energy for the bare bilayer, $\mathcal{F}_b = \kappa/2\int_\Gamma H^2\,dS$, we obtain

$$\begin{aligned}\mathcal{F}_b + \mathcal{F}_p = &\int_\Gamma \frac{\kappa}{2}H[H-2C(\phi)]\,dS + \int_\Gamma \frac{k_BT}{a_p}[\phi\log\phi + (\phi_m-\phi)\log(\phi_m-\phi)]\,dS \\ &+ \int_\Gamma \frac{\chi}{2a_p}\phi^2\,dS + \int_\Gamma \frac{\mu_0}{a_p}\phi\,dS,\end{aligned} \tag{4.10}$$

where we have defined the protein-induced spontaneous curvature by crowding of off-membrane bulky domains/polymer blobs as

$$C(\phi) = \frac{d}{a_p\kappa}\left(\frac{\chi}{2}\phi^2 - k_BT\phi_m\log(\phi_m-\phi)\right). \tag{4.11}$$

The formal similarity between this expression for $\mathcal{F}_b + \mathcal{F}_p$ and that obtained in Section 2.2 is remarkable, the only difference being that before, the density-dependent spontaneous curvature was simply $C(\phi) = \bar{C}\phi$ and now it is given by Eq. (4.11). Note that the term proportional to $(\bar{C}\phi)^2$ in the bending energy

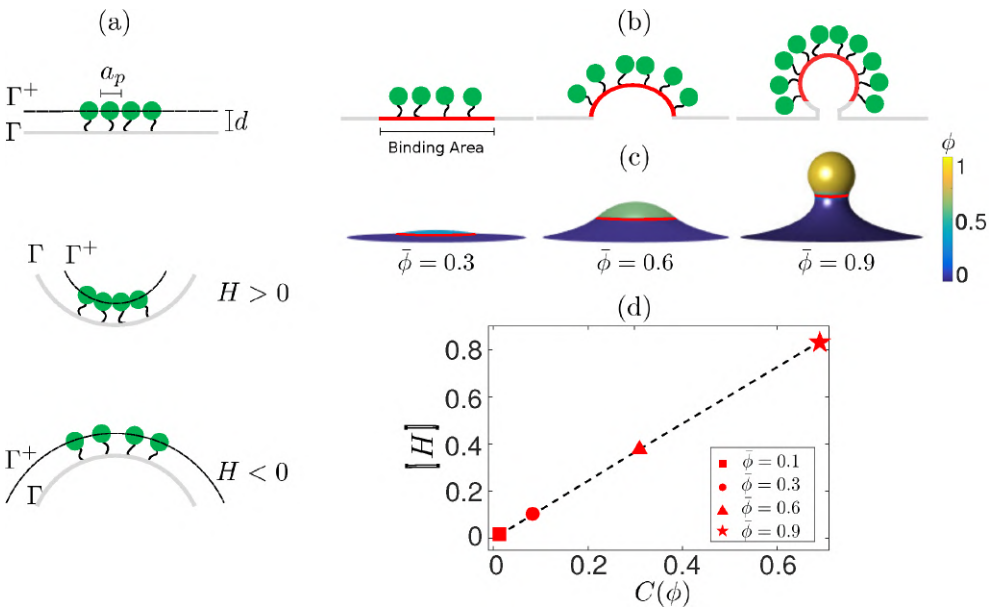

Figure 4.5: (a) Illustration of the model accounting for protein crowding of off-membrane bulky domains interacting on a surface Γ^+ located at a distance d from the bilayer mid-plane Γ. For a fixed number density n on Γ, the figure shows how positive/negative curvature leads to increase/decrease of area fraction of proteins on Γ^+. (b) If proteins are confined to a membrane domain (in red), then an increase in the number of proteins can be accommodated by membrane bending, which reduces the crowding of bulky domains. (c) Equilibrium configurations obtained by increasing the protein average area fraction within a region of constant area.(d) Corresponding jumps in mean curvature as a function of the density dependent spontaneous curvature $C(\phi)$.

of the previous model can be dropped by re-defining χ as χ^{eff}, and thus it does not affect the structure of the free energy.

In-vitro experiments examining membrane bending by protein crowding [13, 23] confined proteins to membrane domains. Not being able to diffuse freely, proteins became increasingly confined, leading to severe membrane remodeling. See Fig. 4.5(b). Here, we consider this situation, by allowing ϕ to differ from zero only over a subdomain $\Gamma_p \subset \Gamma$. Over the interface given by $\partial\Gamma_p$, we thus have an initial jump in protein area fraction of $\bar{\phi}$, the initial

average area fraction over the subdomain. Across the interface $\partial\Gamma_p$, forces and moments need to be continuous. Since the energy depends on curvature, jumps in the normal are not allowed but finite jumps in curvature are [108, 80]. Using the expression for the bending moment derived in Eq. 2.34 adapted to the free energy density in Eq. (4.10), continuity of bending moments across the interface leads to the condition $\kappa(H - C(\phi))|_i = \kappa H|_o$, where the subscripts indicate whether the quantity is evaluated on the inside or on the outside of the interface. We thus conclude that the jump in mean curvature across the interface needs to coincide with the protein-induced spontaneous curvature inside the protein-rich domain, $[\![H]\!] = C(\phi)$. To test these ideas, we considered various average protein area fractions, $\bar{\phi} = \{0.1, 0.3, 0.6, 0.9\}$, within a domain of diameter 250 nm in a membrane patch of diameter 2.5µm. We assumed that $d = 1$ nm and $\chi/a_p = 6$ mN/m (net repulsive protein-protein interaction). As shown in Fig. 4.5(c) increasing the number of proteins leads to increasing curvature, going from very shallow caps to buds, which in all cases very precisely follow the predicted relation for the jump in mean curvature, Fig. 4.5(d).

Chapter 5

Summary

In the first part of this thesis, we have proposed a novel theoretical and computational framework to model and simulate the coupled dynamics of lipid membranes and intrinsically curved proteins. In particular, we have focused on the shape transitions assumed by the lipid membranes and on the proteins distribution. More precisely,

- We have proposed a general continuum theory that analyzes the out-of-equilibrium configurations that lipid membranes assume when they interact with intrinsically-curved proteins. We have built the problem through the Onsager's formalism, a general framework for modeling dissipative systems, and the differential geometry of fluid deformable surfaces. The resulting governing equations exhibit a tight interplay between geometry and protein transport. We have particularized the problem to an axisymmetric configuration, which we have implemented numerically with a direct numerical approach.

- We have exercised the previous model in a selection of numerical simulations that capture the ability of the model to describe curvature sensing, generation, stabilization, and tension-induced disassembly of

protein-rich curved domains. We have proposed three variants of the model: a common model where spontaneous curvature is proportional to protein density develops a positive feedback between curvature and protein density, only stabilized by protein saturation. An alternative model accounting for the bending elasticity of the protein coat does not exhibit this feature. In this case, the positive feedback between membrane curvature and protein coverage stops once membrane curvature reaches the one of proteins. A variant of the model where bending is induced by crowding of bulky off-membrane protein domains is formally equivalent to the first model, albeit with a nonlinear relation between protein-induced spontaneous curvature and protein density.

Part II

Elongated and curved proteins

Chapter 6

Ordering of proteins on a plane: a density-dependence phase transition

---

In this Chapter we present a mean-field theory that describe the isotropic-to nematic-phase transition of elongated and curved molecules. To build the theory we adapt a recent work presented by [2] for hard ellipsoidal particles to the 2D case. The theory is a correction of the Onsager's classical theory that was limited to relatively low coverage and large aspect ratio of particles. The crucial difference with Onsager's study [109] is the enforcement of a compact support of the orientational probability distribution beyond a certain spatial density. In this scenario we consider elongated proteins (such as the ones containing BAR domains) to be 2D elliptical particles that do not overlap. We write the free-energy of these particles in terms of number density of proteins and their angular distribution. Through the solution of a nonlinear system of algebraic equations we are able to compute the free-energy density landscape as a function of protein coverage and nematic order. The theory exhibits the density-dependent discontinuous isotropic-to-nematic transition

on planar membranes. We also show how different aspect ratios of particles can affect the ordering transition and the maximum packing limit of a system.

6.1 Mean field approximation

We consider proteins to be 2D elliptical particles such that the length of their major and minor axes are given by $2a$ and $2b$ as shown in Fig. 6.1. The state of protein i, $\boldsymbol{q}_i$, is given by its position on a surface Γ, $\boldsymbol{r}_i$ and orientation over the unit circle $\mathbb{S}$, given by the angle γ_i of the long axis of the ellipse relative to a fixed direction on the surface. We assume that proteins are rigid, non-overlapping but otherwise non-interacting. Thus, for two particles with states $\boldsymbol{q}_1$ and $\boldsymbol{q}_2$, their interaction potential U is purely repulsive and can be defined as

$$U(\boldsymbol{q}_1, \boldsymbol{q}_2) = \begin{cases} \infty & \text{if particles overlap,} \\ 0 & \text{otherwise.} \end{cases} \tag{6.1}$$

The configurational free energy for N identical proteins up to additive constant is given by

$$\mathcal{F}_e = -\frac{1}{\beta} \ln \frac{1}{N!} \int_{\Omega^N} e^{-\beta \Sigma_{1 \le i < j \le N} U_{i,j}} \, d\boldsymbol{q}_1 \dots d\boldsymbol{q}_N, \tag{6.2}$$

where $\beta = 1/k_B T$ and Ω is the domain in phase space for each of the proteins, accounting for the translational and orientational degrees of freedom. Since all the proteins are equivalent, invoking a mean field approximation and a passage to the continuum limit (see [2] for further details), the free energy can be written as

$$\mathcal{F}_e = \frac{1}{\beta} \int_\Omega \rho(\boldsymbol{q}) \ln(\rho(\boldsymbol{q})) \, d\boldsymbol{q} - \frac{1}{\beta} \int_\Omega \rho(\boldsymbol{q}) \ln[1 - W(\boldsymbol{q})] \, d\boldsymbol{q} \tag{6.3}$$

where $\rho(\boldsymbol{q})$ is the number density of particles with state $\boldsymbol{q}$ and $W(\boldsymbol{q})$ is the average fraction of excluded area for a given particle, i.e. the fraction of phase space inaccessible to a particle due to presence of other particles. This quantity is postulated to take the form[2]

$$W(\boldsymbol{q}_1) = \lambda \int_\Omega \rho(\boldsymbol{q}_2) \left[1 - e^{-\beta U(\boldsymbol{q}_1, \boldsymbol{q}_2)} \right] \, d\boldsymbol{q}_2, \tag{6.4}$$

where λ is an adjustable parameter discussed in Fig. 6.1 accounting for the high-density packing. We note that in the dilute limit, the first term in Eq. (6.3) is dominant, and thus in this limit λ does not play an important role. We further express the number density of proteins in terms of positional and orientational contributions

$$\rho(\boldsymbol{q}) = \phi(\boldsymbol{r}) f(\boldsymbol{r}, \gamma), \tag{6.5}$$

so that $\int_{\mathbb{S}} f(\boldsymbol{r}, \gamma) d\gamma = 1$ and $\int_{\Gamma} \phi(\boldsymbol{r}) d\boldsymbol{r} = N$. Substituting the above relation into Eq. (6.4), we obtain

$$W(\boldsymbol{q}_1) = \lambda \int_{\mathbb{S}} \int_{\Gamma} \phi(\boldsymbol{r}_2) f(\boldsymbol{r}_2, \gamma_2) \left[1 - e^{-\beta U(\boldsymbol{r}_1, \gamma_1, \boldsymbol{r}_2, \gamma_2)}\right] \, d\boldsymbol{r}_2 \, d\gamma_2, \tag{6.6}$$

where we note that $d\boldsymbol{r}_2$ should be interpreted as the element of area on the surface Γ. Note that the term between square brackets is zero unless $\boldsymbol{r}_1$ and $\boldsymbol{r}_2$ are within a small distance commensurate to the particle size. Thus, assuming that ϕ varies slowly in this length-scale, it is reasonable to approximate $\phi(\boldsymbol{r}_2) f(\boldsymbol{r}_2, \gamma) \approx \phi(\boldsymbol{r}_1) f(\boldsymbol{r}_1, \gamma)$ in the equation above, finding

$$W(\boldsymbol{q}_1) = \lambda \phi(\boldsymbol{r}_1) \int_{\mathbb{S}} f(\boldsymbol{r}_1, \gamma_2) A_{\mathrm{e}}(\gamma_1, \gamma_2) \, d\gamma_2, \tag{6.7}$$

where $A_{\mathrm{e}}(\gamma_1, \gamma_2)$ is given by

$$A_{\mathrm{e}}(\gamma_1, \gamma_2) = \int_{\Gamma} \left[1 - e^{-\beta U(\boldsymbol{r}_1, \gamma_1, \boldsymbol{r}_2, \gamma_2)}\right] \, d\boldsymbol{r}_2. \tag{6.8}$$

The integrand in this expression is 0 unless the two particles overlap, in which case it is 1. It thus contains purely geometric information and can be interpreted as the excluded area per particle for two particles oriented along the angles γ_1 and γ_2. Note that, by translational invariance, it is independent of $\boldsymbol{r}_1$, and by rotational invariance is should depend on γ_1 and γ_2 through their difference.

Introducing Eqs. (6.5,6.7) into Eq. (6.3), we can write the configurational free energy of the system as

$$\begin{aligned} \mathcal{F}_e =& \frac{1}{\beta} \int_{\Gamma} \phi(\boldsymbol{r}) \ln \phi(\boldsymbol{r}) \, d\boldsymbol{r} \\ &+ \frac{1}{\beta} \int_{\Gamma} \phi(\boldsymbol{r}) \left\{ \int_{\mathbb{S}} f(\boldsymbol{r}, \gamma) \left[\ln f(\boldsymbol{r}, \gamma) - \ln g(\boldsymbol{r}, \gamma)\right] \, d\gamma \right\} \, d\boldsymbol{r}, \end{aligned} \tag{6.9}$$

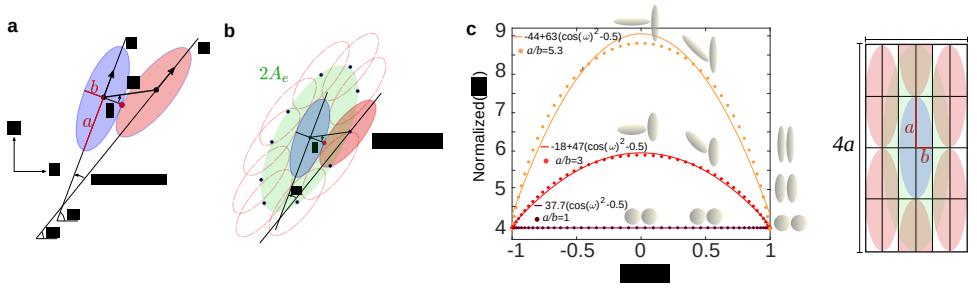

Figure 6.1: (a) Contact configuration of two ellipses in the plane. The modulus of the vector joining the centers, $R = |\boldsymbol{R}|$, is the so-called distance of closest approach for two ellipses whose major axis forms an angle $\omega = \gamma_1 - \gamma_2$, where γ_α is the orientation of each of the ellipses with respect to a fixed direction. This distance obviously depends on ω, on the length of the major and minor axes, $2a$ and $2b$, but also on the location of the contact point, parametrized by the angle ξ. (b) Illustration of the calculation of the excluded area (shaded in green) for a given ω. (c) Excluded area per particle for different ellipses of fixed area as a function of $\cos\omega$. The excluded area is normalized by the area of an ellipse πab and all the ellipses with different aspect ratios a/b have the same area. Elongated ellipses need to align to reduce the excluded area per ellipse. Dots represent the excluded area computed numerically with high accuracy while the solid line corresponds to a least-squares fit with the second-order polynomial approximation in Eq. (6.15). (d) Schematic view for the choice of λ in Eq. (6.4) estimated through the relation $a_{\text{eff}} = \lambda A_e$ [2], where a_{eff} is the average area effectively occupied by one particle in the rectangle and given by $a_{eff} = A_{rect}/N_{\text{particles}} = 4ab$ and A_e is the excluded area for a pair of particles with parallel long axis, $A_e = 4\pi ab$.

where we have defined

$$g(\boldsymbol{r}, \gamma) = 1 - \lambda\phi(\boldsymbol{r}) \int_{\mathbb{S}} f(\boldsymbol{r}, \gamma_2) A_{\text{e}}(\gamma, \gamma_2)\, d\gamma_2. \tag{6.10}$$

We note that for circular particles, this free energy reduces to that of a Van der Waals gas. We also note that, even though A_{e} is scale dependent (it has units of area), ϕ is also scale dependent in such a way that g is dimensionless and scale-independent.

6.2 Excluded area for two ellipses

To evaluate the free-energy in Eq. (6.9), we need to evaluate $A_{\text{e}}(\gamma_1, \gamma_2)$. For this, we note that the excluded area between two ellipses can be computed in

terms of the distance of closest approach R, see Fig. 6.1(a,b), as[110]

$$A_{\mathrm{e}}(\gamma_1, \gamma_2) = \frac{1}{2} \int_{\mathbb{S}} R^2(\omega, \xi, a, b)\, d\xi. \tag{6.11}$$

The calculation of $R(\omega, \xi, a, b)$ is algebraically complex[111]. It can be shown that R solves the equation

$$0 = 4(f_1^2 - 3f_2)(f_2^2 - 3f_1) - (9 - f_1 f_2)^2, \tag{6.12}$$

where

$$f_\alpha = 1 + G - \left(\frac{R}{a}\sin\theta_\alpha\right)^2 - \left(\frac{R}{b}\cos\theta_\alpha\right)^2, \quad \text{for} \quad \alpha = 1, 2, \tag{6.13}$$

with $\theta_1 = \xi$, $\theta_2 = \xi - \omega$, and

$$G = 2 + \left(\frac{a}{b} - \frac{b}{a}\right)^2 \sin^2\omega. \tag{6.14}$$

The above equations allow us to compute $A_{\mathrm{e}}(\gamma_1, \gamma_2)$ numerically, see Fig. 6.1(c), which shows how the dependence of the excluded area on particle alignment depends on the aspect ratio.

The average fraction of excluded area for a given particle $W(\boldsymbol{q})$ is only relevant at high packing but we are estimating it using the excluded area between two particles, A_{e}. To reconcile these two quantities through the parameter λ, we follow [2]. In a dense packing limit, such as in Fig. 6.1(d), $W(\boldsymbol{q})$ should approach 1, which we can express as the number density of particles $\phi = N_{\mathrm{particles}}/A_{\mathrm{tot}}$ times an effective area per particle a_{eff} in such a dense arrangement. We thus obtain $a_{\mathrm{eff}} = 4ab$. Examining Eq. (6.7), in this high-packing limit $1 \approx \lambda(N_{\mathrm{particles}}/A_{\mathrm{tot}})A_{\mathrm{e}}$, where A_{e} is the excluded area between two ellipsoidal particles with parallel long axis, i.e. $A_{\mathrm{e}} = 4\pi ab$. We thus conclude that $\lambda = 1/\pi \approx 1/3$.

Since $A_{\mathrm{e}}(\gamma_1, \gamma_2)$ depends on the orientations of the particles through $\omega = \gamma_1 - \gamma_2$, it can be approximated by an expansion of Legendre polynomials depending on $\cos\omega$ as

$$A_{\mathrm{e}}(\gamma_1, \gamma_2) = B_0 + B_2 P_2(\cos\omega) + \cdots \tag{6.15}$$

where B_0 and B_2 are constants depending on a and b, and $P_2(x) = x^2 - 1/2$. Note that by symmetry arguments, only even polynomials appear in the expansion. The expansion can be extended to higher order but the second-order approximation already provides a good approximation, see Fig. 6.1(c). Interestingly, the second order expansion allows us to express $A_e(\gamma_1, \gamma_2)$ in terms of the symmetric and traceless tensor

$$\boldsymbol{\sigma}(\gamma) = \frac{1}{2}\left[2\boldsymbol{\ell}(\gamma) \otimes \boldsymbol{\ell}(\gamma) - \boldsymbol{I}\right], \tag{6.16}$$

where $\boldsymbol{I}$ is the surface identity and $\boldsymbol{\ell}(\gamma)$ is the local orientation of proteins. The latter can be expressed in an arbitrary orthonormal frame of the tangent plane to the surface $\{\boldsymbol{\lambda}, \boldsymbol{\mu}\}$ as $\boldsymbol{\ell} = \cos\gamma\,\boldsymbol{\lambda} + \sin\gamma\,\boldsymbol{\mu}$, see Fig. 6.1. This tensor describes the local (or microscopic) second moment of the orientation of proteins, and as shown later, it leads to a theory where orientational order appears through the classical nematic tensor $\boldsymbol{Q}$.

By noting that $\boldsymbol{\ell}(\gamma_1) \cdot \boldsymbol{\ell}(\gamma_2) = \cos\omega$, a direct calculation shows from Eq. (6.15) that

$$\lambda A_e(\gamma_1, \gamma_2) = c - d\boldsymbol{\sigma}(\gamma_1) : \boldsymbol{\sigma}(\gamma_2), \tag{6.17}$$

where, $c = \lambda B_0$ and $d = -\lambda B_2$ depend on a and b and can be computed by fitting a second order polynomial in $\cos\gamma$ to $A_e(\gamma_1, \gamma_2)$.

6.3 Optimizing the orientational distribution

Given a density field ϕ, we can find the optimal angular distribution at each point in space $\boldsymbol{r}$ by minimizing the free energy in Eq. (6.9) with respect to f subject to the normalization constraint. To minimize the free energy and account for this constraint, we introduce the Lagrangian functional

$$\mathcal{L}[f, \mu] = \int_{\mathbb{S}} f\,(\ln f - \ln g)\,d\gamma + \mu\left(\int_{\mathbb{S}} f\,d\gamma - 1\right), \tag{6.18}$$

where μ is a Lagrange multiplier field. Since we perform this minimization point-wise, we drop for notational simplicity the dependence on $\boldsymbol{r}$ of f, g, μ, ϕ and all quantities depending on these fields.

Recalling Eq. (6.17), we have

$$g(\gamma) = 1 - \phi(c - d\boldsymbol{\sigma}(\gamma) : \boldsymbol{Q}), \tag{6.19}$$

where we have introduced the nematic tensor describing the average particle orientation

$$\boldsymbol{Q} = \int_{\mathbb{S}} f(\gamma)\boldsymbol{\sigma}(\gamma)\, d\gamma = \langle \boldsymbol{\sigma}(\gamma) \rangle \,. \tag{6.20}$$

Note that $\boldsymbol{Q}$ inherits from $\boldsymbol{\sigma}$ the properties of being symmetric and traceless. We further introduce the auxiliary tensor

$$\boldsymbol{\psi} = d\phi \int_{\mathbb{S}} \frac{f(\gamma)}{g(\gamma)} \boldsymbol{\sigma}(\gamma)\, d\gamma, \tag{6.21}$$

which is also symmetric and traceless. The stationarity condition can then be written as

$$0 = \delta_f \mathcal{L} = \int_{\mathbb{S}} (\ln f - \ln g - \boldsymbol{\psi} : \boldsymbol{\sigma} + \mu)\, \delta f d\gamma, \tag{6.22}$$

for all admissible variation δf, and thus the term between parentheses must vanish. It is clear that when $g \to 0$, then necessarily $f \to 0$. We can thus define the support of $f(\gamma)$ as $\mathbb{S}^+ = \{\gamma \in (-\pi, \pi) \text{ such that } g(\gamma) > 0\}$. Determining μ though the normalization of f, we find an expression for the angular probability density function

$$f(\gamma) = \begin{cases} \dfrac{g(\gamma) e^{\boldsymbol{\sigma}(\gamma):\boldsymbol{\psi}}}{\int_{\mathbb{S}^+} g(\gamma') e^{\boldsymbol{\sigma}(\gamma'):\boldsymbol{\psi}}\, d\gamma'} & \text{if } \gamma \in \mathbb{S}^+ \\ 0 & \text{otherwise.} \end{cases} \tag{6.23}$$

We note that this expression is far from being explicit, since g depends on $\boldsymbol{Q}$, which in turn depends on f, and $\boldsymbol{\psi}$ also depends on f. However, as developed below, it allows us to evaluate the free energy. We also note that the probability density function f vanishes in a region of the orientational space as the areal number density of proteins ϕ increases, and thus g in Eq. (6.19) becomes negative. As discussed in [2, 112], this is critical to quantitatively predict density based ordering for moderately elongated particles. Finally,

due to the symmetry of particles with respect to to rotations by π, it follows that $f(\gamma) = f(\gamma + \pi)$.

Since $\boldsymbol{Q}$ is symmetric and traceless, it has two real eigenvalues of opposite sign and it is diagonal in an orthonormal eigenframe. We let $\{\boldsymbol{\lambda}, \boldsymbol{\mu}\}$ be this eigenframe. Thus, the nematic tensor can be expressed as

$$\boldsymbol{Q} = \frac{S}{2}\left(\boldsymbol{\lambda} \otimes \boldsymbol{\lambda} - \boldsymbol{\mu} \otimes \boldsymbol{\mu}\right), \tag{6.24}$$

where we call S the order parameter, which contracting the above relation and Eq. (6.20) with $\boldsymbol{\lambda} \otimes \boldsymbol{\lambda}$ can be expressed as

$$S = \left\langle 2\left(\boldsymbol{\ell} \cdot \boldsymbol{\lambda}\right)^2 - 1 \right\rangle = 2\left\langle P_2(\cos\gamma)\right\rangle, \tag{6.25}$$

where γ is the angle between the nematic direction $\boldsymbol{\lambda}$ and the direction of a microscopic particle, $\boldsymbol{\ell}$. Combining Eqs. (6.16) and (6.24), we also find that $\boldsymbol{\sigma} : \boldsymbol{Q} = SP_2(\cos\gamma)$, and thus

$$g(\gamma) = 1 - \phi[c - dSP_2(\cos\gamma)]. \tag{6.26}$$

A traceless symmetric tensor such as $\boldsymbol{\psi}$ can be expressed in the eigenframe of $\boldsymbol{Q}$ as

$$\boldsymbol{\psi} = \frac{\psi}{2}(\boldsymbol{\lambda} \otimes \boldsymbol{\lambda} - \boldsymbol{\mu} \otimes \boldsymbol{\mu}) + \frac{\bar{\psi}}{2}(\boldsymbol{\lambda} \otimes \boldsymbol{\mu} + \boldsymbol{\mu} \otimes \boldsymbol{\lambda}). \tag{6.27}$$

We show next that in fact, $\{\boldsymbol{\lambda}, \boldsymbol{\mu}\}$ is also an eigenfame of $\boldsymbol{\psi}$, and thus $\bar{\psi} = 0$.

With the above representation of $\boldsymbol{\psi}$, we find that

$$\boldsymbol{\sigma} : \boldsymbol{\psi} = \psi P_2(\cos\gamma) + \bar{\psi}\sin\gamma\cos\gamma. \tag{6.28}$$

The condition that $\{\boldsymbol{\lambda}, \boldsymbol{\mu}\}$ is an eigenframe of $\boldsymbol{Q}$ implies that $0 = \boldsymbol{\lambda} \cdot \boldsymbol{Q} \cdot \boldsymbol{\mu}$ and hence

$$0 = \int_{\mathbb{S}^+} f(\gamma)\boldsymbol{\lambda} \cdot \boldsymbol{\sigma}(\gamma) \cdot \boldsymbol{\mu}\; d\gamma = \int_{\mathbb{S}^+} f(\gamma)\sin\gamma\cos\gamma\; d\gamma. \tag{6.29}$$

Noting that $\mathbb{S}^+$ is symmetric about $\gamma = 0$ since $g(\gamma)$ is an even function, Eq. (6.26), and using the symmetry $f(\gamma) = f(\gamma + \pi)$, the above relation

implies that

$$\begin{aligned}0 &= \int_{\mathbb{S}^+\cap(-\pi/2,\pi/2)} g(\gamma) e^{\boldsymbol{\sigma}(\gamma):\boldsymbol{\psi}} \sin\gamma\cos\gamma \; d\gamma \\ &= \int_{\mathbb{S}^+\cap(-\pi/2,\pi/2)} g(\gamma)\sin\gamma\cos\gamma\, e^{\psi P_2(\cos\gamma)} e^{\bar{\psi}\sin\gamma\cos\gamma} \; d\gamma \\ &= \int_{\mathbb{S}^+\cap(0,\pi/2)} g(\gamma)\sin\gamma\cos\gamma\, e^{\psi P_2(\cos\gamma)} \left(e^{\bar{\psi}\sin\gamma\cos\gamma} - e^{-\bar{\psi}\sin\gamma\cos\gamma}\right) d\gamma,\end{aligned}$$

where in the last step we have used the fact that $g(\gamma)\sin\gamma\cos\gamma\, e^{\psi P_2(\cos\gamma)}$ is an odd function of γ. Since in the integration domain $\mathbb{S}^+ \cap (0,\pi/2)$ the function $g(\gamma)$, $\sin\gamma$ and $\cos\gamma$ are strictly positive, it follows that the integral above is strictly positive if $\bar{\psi} > 0$ and strictly negative if $\bar{\psi} < 0$, and we thus conclude that $\bar{\psi} = 0$, that $\boldsymbol{Q}$ and $\boldsymbol{\psi}$ have the same eigenframe, and that $\boldsymbol{\sigma} : \boldsymbol{\psi} = \psi P_2(\cos\gamma)$.

Combining this last expression with Eqs. (6.23,6.25,6.26), we find that

$$S = 2\frac{\int_{\mathbb{S}^+} P_2(\cos\gamma)\left\{1-\phi\left[c-dSP_2(\cos\gamma)\right]\right\} e^{\psi P_2(\cos\gamma)} d\gamma}{\int_{\mathbb{S}^+}\left\{1-\phi\left[c-dSP_2(\cos\gamma)\right]\right\} e^{\psi P_2(\cos\gamma)} d\gamma}. \tag{6.30}$$

Importantly, the above relation provides an implicit relation for the auxiliary variable $\psi(\phi, S)$ given the particle number density ϕ and the order parameter S. With these expressions, the configurational free-energy in Eq. (6.9) can be rewritten as

$$\begin{aligned}\mathcal{F}_e[\phi,S] =& \frac{1}{\beta}\int_\Gamma \phi\Bigg\{ \ln\phi + \frac{S\psi}{2} \\ &- \ln\int_{\mathbb{S}^+}\left\{1-\phi\left[c-dSP_2(\cos\gamma)\right]\right\} e^{\psi P_2(\cos\gamma)} d\gamma\Bigg\} d\boldsymbol{r},\end{aligned} \tag{6.31}$$

in terms of the fields $\phi(\boldsymbol{r})$ and $S(\boldsymbol{r})$. We note that, given the lack of a preferred orientation, this effective free-energy depends on the nematic tensor $\boldsymbol{Q}$ only through S, and whenever $S \neq 0$, the nematic direction is arbitrary.

6.4 Free-energy landscapes on planar surfaces

Figure 6.2 shows the landscape of the energy density, the integrand in Eq. (6.31), as a function of density and order parameter. The figure shows that, as area

fraction becomes large, the energy grows rapidly irrespective of S and blows up at finite density, defining a region of inaccessible states where $g(\gamma)$, see Eq. (6.26), becomes negative. Given the density ϕ, we can minimize the energy profile with respect to S to determine the degree of order in equilibrium as a function of ϕ, defining the equilibrium path shown by red dots in the figure. For low area-fraction, proteins maximize their entropy by being randomly oriented and hence $S = 0$ is the only solution branch. As density increases beyond a threshold, we observe the emergence of another stable branch characterized by high protein order. There is a range of densities where both the disordered and the ordered branches coexist. Density-based ordering for such elliptical molecules thus proceeds through a first order phase transition. The procedure described here, which adapts that in [2] to 2D systems with elliptical particles, predicts how the energy landscape depends on the particle aspect ratio. As shown in Fig. 6.3, increasing it decreases the size of the region of accessible states, decreases the threshold density of the phase transition, and increases the maximum packing limit.

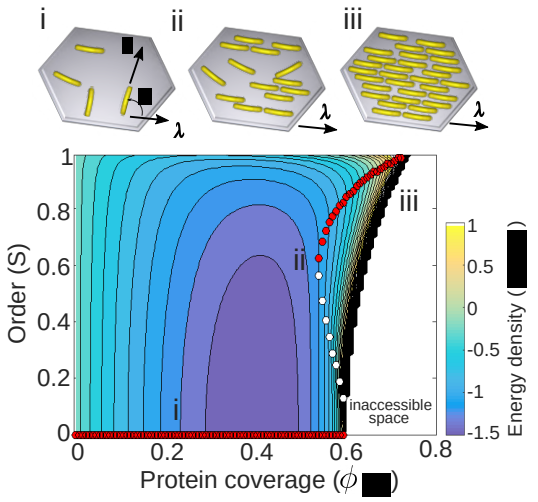

Figure 6.2: Free-energy density landscape as a function of protein coverage, expressed as the area fraction $a_p\phi$ with a_p the area of a protein, and of nematic order S. We consider ellipses with aspect ratio $a/b = 3$ on a flat membrane. Dots represent minima (red) and maxima (white) of the energy profile for fixed ϕ. The diagrams on top illustrate states i, ii and iii.

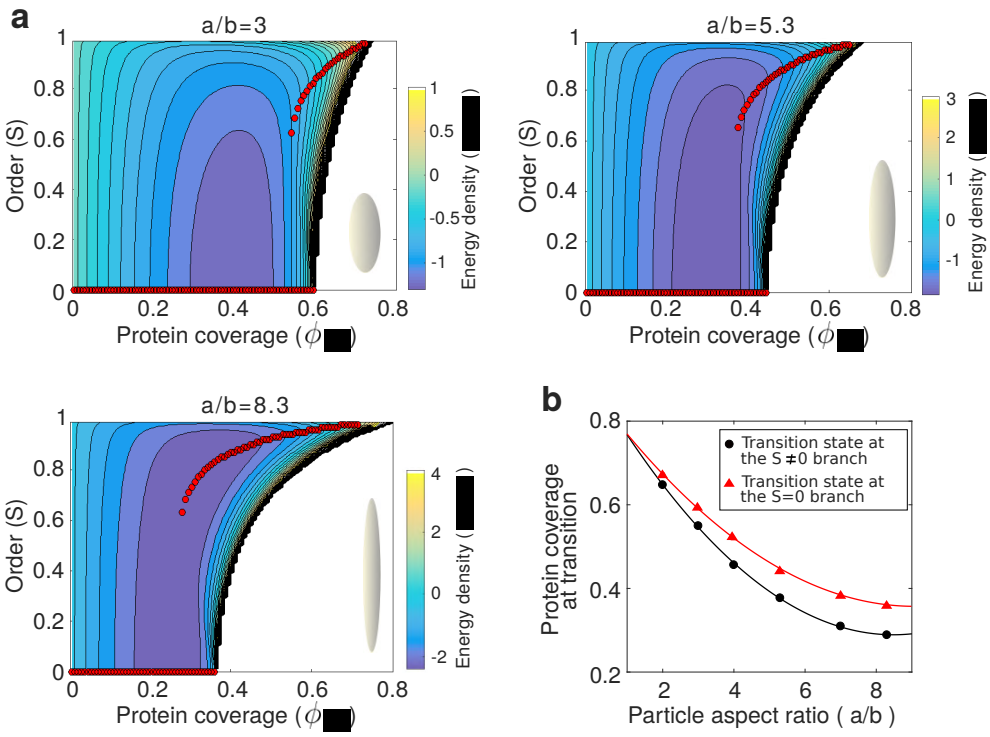

Figure 6.3: (a) Energy density landscape for ellipses with varying aspect ratio on a flat membrane. (b) Critical protein coverage for the isotropic-to-nematic transition for ellipses with varying aspect ratio on a flat membrane.

Chapter 7

Protein self-organization based on curved surfaces

Here, we extend the mean-field theory for the ordering of elongated and curved particles, presented in Chapter 6, to include the elastic curvature energy of proteins, that we consider to depend on their orientation and on the second fundamental form of the underlying surface. In particular, we examine how differently bent membranes can affect the isotropic-to nematic transition and we predict the ordering of molecules on spheres and cylinders of various radii. To complete the study we also look at the coexistence of phases (isotropic or nematic) in chemical equilibrium on planar membranes and on curved templates with negative Gaussian curvature.

7.1 Accounting for the bending energy and membrane curvatue

Having described the phase transition of ellipses on flat surfaces, we now consider curved proteins adhered to a curved lipid membrane approximated as a surface. We assume that the configurational free energy derived in the

previous section is not significantly affected by curvature. This is a reasonable approximation since Gaussian curvature, locally affecting the local metric of the surface, would need to be very large, in the order of $1/(ab)$, to significantly affect our calculation of excluded area.

Elongated membrane proteins can couple to curvature through various mechanisms acting at different planes. Shallowly inserting into the membrane, amphipathic domains can induce curvature by increasing monolayer packing or through a wedge effect. The charged and curved surface of a protein with high affinity with the membrane can create a scaffolding effect on the surface of the bilayer. Finally, attached polymers or partially disordered protein domains can induce a crowding effect at a distance off the membrane surface [113, 23, 15]. Since this latter mechanism strongly depends on density but should not depend much on protein orientation, we ignore it here and refer to other works where it is theoretically modeled [114, 42, 115, 15]. Focusing on the

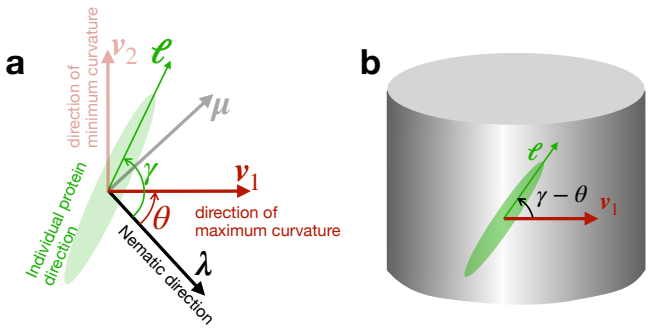

Figure 7.1: (a) Illustration of the eigenframe $\{\boldsymbol{\lambda}, \boldsymbol{\mu}\}$ of the nematic tensor $\boldsymbol{Q}$, where $\boldsymbol{\lambda}$ is the nematic direction, and of the eigenframe $\{\boldsymbol{v}_1, \boldsymbol{v}_2\}$ of the second fundamental form of the surface $\boldsymbol{k}$, where these vectors determine directions of maximum and minimum curvature of the surface. We also illustrate a microscopic direction $\boldsymbol{\ell}$, the angle γ between the nematic direction $\boldsymbol{\lambda}$ and $\boldsymbol{\ell}$, and the angle θ between the two eigenframes. (b) An adsorbed protein along vector $\boldsymbol{\ell}$ samples the normal curvature of the surface in this direction.

scaffolding and wedge effects, which should depend on protein orientation, we can compute the curvature of the membrane along the long axis of the protein given by vector $\boldsymbol{\ell}$, Fig. 7.1(b), as $k_{\boldsymbol{\ell}} = \boldsymbol{\ell} \cdot \boldsymbol{k} \cdot \boldsymbol{\ell}$ where $\boldsymbol{k}$ is the second fundamental

form of the surface characterizing its local curvature. Similarly, $k_{\boldsymbol{s}} = \boldsymbol{s} \cdot \boldsymbol{k} \cdot \boldsymbol{s}$ is the curvature of the membrane along the short protein axis given by $\boldsymbol{s}$.

With these directional curvatures at hand and assuming that the protein curvatures along and perpendicular to the long axis conform to the curvature of the underlying surface in these directions, we consider a natural form of the elastic bending energy of a protein as [116, 60, 37]

$$U^b = \frac{\kappa_\parallel a_p}{2}(k_{\boldsymbol{\ell}} - \bar{C}_\parallel)^2 + \frac{\kappa_\perp a_p}{2}(k_{\boldsymbol{s}} - \bar{C}_\perp)^2, \tag{7.1}$$

where $\kappa_\parallel$ and $\kappa_\perp$ are the bending rigidities (with units of energy) of a protein along its long and short axes, and where $\bar{C}_\parallel$ and $\bar{C}_\perp$ are the corresponding preferred curvatures.

To obtain more explicit expressions of $k_{\boldsymbol{\ell}}$ and $k_{\boldsymbol{s}}$, we note that both the nematic tensor $\boldsymbol{Q}$, see Eq. (6.20), and the second fundamental form of the surface are symmetric tensors, and hence they possess respective tangential orthonormal eigenframes, $\{\boldsymbol{\lambda}, \boldsymbol{\mu}\}$ for $\boldsymbol{Q}$ and one given by the principal curvature directions $\{\boldsymbol{v}_1, \boldsymbol{v}_2\}$ for $\boldsymbol{k}$, Fig. 7.1(a). The principal curvatures of the surface are the corresponding eigenvalues $\boldsymbol{k} \cdot \boldsymbol{v}_i = k_i \boldsymbol{v}_i$, $i = 1, 2$. In general, these two eigenframes are different and are rotated by an angle θ, Fig. 7.1(a), which can be assumed to lie in the interval $\theta \in (-\pi/2, \pi/2]$ since eigenvectors can be flipped. We can express one frame in terms of the other as $\boldsymbol{\lambda} = \cos\theta \boldsymbol{v}_1 - \sin\theta \boldsymbol{v}_2$ and $\boldsymbol{\mu} = \sin\theta \boldsymbol{v}_1 + \cos\theta \boldsymbol{v}_2$. From the definitions of angles γ and θ, the angle between the principal curvature direction $\boldsymbol{v}_1$ and a microscopic particle direction $\boldsymbol{\ell}$ is $\gamma - \theta$, and hence

$$k_{\boldsymbol{\ell}} = k_1 \cos^2(\gamma - \theta) + k_2 \sin^2(\gamma - \theta), \tag{7.2}$$

$$k_{\boldsymbol{s}} = k_1 \sin^2(\gamma - \theta) + k_2 \cos^2(\gamma - \theta). \tag{7.3}$$

These expressions thus show that the elastic bending energy of a protein Eq. (7.1) depends on the principal curvatures of the surface at the location of the particle, k_1 and k_2, and on the angle between the particle axis and the direction of maximum curvature, $\gamma - \theta$.

Combining this bending energy, or in principle any other protein bending energy depending on particle orientation, with the configurational free energy

discussed in Section 1 for N proteins, Eq. (6.1), we obtain the free energy

$$\mathcal{F}^* = -\frac{1}{\beta} \ln \frac{1}{N!} \int_{\Omega^N} e^{-\beta\left(\Sigma_{1\le i<j\le N} U_{i,j} + \Sigma_{1\le i\le N} U_i^b\right)} \, d\boldsymbol{q}_1 \dots d\boldsymbol{q}_N. \tag{7.4}$$

As shown in [117, 2], the above free energy can be approximated by the mean field energy

$$\mathcal{F}^* \approx \mathcal{F} = -\frac{1}{\beta} \ln \frac{1}{N!} \left\langle \int_{\Omega} e^{-\beta \sum_{2\le j\le N} U_{1,j}} e^{-\beta U_1^b} \, d\boldsymbol{q}_1 \right\rangle^N \tag{7.5}$$

$$= -\frac{1}{\beta} \ln \frac{1}{N!} \left(\int_{\Omega} \left\langle e^{-\beta \sum_{2\le j\le N} U_{1,j}} e^{-\beta U_1^b} \right\rangle \, d\boldsymbol{q}_1 \right)^N, \tag{7.6}$$

where in the second line we have changed the order of integration and where the ensemble average

$$\langle f \rangle = \int_{\Omega^{N-1}} f \, p(\boldsymbol{q}_2, \dots, \boldsymbol{q}_N) \, d\boldsymbol{q}_2 \dots d\boldsymbol{q}_N, \tag{7.7}$$

is with respect to the probability distribution of $N-1$ particles given by

$$p(\boldsymbol{q}_2, \dots, \boldsymbol{q}_N) = \frac{e^{-\beta\left(\Sigma_{2\le i<j\le N} U_{i,j} + \Sigma_{2\le i\le N} U_i^b\right)}}{\int_{\Omega^{N-1}} e^{-\beta\left(\Sigma_{2\le i<j\le N} U_{i,j} + \Sigma_{2\le i\le N} U_i^b\right)} \, d\boldsymbol{q}_2 \dots d\boldsymbol{q}_N}. \tag{7.8}$$

The mean free approximation is an upper bound to the exact free energy.

Unlike the hard-core repulsion energy, which depends on the configuration of other proteins, the bending energy of a protein molecule does not depend on the configuration of other proteins. We can thus write

$$\begin{aligned} \mathcal{F} &= -\frac{1}{\beta} \ln \frac{1}{N!} \left(\int_{\Omega} \left\langle e^{-\beta \sum_{2\le j\le N} U_{1,j}} \right\rangle e^{-\beta U_1^b} \, d\boldsymbol{q}_1 \right)^N \\ &= -\frac{1}{\beta} \ln \frac{1}{N!} \left(\int_{\Omega} [1 - W(\boldsymbol{q}_1)] e^{-\beta U_1^b} \, d\boldsymbol{q}_1 \right)^N \end{aligned} \tag{7.9}$$

or equivalently

$$\mathcal{F} = -\frac{1}{\beta} \ln \frac{1}{N!} \left(\int_{\Omega} [1 - W(\boldsymbol{q})] e^{-\beta U^b(\boldsymbol{q})} \, d\boldsymbol{q} \right)^N \tag{7.10}$$

with $W(\boldsymbol{q})$ as defined before in Eq. (6.4). Following [2], we discretize the phase space in subdomains $\Omega = \cup_i \Omega_i$, each with N_i particles, and obtain free energy within this domain $\mathcal{F}_i$ after using Stirling's approximation as

$$\mathcal{F}_i = -\frac{1}{\beta} \ln \left(\frac{1}{N_i} \int_{\Omega_i} [1 - W(\boldsymbol{q}_i)] e^{-\beta U^b(\boldsymbol{q}_i)} \, d\boldsymbol{q}_i \right)^{N_i}. \tag{7.11}$$

Thus, the total free energy is given by

$$\mathcal{F} = \sum_i \mathcal{F}_i = -\frac{1}{\beta} \ln \prod_i \left(\frac{1}{N_i} \int_{\Omega_i} [1 - W(\boldsymbol{q}_i)] e^{-\beta U^b(\boldsymbol{q}_i)} \, d\boldsymbol{q}_i \right)^{N_i}. \tag{7.12}$$

Assuming $N_i \approx \rho(\boldsymbol{q}_i) \Delta \boldsymbol{q}_i$ and passing onto the continuum limit, we obtain

$$\begin{aligned} \mathcal{F} = &\frac{1}{\beta} \int_\Omega \rho(\boldsymbol{q}) \ln \rho(\boldsymbol{q}) \, d\boldsymbol{q} - \frac{1}{\beta} \int_\Omega \rho(\boldsymbol{q}) \ln[1 - W(\boldsymbol{q})] \, d\boldsymbol{q} \\ &+ \int_\Omega \rho(\boldsymbol{q}) U^b(\boldsymbol{q}) \, d\boldsymbol{q}. \end{aligned} \tag{7.13}$$

Further, separating the particle density ρ into spatial and orientational components as mentioned in Eq. (6.5), we obtain the expression for free energy

$$\begin{aligned} \mathcal{F}[\phi, f] = &\frac{1}{\beta} \int_\Gamma \phi \ln \phi \, d\boldsymbol{r} + \frac{1}{\beta} \int_\Gamma \phi \left\{ \int_{\mathbb{S}} f \left[\ln f - \ln g \right] \, d\gamma \right\} d\boldsymbol{r} \\ &+ \int_\Gamma \phi \int_{\mathbb{S}} f U^b \, d\gamma \, d\boldsymbol{r}. \end{aligned} \tag{7.14}$$

As before, we find the optimal particle angle distribution f by minimizing the free energy, resulting in an effective energy that will depend on S as before, but now also on θ and hence on the full nematic tensor $\boldsymbol{Q}$. Analogously to before, we introduce the Lagangian

$$\mathcal{L} = \int_{\mathbb{S}} f \left[\ln f - \ln g + U^b \right] d\gamma + \mu \left(\int_{\mathbb{S}} f \, d\gamma - 1 \right). \tag{7.15}$$

Minimization with respect to f requires that

$$0 = \delta_f \mathcal{L} = \int_{\mathbb{S}} \left[\ln f - \ln g - \boldsymbol{\psi} : \boldsymbol{\sigma} + U^b + \mu \right] \delta f d\gamma, \tag{7.16}$$

where the auxiliary symmetric and traceless tensor $\boldsymbol{\psi}$ was defined in Eq. (6.21), and hence, with the same argument leading to Eq. (6.23), we find that

$$f(\gamma) = \frac{g(\gamma)\, e^{\boldsymbol{\sigma}(\gamma):\boldsymbol{\psi}}\, e^{-U^b}}{\int_{\mathbb{S}^+} g(\gamma')\, e^{\boldsymbol{\sigma}(\gamma'):\boldsymbol{\psi}}\, e^{-U^b}\, d\gamma'} \tag{7.17}$$

if $\gamma \in \mathbb{S}^+$ and 0 otherwise.

As before, we express $\boldsymbol{\psi}$ in the eigenframe of $\boldsymbol{Q}$ as

$$\boldsymbol{\psi} = \frac{\psi}{2}(\boldsymbol{\lambda}\otimes\boldsymbol{\lambda} - \boldsymbol{\mu}\otimes\boldsymbol{\mu}) + \frac{\bar{\psi}}{2}(\boldsymbol{\lambda}\otimes\boldsymbol{\mu} + \boldsymbol{\mu}\otimes\boldsymbol{\lambda}). \tag{7.18}$$

However, we cannot make the same argument as before to conclude that $\bar{\psi} = 0$ because, unless $\theta = 0$ or $\theta = \pi/2$, U^b is not an even function of γ, see Eqs. (7.2,7.1). Recalling Eq. (6.28), we can write the angular probability distribution

$$f(\gamma) = \frac{[1 - \phi\,(c - dSP_2)]\; e^{\psi P_2}\, e^{\bar{\psi}\sin\gamma\cos\gamma}\, e^{-U^b}}{\int_{\mathbb{S}^+} [1 - \phi\,(c - dSP_2)]\; e^{\psi P_2}\, e^{\bar{\psi}\sin\gamma'\cos\gamma'}\, e^{-U^b}\, d\gamma'}, \tag{7.19}$$

where P_2 stands for $P_2(\cos\gamma)$. In Section 1, we used Eq. (6.25) to determine ψ. Now, however, we need two equations since we also need to determine $\bar{\psi}$. For this, we recall that $0 = \boldsymbol{\lambda}\cdot\boldsymbol{Q}\cdot\boldsymbol{\mu}$ leading to Eq. (6.29). Thus, we have two conditions

$$\begin{aligned} 0 =& 2\int_{\mathbb{S}^+} P_2\,[1 - \phi\,(c - dSP_2)]\; e^{\psi P_2}\, e^{\bar{\psi}\sin\gamma\cos\gamma}\, e^{-U^b}\, d\gamma \\ & - S\int_{\mathbb{S}^+} [1 - \phi\,(c - dSP_2)]\; e^{\psi P_2}\, e^{\bar{\psi}\sin\gamma\cos\gamma}\, e^{-U^b}\, d\gamma, \qquad (7.20) \\ 0 =& \int_{\mathbb{S}^+} \sin\gamma\cos\gamma\,[1 - \phi\,(c - dSP_2)]\; e^{\psi P_2}\, e^{\bar{\psi}\sin\gamma\cos\gamma}\, e^{-U^b}\; d\gamma, \qquad (7.21) \end{aligned}$$

the second of which was trivially satisfied previously as the integrand is an odd function of γ for $\bar{\psi} = 0$ and $U^b = 0$. Now, however, these two relations provide a system of nonlinear equations to solve for ψ and $\bar{\psi}$.

Examining the above equations, it is clear that $f(\gamma)$, ψ and $\bar{\psi}$ depend on ϕ and S, but also on θ, k_1 and k_2 through U^b. Plugging Eq. (7.19) into

Eq. (7.14), we obtain a computable expression of the free energy accounting for the curvature energy of the proteins

$$\mathcal{F}[\phi, S, \theta, k_1, k_2] = \frac{1}{\beta}\int_\Gamma \phi\Big\{ \ln\phi + \frac{S\psi}{2} \\ - \ln\int_{\mathbb{S}^+} \{1 - \phi\,[c - dSP_2(\cos\gamma)]\}\, e^{\psi P_2(\cos\gamma)}\, e^{\bar{\psi}\sin\gamma\cos\gamma}\, e^{-U^b} d\gamma\Big\} d\boldsymbol{r}. \tag{7.22}$$

It is interesting to note that, as mentioned earlier, in the special case that the nematic direction $\boldsymbol{\lambda}$ is aligned with one of the principal directions, $\theta = 0$ or $\theta = \pi/2$, then $\bar{\psi} = 0$, U^b becomes an even function of γ, and hence $f(\gamma)$ is symmetric with respect to the nematic direction. For a general nematic orientation relative to the principal curvatures, however, f is not symmetric about the nematic direction.

We also note that, following a standard procedure, the chemical potential of proteins can be obtain by taking the functional derivative of Eq. (7.22) with respect to ϕ, and that subsequently a grand canonical thermodynamic potential can be defined where the chemical potential replaces ϕ as an independent variable. However, since ψ and $\bar{\psi}$ implicitly depend on ϕ through Eqs. (7.20,7.21), this calculation is not straightforward.

7.2 Optimizing θ

The free energy in Eq. (7.22) can then be minimized with respect to θ to yield an effective energy

$$\hat{\mathcal{F}}[\phi, S, k_1, k_2] = \min_{\theta\in(-\pi/2,\pi/2)} \mathcal{F}[\phi, S, \theta, k_1, k_2]. \tag{7.23}$$

This process identifies the energetically optimal nematic orientation relative to the curvature of the surface. To do that, we make $\mathcal{L}$ stationary with respect to θ to find

$$0 = \int_{\mathbb{S}^+} g(\gamma) e^{\boldsymbol{\sigma}:\boldsymbol{\psi}} e^{-U^b} \frac{\partial U^b}{\partial\theta}\, d\gamma. \tag{7.24}$$

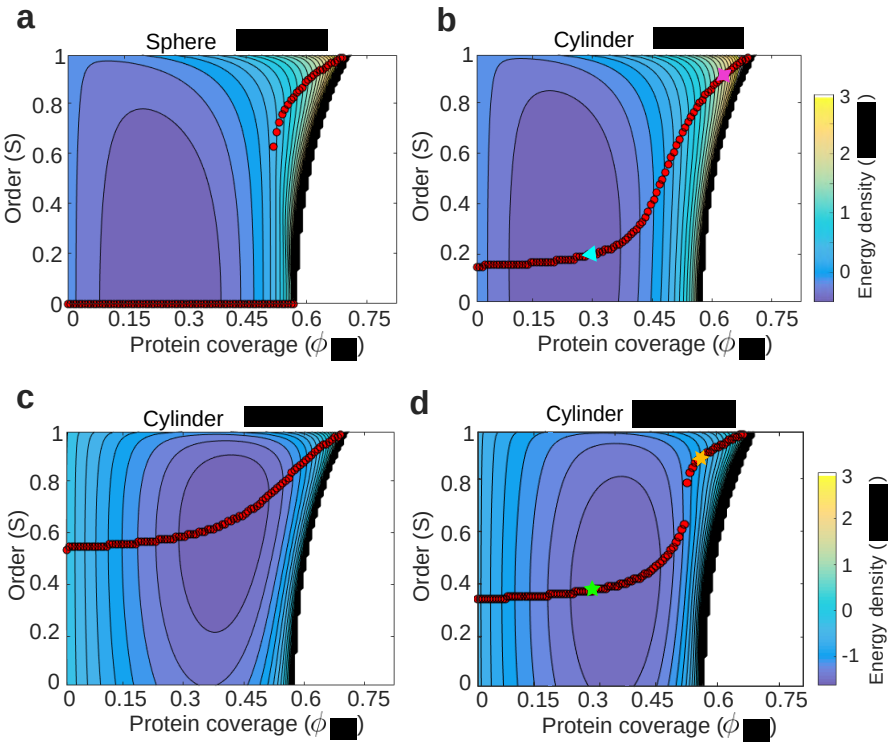

Figure 7.2: (a)-(d) Energy density contours as a function of density and order on spherical and cylindrical surfaces of different radii ($R = 150$ nm for the sphere, $R = 150, 15$ and 10 nm for cylinders), and for a protein preferred curvature of $\bar{C} = 1/15$ nm^{-1}. Red dots denote stable states, which minimize the free energy for a given protein coverage.

Expanding the last term in the integral, we find

$$0 = \int_{\mathbb{S}^+} g(\gamma) e^{\boldsymbol{\sigma}:\boldsymbol{\psi}} e^{-U^b} \left[k_1 \cos^2(\gamma-\theta) + k_2 \sin^2(\gamma-\theta) - \bar{C}\right] \\ (k_1 - k_2)\cos(\gamma-\theta)\sin(\gamma-\theta)\, d\gamma. \tag{7.25}$$

This equation, together with Eqs. (7.20,7.21), provides a system of three nonlinear equations for three unknowns, ψ, $\bar{\psi}$ and θ. For a sphere, $k_1 = k_2$, this equation is an identity showing that any direction is equally possible. Suppose that $\bar{\psi} = 0$ and $\theta = 0$. In this case, U^b is an even function of γ, Eqs. (7.21,7.25) are identically satisfied, and Eq. (7.20) provides an equation

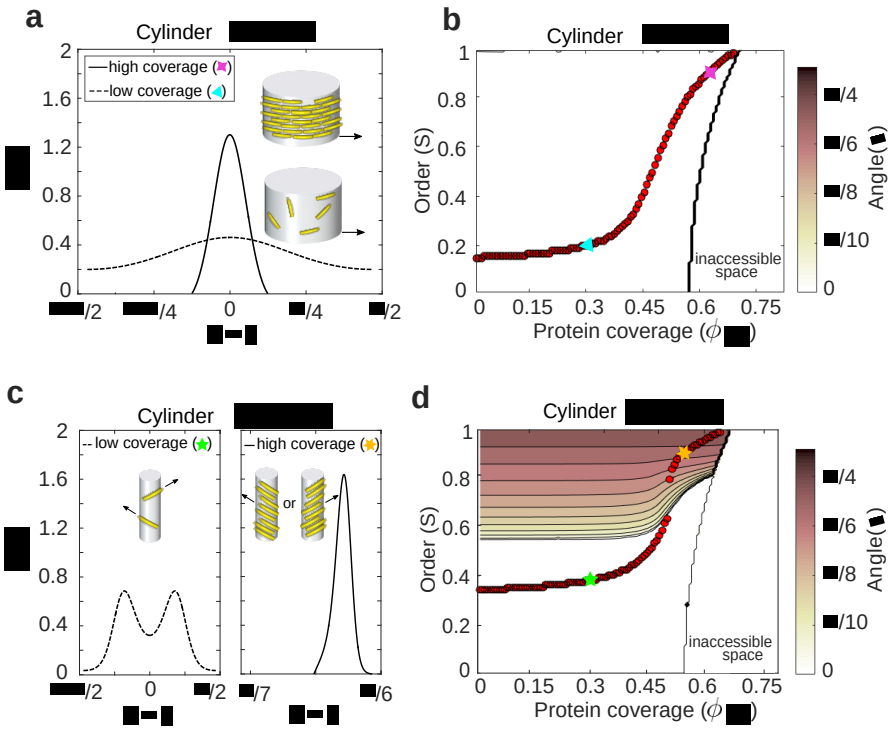

Figure 7.3: (a,c) Angular probability distribution $f(\gamma)$ plotted against $\gamma - \theta$, i.e. against the angle of a particle relative to the direction of maximum curvature of the cylinder $\boldsymbol{v}_1$, Fig. 7.1. The inset pictorially illustrates the state of the system, where the double-ended arrow indicates the nematic direction. (b,d) Protein net orientation expressed as the angle θ between the nematic direction and $\boldsymbol{v}_1$ as a function of density and order for the cylindrical surfaces in Fig. 7.2(b) and (d). In (b), $\theta = 0$ everywhere.

for ψ. Thus, there is always a solution with $\bar{\psi} = 0$ and $\theta = 0$ but in general there may be others and their relative stability must be examined to select the ground state.

7.3 Free energy landscapes on curved surfaces

In all the calculations, we choose $\kappa_\perp = 0$ and, unless otherwise stated, $\kappa_\parallel = 27\, k_B T$, in the order of recent estimates for I-BAR proteins using an assay based on unilamellar vesicles connected to membrane nanotubes and thermo-

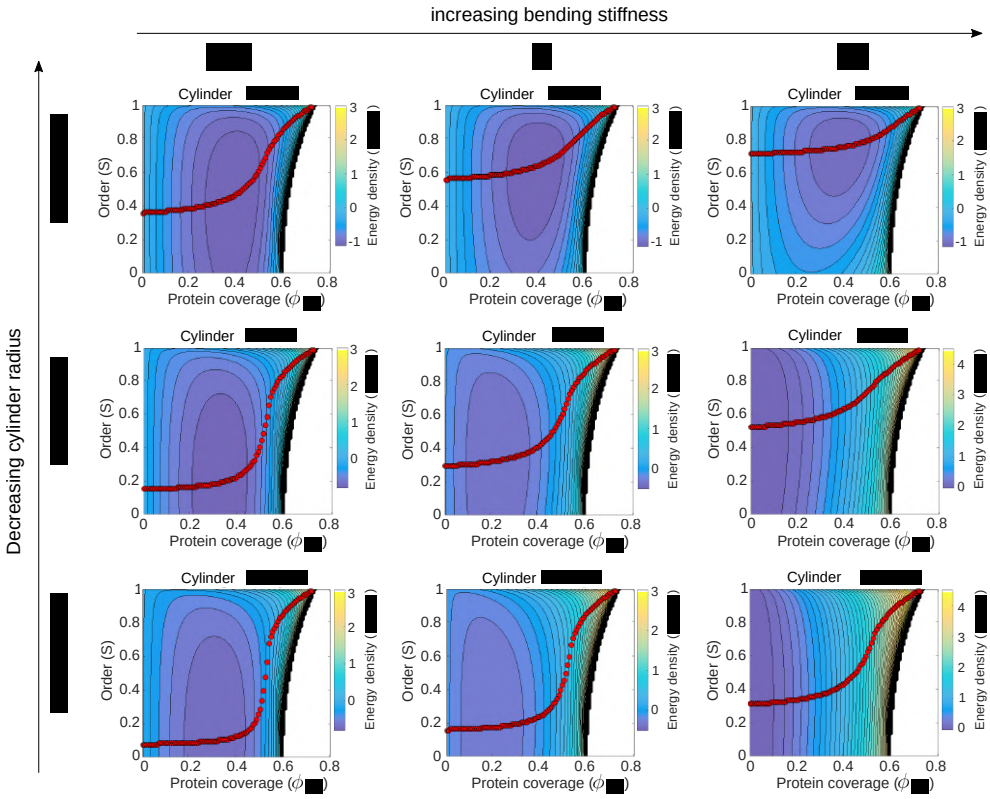

Figure 7.4: (a)-(d) Energy density contours as a function of density and order on cylindrical surfaces of different radii ($R = 150, 75$ and 15 nm, with $\bar{C} = 15$ nm^{-1}) considering different bending stiffnesses for the protein coat ($\kappa_{\parallel} = 27\ k_BT$, and half and twice of this value). Red dots denote stable states, which minimize the free energy for a given protein coverage.

dynamical models for protein-membrane interactions [118, 119] and comparable to previously used parameters in other theoretical models [120]. We also consider an aspect ratio of $a/b = 3$. The longitudinal preferred curvature $\bar{C}_{\parallel} = \bar{C}$ and the curvature of the surface is varied and indicated in each figure.

Energy density landscapes exhibiting the isotropic-to-nematic transition for proteins on spherical and cylindrical surfaces are shown in Fig. 7.2 (a-d) using the expression given by Eq. (7.22) and minimizing the energy with respect to θ (the angle between the net orientation of proteins and the max-

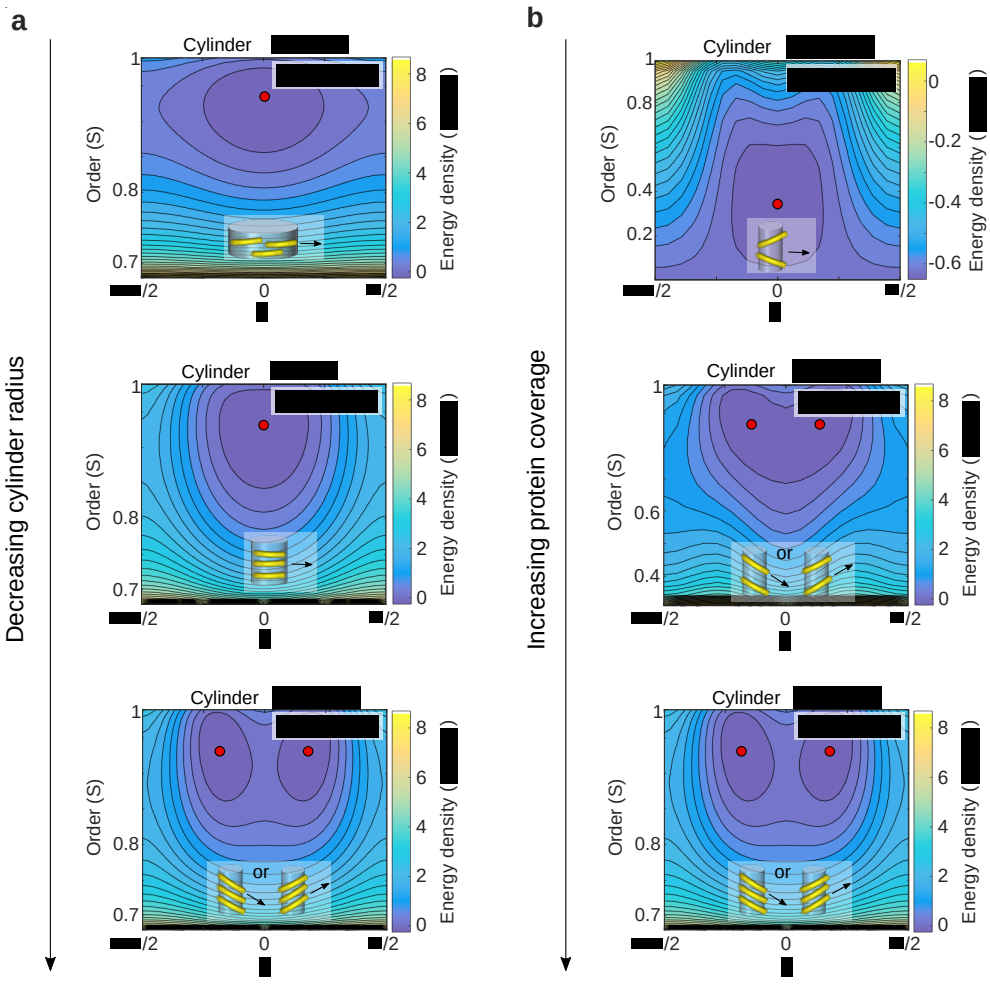

Figure 7.5: (a) Energy landscapes in the $(\theta - S)$ plane for high protein coverage ($\phi a_p = 0.66$) and cylinders of decreasing radius. (b) Energy landscape in the $(\theta - S)$ plane for a thin cylinder ($\bar{C}R = 2/3$) and varying coverage.

imum curvature direction) as described in the previous section. We depict stable equilibrium states minimizing the free energy for a given protein coverage with respect to S and θ with red dots. For a sphere, Fig. 7.2(a), the isotropic curvature does not bias alignment along any specific direction and hence the phase transition is solely driven by entropic interactions. In fact,

examining Eq. (7.14), it is clear that since U^b does not depend on orientation, the last bending term in the free energy density is simply linear in ϕ and hence does not alter the path of minimizers marked by red dots. As a result, the system shows the same discontinuous transition upon crowding as in the planar case.

On anisotropically curved surfaces such as cylinders with radius R, proteins are biased to orient along specific directions to favourably adapt their curvature to that of the underlying surface, Fig. 7.2(b-d). This creates a competition between a curvature-dependent bias and the entropic part of the free energy, which leads to partial order (finite S) even in the dilute limit. Furthermore, this curvature bias changes the character of the isotropic-to-nematic transition, which now becomes continuous. Not surprisingly, this effect is stronger on thinner tubes, Figs. 7.2(b-c) and 7.4, and for stiffer proteins, Fig. 7.4.

Our model not only provides the free energy landscape as a function of ϕ and S but also the nematic orientation relative to the direction of maximum curvature of the cylinder $\boldsymbol{v_1}$ (Fig. 7.1) given by θ and represented in Fig. 7.3(b,d), and the distribution of protein orientations $f(\gamma)$, which we represent relative to $\boldsymbol{v_1}$, i.e. against $\gamma - \theta$, Fig. 7.3(a,c). Figure 7.3(b) illustrates the observation that for $\bar{C}R \geq 1$ the optimal nematic orientation is always that of maximum curvature of the cylinder, $\theta = 0$. Figure 7.3(a) shows the angular distribution for two values of protein coverage marked in (b). Both distributions are unimodal and symmetric about the direction given by $\boldsymbol{v_1}$ but as coverage increases, order increases as well and the distribution becomes more localized and compactly supported.

For cylinders with higher curvature than that of proteins, $\bar{C}R < 1$, the situation is more complex since now proteins aligned with $\boldsymbol{v_1}$ will be bent beyond their spontaneous curvature whereas proteins forming an angle α with $\boldsymbol{v_1}$ given by $\cos^2\alpha = \bar{C}R$, see Eq. 7.2, will store no elastic energy. The isotropic-to-nematic transition becomes discontinuous again, Fig. 7.2(d), and the nematic direction is along $\boldsymbol{v_1}$ for low S but θ becomes different from zero for larger order, Fig. 7.3(d). Interestingly, at low densities when $\theta = 0$, the angular distribution is bimodal, broad, and symmetric about $\boldsymbol{v_1}$, indicating a state

where proteins are disordered but preferentially adopt orientations forming a finite angle with the direction of maximum curvature, which is too curved compared to the protein curvature. This detailed information is lost if the nematic state is described in terms of a moment of f such as the nematic tensor $\boldsymbol{Q}$ or equivalently S and θ alone, rather than in terms of the full distribution. For high density, we find that the system adopts a non-symmetric, very narrow and compactly supported distribution (or a symmetry-related distribution), indicative of a nematic state with nematic direction forming a finite angle with $\boldsymbol{v_1}$, consistent with the fact that F-BAR proteins at high coverages adopt increasingly helical arrangements on increasingly thinner tubes [28].

The symmetry-breaking transition for thin tubes at high coverages can be nicely examined through free energy maps at given coverage and radius as a function of θ (the angle between nematic direction and $\boldsymbol{v}_1$) and S. On the one hand, we can observe how at fixed high-coverage and as the cylinder radius decreases, a single minimum given by $\theta = 0$ splits into two minima given by $\theta = \pm\theta_0$ when $\bar{C}R < 1$, Fig. 7.5(i). Similarly, given a high-curvature cylinder, as coverage increases the optimal nematic direction switches from being aligned with $\boldsymbol{v}_1$ to adopting either one of two symmetry-related orientations, Fig. 7.5(j).

We finally note that the model proposed here can be used to quantify the free energy of curved elongated particles on other surfaces, such as those of negative curvature.Figure 7.8 shows the isotropic-to-nematic transition on surfaces with locally zero mean curvature, i.e. surface with principal curvatures equal in magnitude and opposite in sign. The results are similar to those on cylinders, albeit with a larger bias towards nematic states, compare Fig. 7.2(b,c) and Fig. 7.8(a-c).

7.4 Coexistence of isotropic and nematic phases

Coarse-grained simulations suggest the possibility of coexistence between isotropic and nematic phases [37]. To examine such coexistence using our theory, we first consider the situation of a flat membrane. Figure 7.6(a) shows the land-

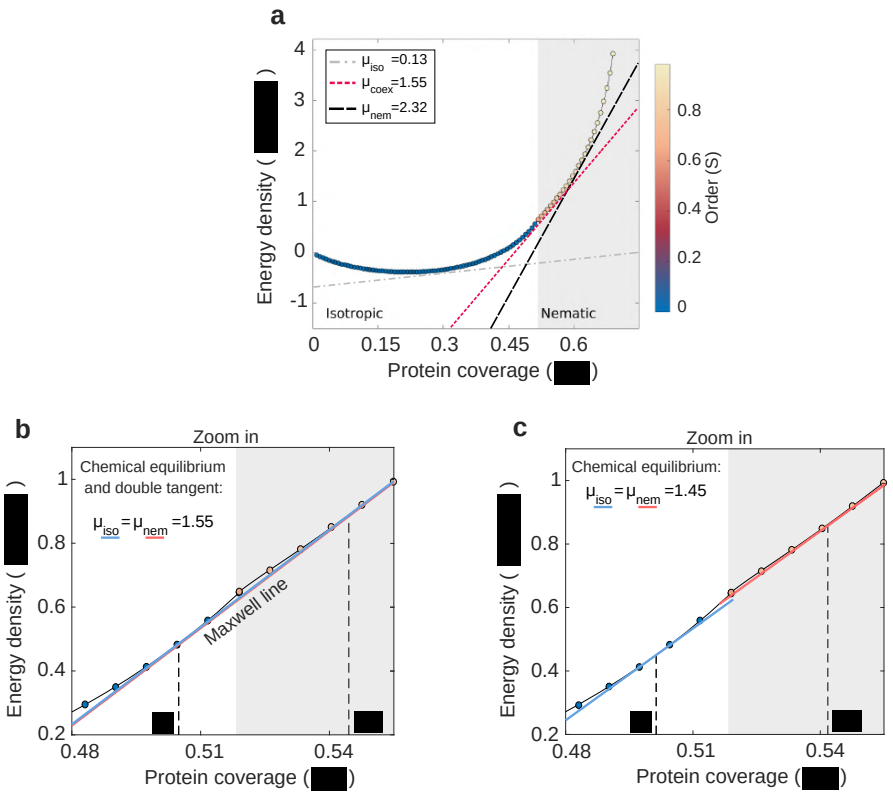

Figure 7.6: (a) Lowest energy density as a function of protein coverage for ellipses on a flat membrane, i.e. the energy along the minimum-energy path marked with red dots in Fig. 6.2. The color code represents order, highlighting the parts of the energy landscape corresponding to isotropic and to nematic phases. The slopes of the tangent lines represent the rate of change of energy density with respect to protein coverage, i.e. the chemical potential. The red line is doubly tangent (a Maxwell line) to the isotropic and nematic branches and represents a situation of coexistence in which protein number is fixed, see zoom in (b). If proteins can be exchanged with a bulk solution where they have a given chemical potential, then coexistence of isotropic and nematic phases does not require the double tangency constraint (c).

scape of minimum free energy as a function of protein coverage, which as discussed earlier and shown here with the color representing order, has an isotropic and a nematic branch. The slope of the energy density as a function of protein coverage is precisely the chemical potential of proteins in a

given state. For coexistence of isotropic and nematic phases in equilibrium, the chemical potentials of the two phases should be equal. If the number of proteins populating these two phases is fixed with average density $\bar{\phi}$, then coexistence additionally requires the double tangency condition, see Fig. 7.6(a,b) and the line with slope μ_{coex} following the Maxwell construction. Thus, under these conditions, coexistence is possible only when $\phi_{\text{iso}} < \bar{\phi} < \phi_{\text{nem}}$. When the membrane can exchange proteins with a bulk solution with chemical potential μ_{bulk}, the double tangency condition is no longer required and coexistence requires simply that $\mu_{\text{bulk}} = \mu_{\text{iso}} = \mu_{\text{nem}}$, see Fig. 7.6(c). This slightly relaxes the possibility of coexistence but the figure shows that it can only occur in a rather narrow range of densities.

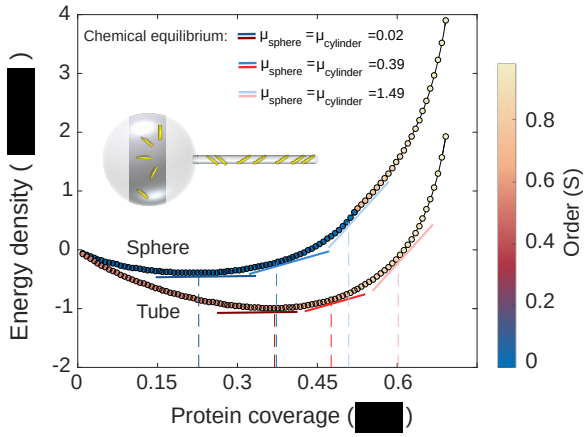

Figure 7.7: Energy landscape for a sphere with radius $R_s = 10/\bar{C}$ and a tube with radius $R_t = 2/\bar{C}$. Three different isotropic-nematic states of coexistence in an ensemble in which proteins can be exchanged with a bulk solution are highlighted by pairs of tangents with the same slope.

Since as discussed earlier the energy landscape on spheres is that of a planar surface with a tilt proportional to ϕ, the conditions for coexistence are similar. On tubes, however, there exists essentially no isotropic phase, and as illustrated in Fig. 7.7 the energy is convex in ϕ, leaving no room for coexistence. Yet, as suggested by experiments where thin tubes are pulled off giant vesicles and exposed to a solution with BAR proteins [20], it is

reasonable to expect isotropic-nematic coexistence in cylinder-sphere systems in equilibrium. Indeed, for moderate coverages, spheres adopt an isotropic state whereas thin-enough tubes are in a significantly nematic state. It is thus possible to find infinitely many equilibrium states of coexistence over a broad range of bulk chemical potentials, Fig. 7.7, in all of which area coverage and order are higher on the tube.

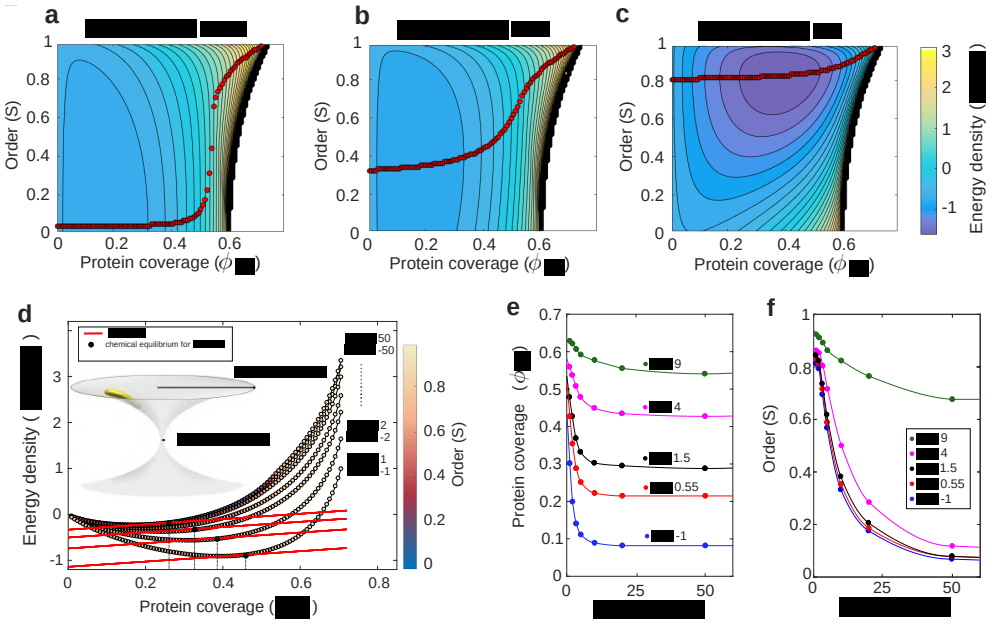

Figure 7.8: (a)-(c) Energy density contours as a function of density and order for surfaces of negative Gaussian curvature and zero mean curvature, with principal curvatures of magnitude $R = 1500, 150$ and 15 nm, with $\bar{C} = 15$ nm. Red dots denote stable states, which minimize the free energy for a given protein coverage (d) Free energy profiles for selected radii in a catenoid along the equilibrium paths, such that $\bar{C}R_1 = -\bar{C}R_2 = 1, 2, 3.3, 5, 10, 20, 50$. The chemical potential of proteins is the slope of these curves. The black dots are the tangent points to the same chemical potential $\mu = 0.55\ k_BT/a_p$ and they are in chemical equilibrium. (e) Protein coverage in chemical equilibrium for selected radii in a catenoid, same of (d), exposed to diffent chemical potentials, $\mu a_p/(k_BT) = -1, 0.55, 1.5$ and 4.

We finally examine the arrangement of proteins at fixed chemical potential on a surface of non-uniform Gaussian curvature and zero mean curvature, a

catenoid. Fig. 7.8(d) graphically depicts a catenoid with curved proteins in the inside of the surface, which can model a membrane neck, and shows the energy profile, color coded with nematic order, at different locations on the catenoid with different curvature. The points in each curve with a common tangent (black dots) allow us to identify the equilibrium coverage and nematic order at each location on the catenoid at fixed chemical potential. As shown in Fig. 7.8(e)(f), the thinner neck exhibits an enrichment in coverage and increased nematic order, so that at the thinnest section of the neck protein coverage is close to saturation and alignment (along the symmetry axis of the catenoid) is above 0.8. We also note that the contrast between the neck region and the rest of the surface is larger when the fixed protein chemical potential is lower. Interestingly, the protein configurations at the neck predicted by our model significantly differ from those resulting from a phenomenological continuum model in [67]. We should also note that the prediction of the coverage and nematic fields presented here is purely local and does not penalize in any way gradients in these fields [1].

Chapter 8

Dynamic of BAR proteins and curved membranes

Due to the curved shape and membrane binding of Bin/Amphiphysin/Rvs (BAR) domains, proteins containing such domains have the interesting ability of reshaping membranes. Furthermore, as we discussed in Chapter 7, because of their elongated shape they can align along a preferred direction, adopting a nematic organization that impinges anisotropic curvature on the membrane. For instance, incubation of small vesicles with a high concentration of BAR proteins leads to tubules covered by a dense protein scaffold where the elongated molecules are nematically arranged [121, 122]. In a different system, GUVs with sufficiently high bound protein density rapidly expel thin protein-rich tubes in a tension dependent manner [123]. On thin membrane tubes pulled out of giant unilamellar vesicles (GUVs), BAR proteins can also change the radius of the tube and the force required to hold it [124]. Beyond these well-known cases, in many physiological situations BAR proteins interact with pre-existing curved membrane templates. Such templates can include for instance invaginations caused by nanoscale topographical features on the cell substrate [125], mechanical folds [126, 127], or endocytic structures

[128, 129]. Due to their affinity for curved membranes, BAR proteins are thus bound to reshape such templates in ways that could be important in processes ranging from endocytosis to the sensing of topographical or mechanical cues in the cell environment. However, the dynamics of membrane reshaping by BAR proteins, and how it depends on initial membrane shape, remains elusive.

To answer this question, we developed a theoretical and computational modeling, combined with a novel experimental system, to study the reshaping of cellular-like membrane structures of a broad range of shapes and sizes. The experimental study that we present in this thesis was performed by our collaborators at the Institute for Bioengineering of Catalonia (IBEC), more experimental details are provided in our recent work [1].

8.1 Experimental setup

Supported lipid bilayer

In our system, we create curved membrane features off a supported lipid bilayer by lateral mechanical compression. As previously shown in vitro [126] and in cells [127], once stretch is applied to membranes and subsequently released, excess membrane area is stored in protrusions of tubular or spherical shape. The size and shape of tubes or spherical caps depends on the relative magnitude of excess area and excess enclosed volume. Controlling stretch, but also osmolarity, it is thus possible to generate tubules, buds, or spherical caps. In contrast with tubes pulled out of GUVs, where a tip force and tension are required to stabilize their shape, in our system tubes are stabilized osmotically without a pulling force. These protrusions emerging from a flat supported lipid bilayer (SLB) can serve as model system for membrane templates such as endocytic buds, or topographically/mechanically induced structures (Fig.8.1a). Further experimental insight, such as the lipid membrane composition, the stretching device and more in general the experiment procedure, can be find in [1].

Proteins injection

We capture protein binding to these curved templates starting from the injection of fluorescently labelled amphiphysin in the bulk solution on top of the pSLB (patterned supported lipid bilayer) (Fig. 8.1a). The fluorescence signal from both the pSLB and amphiphysin (in different channels) was subsequently monitored as a function of time. Once injected, the protein bound to the tubes and buds (Fig. 8.1b,left), and after further adsorption from the bulk started to reshape them (Fig. 8.1b,right), into geometrically heterogeneous structures with coexistence of small spherical and tubular features .

To understand the physical mechanisms underlying our observations, we developed a theoretical framework considering the dynamics of lipid tubes and buds with low coverage (since protein is injected once structures are formed) and low curvature (since the structures are made markedly thinner by Amphiphysin) upon exposure to BAR proteins. Theoretically, various computational studies using coarse-grained simulations of elongated and curved objects moving on a deformable membrane have suggested the self-organization of regions with high anisotropic (cylindrical) curvature with high-protein coverage and strong nematic order [130, 60, 41]. None of these works, however, predicted or observed the tube-sphere complexes that appear in our experiments (Fig.8.1b). Neither theoretical continuum models for the free-energy of curved and elongated molecules on membranes cannot predict whether the system is in an isotropic or nematic phase, nor the nematic direction, and instead nematic order and direction are fixed [64, 65].

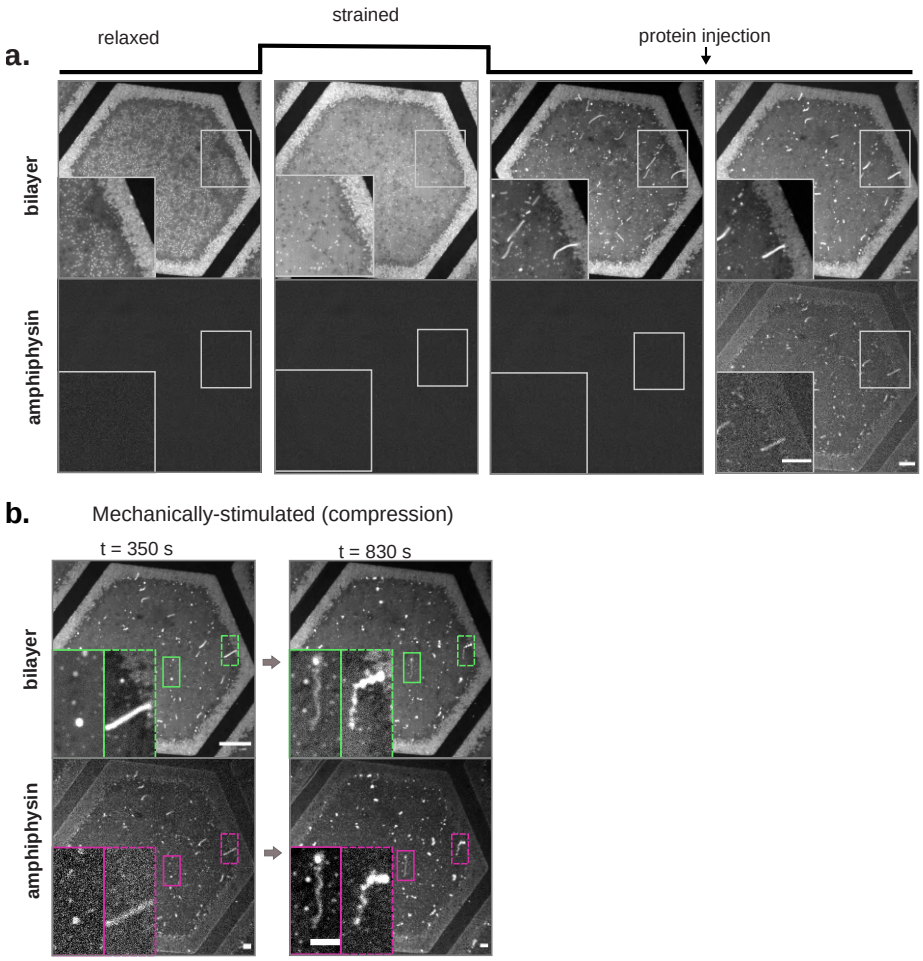

Figure 8.1: **a**, Representative images of the mechanical stimulation of the pSLB, showing both lipid and protein fluorescence images. In the resting initial state, excess liposomes stand on top of the pSLB. With strain, the liposomes incorporate in the pSLB. Upon release, excess lipids are expelled in the form or tubes or buds. At this stage, fluorescent Amphiphysin is gently microinjected on top of pSLB and its binding to the tubes and buds is monitored with time. **b**, Membrane tubes (green inset) and buds (purple inset) before (left) and after (right) being reshaped by Amphiphysin. Scale bar, 5 μm.

Chapter 9

Modeling the dynamical interplay between deformable membranes and elongated and curved proteins

In this Chapter we present a continuum model that captures the dynamics rising from the interplay between BAR proteins and mechanically-bent lipid membranes. Here, we employ the same continuum framework used in Chapter 2 for dissipative systems, based on the Onsager's principle. In addition to protein diffusion and membrane elasticity and hydrodynamics, we account for sorption dynamics of proteins [69] and their orientational order [131].

With this extended theory, we can predict the coupled dynamics of protein area fraction ϕ, the shape of the membrane surface Γ parametrized by $\boldsymbol{x}(u, v, t)$, and nematic order. Orientational order is quantified by the traceless

and symmetric tensor

$$\boldsymbol{Q} = S\left(\boldsymbol{\lambda}\otimes\boldsymbol{\lambda} - \frac{1}{2}\boldsymbol{I}\right), \tag{9.1}$$

capturing two important pieces of information: the order parameter S taking values between 0 and 1, where 0 corresponds to an isotropic organization of proteins and 1 to the maximum degree of order, and the net protein orientation given by the unit vector $\boldsymbol{\lambda}$. $\boldsymbol{I}$ is the identity tensor on the surface. In the following, we denote by $\boldsymbol{k}$ the second fundamental form or curvature of the surface.

To model the free energy of an ensemble of elongated and curved proteins on a curved membrane, our aim is to use the microscopically derived theory of Chapter 7. However, the evaluation of this theory requires the solution of a nonlinear system of equations, which is not practical in numerical simulations. For this reason we develop later an explicit parametrization of the theory of Chapter 7.

9.1 Modeling the state prior to protein exposure

Prior to protein exposure, we model the formation of membrane protrusions following the conceptual and computational approach in [126] under the assumption of axisymmetry. We consider an inextensible membrane patch Γ of radius 1 μm interacting with a support through an interaction energy density per unit surface area $U(z)$, where z is the separation between the membrane and the substrate. The free energy of the membrane is

$$\mathcal{F}_{\mathrm{m}}[\boldsymbol{x}] = \int_\Gamma \frac{k_0}{2}H^2\,dS + \int_\Gamma U(z)\,dS, \tag{9.2}$$

where k_0 is the bending stiffness of the membrane and $H = (\mathrm{tr}\ \boldsymbol{k})/2$ is the mean curvature and dS is the area element of Γ. To model the dynamics and as described elsewhere [83, 115, 75], we introduce a dissipation potential accounting for membrane viscosity $D_{\mathrm{m}}[\boldsymbol{v}]$, and obtain the governing equations

of the system by minimizing the Rayleighian functional

$$\frac{d}{dt}\mathcal{F}_{\mathrm{m}}[\boldsymbol{v}] + D_{\mathrm{m}}[\boldsymbol{v}] + \int_{\Gamma} \sigma \,\mathrm{tr}\, \boldsymbol{d}\, dS + p \int_{\Gamma} \boldsymbol{v}\cdot\boldsymbol{n}\, dS \tag{9.3}$$

with respect to the membrane velocity $\boldsymbol{v}$, where $\boldsymbol{d}$ is the rate-of-deformation tensor of the membrane, $\boldsymbol{n}$ is the outer normal to the surface, and the surface tension σ and pressure p are Lagrange multipliers that enforce the local inextensibility of the membrane and global incompressibility of the fluid enclosed between the membrane and the substrate.

Excess membrane resulting from lateral compression and excess enclosed volume resulting from osmotic imbalances lead to a variety of equilibrium membrane protrusions, which include long tubules, spherical buds and shallow spherical caps as mapped in [126]. All of these protrusions are observed in our experimental system. To study the effect of proteins on each of these types of structures, we prepared protrusions in equilibrium by laterally compressing the flat membrane and increasing the enclosed volume to V with respect to V_0 (the reference volume computed for a planar membrane at the equilibrium separation z_0). Upon compression, the membrane delaminates to form a shallow spherical cap. By further increasing lateral compression and/or the enclosed volume, we obtained equilibrium structures consisting of spherical buds connected to the supported part of the bilayer by a narrow neck, or long tubular protrusions, see Fig. 9.1-a.

9.2 Modeling the protein-membrane interaction dynamics

Proteins on the membrane are represented by two fields, their area fraction ϕ and their nematic tensor $\boldsymbol{Q}$, which in our axisymmetric setting can be represented by the order parameter S and the angle θ with respect to the azimuthal direction $\boldsymbol{e}_1$, see Fig. 9.1b.

Given the free-energy of the elongated and curved proteins on the membrane $\mathcal{F}_{\mathrm{p}}[\boldsymbol{x}, \phi, S, \theta]$, to be specified later and which depends on $\boldsymbol{x}$ through the

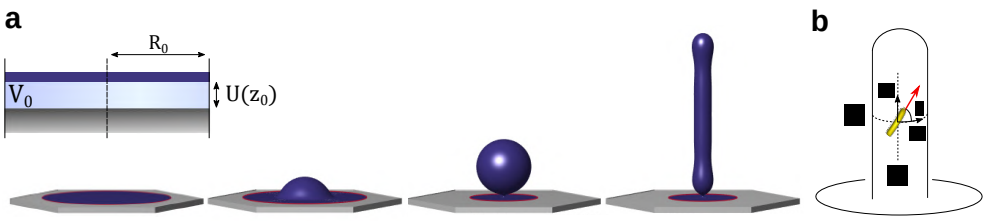

Figure 9.1: (a) Illustration of the initial state of the system, in which the planar adhered membrane sits on a substrate at the equilibrium separation z_0 (left) and upon compression and excess enclosed volume, develops a variety of protrusions as described in the text. (b) In our axisymmetric model, the principal directions of curvature coincide with the symmetry directions $\boldsymbol{e}_1$ and $\boldsymbol{e}_2$. The angle θ characterizes the orientation of an elongated molecule or of the nematic direction on the membrane.

curvature of the membrane, we can define the total free energy of the system as

$$\mathcal{F}[\boldsymbol{x},\phi,S,\theta] = \mathcal{F}_{\mathrm{m}}[\boldsymbol{x}] + \mathcal{F}_{\mathrm{p}}[\boldsymbol{x},\phi,S,\theta] + \int_\Gamma \frac{\Lambda_\phi}{2}|\nabla\phi|^2\,dS + \int_\Gamma \frac{\Lambda_S}{2}|\nabla S|^2\,dS \quad (9.4)$$

$$+ \int_\Gamma \frac{\Lambda_\theta}{2}|\nabla\theta|^2\,dS, \quad (9.5)$$

where the last three terms regularize the phase boundaries between regions of different protein coverage, order and orientation.

We can write the Rayleighian functional of the membrane-protein system as

$$\frac{d}{dt}\mathcal{F}[\boldsymbol{v},\boldsymbol{w},\dot{S},\dot{\theta}] + D_{\mathrm{m}}[\boldsymbol{v}] + D_{\mathrm{p}}[\boldsymbol{w},\dot{S},\dot{\theta}] + \int_\Gamma \sigma\,\mathrm{tr}\;\boldsymbol{d}\,dS + p\int_\Gamma \boldsymbol{v}\cdot\boldsymbol{n}\,dS, \quad (9.6)$$

where $\boldsymbol{w}$ is the net diffusive velocity of proteins relative to the lipids and $D_{\mathrm{p}}[\boldsymbol{w},\dot{S},\dot{\theta}]$ is the dissipation potential of proteins accounting for translational, order and rotational drag. Minimization of the Rayleighian with respect to $\boldsymbol{v}$ leads to the equations of mechanical equilibrium govering shape dynamics. Minimization with respect to $\boldsymbol{w}$ leads to a generalized Fick's law relating $\boldsymbol{w}$ to the gradient of the chemical potential of the proteins, whereas minimization with respect to $\dot{S}$ and $\dot{\theta}$ leads to configurational balance equations. Here, we

assume that S and θ relax much faster than $\boldsymbol{x}$ and ϕ. Combining Fick's law with the equation of balance of mass for proteins

$$\frac{\partial \phi}{\partial t} + \phi \operatorname{tr} \boldsymbol{d} + \nabla \cdot (\phi \boldsymbol{w}) = r, \tag{9.7}$$

where r is the sorption rate, we obtain a nonlinear diffusion-reaction equation for the protein density. All these equations are self-consistently coupled in this formalism. We refer to the first Part of the thesis for a full account of this formulation and of its computational axisymmetric implementation using a Galerkin finite element method based on B-Spline approximations.

We model sorption with a modified Langmuir model given by[69]

$$r = k_A c_{\text{bulk}} (\phi_{\max} - \phi) e^{-\beta \mu_{\text{mech}}} - k_D \phi, \tag{9.8}$$

where k_A is an adsorption rate constant, c_{bulk} the bulk concentration of proteins, μ_{mech} is the mechanical part (associated with their bending elasticity) of the chemical potential of proteins on the membrane, $1/\beta$ is the thermal energy, and k_D is a desorption rate constant. The exponential part of the adsorption term models an adsorption mechanism by which a curved molecule in solution must conform to the membrane curvature by a thermal fluctuation to become a membrane-bound protein, analogously to the case of binding of flexible adhesion molecules [132]. This has kinetic and thermodynamic consequences, as adsorption becomes faster and equilibrium coverage higher when the membrane curvature is close to the spontaneous curvature of the protein.

9.3 Free-energy of the elongated and curved proteins on a membrane

Summary of the mean-field density functional theory

Following the mean field approach presented in Chapter 6 and 7, we can write the free-energy of the ensemble of elongated molecules in terms of the position-dependent number density of proteins ψ, related to the area fraction

by $\phi = a_p\psi$ where a_p is the area of a protein, and the angular distribution f of proteins as

$$\begin{aligned}\mathcal{F}_{\mathrm{p}}[\boldsymbol{x},\psi,f] =& \frac{1}{\beta}\int_\Gamma \psi\ln\psi\,dS + \frac{1}{\beta}\int_\Gamma \psi\left\{\int_{\mathbb{S}} f\left[\ln f - \ln g\right]\,d\gamma\right\}\,dS \\ &+ \int_\Gamma \psi\int_{\mathbb{S}} fU^b\,d\gamma\,dS,\end{aligned} \tag{9.9}$$

where $1/\beta = k_BT$ is the thermal energy and the set $\mathbb{S} = [-\pi,\pi)$ represents all possible orientations of molecules. The first term models the positional entropy of proteins, the second term accounts for orientational entropy and the excluded area though the function $g(\psi,\gamma) = 1 - \psi[c - dSP_2(\cos\gamma)]$ (with c and d parameters that depend on the geometry of the particles and $P_2(x) = x^2 - 1/2$), and the last term models the bending elasticity of proteins. The function $U^b(\boldsymbol{k},\gamma)$ is the bending energy of an adsorbed protein oriented along the tangential vector $\boldsymbol{\ell}$ forming an angle γ with a fixed direction and is given by

$$U^b(\boldsymbol{k},\gamma) = \frac{\kappa_p a_p}{2}(k_{\boldsymbol{\ell}} - \bar{C})^2, \tag{9.10}$$

where κ_p is its bending rigidity (with units of energy), $\bar{C}$ is its preferred curvature along the long axis, and $k_{\boldsymbol{\ell}} = \boldsymbol{\ell}\cdot\boldsymbol{k}\cdot\boldsymbol{\ell}$ is the normal curvature of the surface along the long direction of the protein. Equation (9.9) allows us to identify the mechanical part of the chemical potential of proteins as

$$\mu_{\mathrm{mech}} = \int_{\mathbb{S}} fU^b\,d\gamma. \tag{9.11}$$

Minimization of $\mathcal{F}_{\mathrm{p}}$ with respect to the angular distribution f yields an effective free energy depending only on the nematic tensor

$$\boldsymbol{Q} = \int_{\mathbb{S}} f(\gamma)\,\boldsymbol{\ell}(\gamma)\otimes\boldsymbol{\ell}(\gamma)\,d\gamma - \frac{1}{2}\boldsymbol{I}. \tag{9.12}$$

Since $\boldsymbol{Q}$ is traceless and symmetric, it can be expressed as in Eq. (9.1). In the axisymmetric setting considered here, $\boldsymbol{Q}$ can be parametrized by S and the angle θ between the nematic direction $\boldsymbol{\lambda}$ and the azimuthal direction. Denoting by k_1 and k_2 the principal curvatures of the surface at any point (which in

the axisymmetric setting considered here are along symmetry directions), we can express the free energy of the proteins as

$$\mathcal{F}_{\mathrm{p}}[\boldsymbol{x}, \psi, S, \theta] = \int_{\Gamma} F_{\mathrm{p}}(\psi, S, \theta, k_1, k_2)\, dS, \tag{9.13}$$

where the evaluation of $F_{\mathrm{p}}(\psi, S, \theta, k_1, k_2)$ involves the solution of a nonlinear system of algebraic equations with two unknowns, see [131]. Importantly, the only material parameters in this theory are the long and short axes of the ellipse modeling a protein, its preferred curvature $\bar{C}$ and its bending stiffness $\kappa_p a_p$, for which estimates are available.

To summarize, this theory allows us to evaluate the free energy of proteins and study the isotropic-to-nematic transition on membranes adopting simple geometric motifs observed in our experiments, such as spheres and cylinders of various radii. On spheres, the free energy above is independent of θ whereas on cylinders it is minimized for $\theta = 0$ (proteins aligned with the direction of curvature) as long as the cylinder radius is larger than $1/\bar{C}$. Minimization with respect to θ allows us to compute the free-energy profile as a function of area coverage ϕ and order S alone, see Fig. 9.2 and Fig. 9.3. These figures shows that the free-energy landscape exhibits an order- and coverage-dependent forbidden region due to crowding effects. It also shows that, for a planar and a spherical configuration, the model predicts a sharp and discontinuous isotropic-nematic phase transition with a range of intermediate protein coverages exhibiting coexistence of the two phases. The landscape on cylindrical surfaces is different in several ways. There, the isotropic-to-nematic transition is continuous and the isotropic phase is ordered even at low ϕ, particularly for thin tubes, due to the bias introduced by anisotropic curvature.

Explicit parametrization of the theory

The mean field theory that we have just recapitulated connects the microscopic statistical physics with continuum physics and predicts the density- and curvature-dependent isotropic-to-nematic transition of proteins, but is

cumbersome to evaluate and integrate in the computational framework described in Section 9.2 and in [115]. For this reason, we fit the free energy of proteins given by the mean field theory, $\mathcal{F}_{\mathrm{p}}$, to an explicit functional form that we denote as $\hat{\mathcal{F}}_{\mathrm{p}}$. Replacing $\mathcal{F}_{\mathrm{p}}$ by $\hat{\mathcal{F}}_{\mathrm{p}}$ is done for purely practical reasons. To identify an ansatz for the functional form of $\hat{\mathcal{F}}_{\mathrm{p}}$, we examine Eq. (9.9).

Focusing first on the first two integrals in this equation, which do not depend explicitly on θ, and noting that $\langle P_2(\cos\gamma)\rangle = S/2$ where $\langle\ \rangle$ denotes the average with respect to f[131], we postulate the entropic part of the ansantz as

$$\begin{aligned}\hat{\mathcal{F}}_{\mathrm{p,entropy}}[\boldsymbol{x},\phi,S] =& \frac{A_1}{\beta a_p}\int_\Gamma \left\{\phi\ln\phi - \phi\ln\left[1-\phi\left(c-\frac{S^2}{2}d\right)\right]\right\} dS + \\ & \frac{A_2}{\beta a_p}\int_\Gamma \phi S^2 dS - \frac{A_3}{\beta a_p}\int_\Gamma \phi\ln(1-S)dS,\end{aligned} \tag{9.14}$$

where A_1, A_2 and A_3 are non-dimensional fitting coefficients. The first integral accounts for positional entropy and excluded area, the second integral is a quadratic approximation to the order entropy, and the last integral allows us to fit the fast increase in the free-energy landscape for large ϕ and S, Fig. 9.2a1,b1.

Focusing now on the last term of Eq. (9.9), to propose an explicit functional form for the curvature energy of proteins, we note that

$$\begin{aligned}\int_{\mathbb{S}} f(\gamma)U^b\, d\gamma &= \frac{\kappa_p a_p}{2}\int_{\mathbb{S}} f(\gamma)\left(\boldsymbol{k}:\boldsymbol{\ell}\otimes\boldsymbol{\ell}-\bar{C}\right)^2 d\gamma \\ &= \frac{\kappa_p a_p}{2}\int_{\mathbb{S}} f(\gamma)\left(\boldsymbol{k}\otimes\boldsymbol{k}::\boldsymbol{\ell}\otimes\boldsymbol{\ell}\otimes\boldsymbol{\ell}\otimes\boldsymbol{\ell}-2\bar{C}\boldsymbol{k}:\boldsymbol{\ell}\otimes\boldsymbol{\ell}+\bar{C}^2\right) d\gamma \\ &= \frac{\kappa_p a_p}{2}\left[\boldsymbol{k}\otimes\boldsymbol{k}::\langle\boldsymbol{\ell}\otimes\boldsymbol{\ell}\otimes\boldsymbol{\ell}\otimes\boldsymbol{\ell}\rangle-2\bar{C}\boldsymbol{k}:\langle\boldsymbol{\ell}\otimes\boldsymbol{\ell}\rangle+\bar{C}^2\right].\end{aligned} \tag{9.15}$$

where : denotes the double contraction of second-order tensors, :: the contraction of fourth-order tensors, and $\langle\ \rangle$ the average with respect to f. We note that $\boldsymbol{A} = \langle\boldsymbol{\ell}\otimes\boldsymbol{\ell}\rangle = \boldsymbol{Q} + \frac{1}{2}\boldsymbol{I}$. Invoking the Doi closure [133] according to which $\langle\boldsymbol{\ell}\otimes\boldsymbol{\ell}\otimes\boldsymbol{\ell}\otimes\boldsymbol{\ell}\rangle :: \boldsymbol{C} \approx \langle\boldsymbol{\ell}\otimes\boldsymbol{\ell}\rangle\otimes\langle\boldsymbol{\ell}\otimes\boldsymbol{\ell}\rangle :: \boldsymbol{C}$ where $\boldsymbol{C}$ is a fourth-order tensor,

we can approximate the curvature part of the proteins free energy as

$$\begin{aligned}\int_\Gamma \psi \int_{\mathbb{S}} f U^b \, d\gamma \, dS &\approx \int_\Gamma \phi \frac{\kappa_p}{2} \left(\boldsymbol{k} : \boldsymbol{A} - \bar{C}\right)^2 dS = \int_\Gamma \phi \frac{\kappa_p}{2} \left(H + \boldsymbol{k} : \boldsymbol{Q} - \bar{C}\right)^2 dS \\ &= \int_\Gamma \phi \frac{\kappa_p}{2} \left[(1-S)H + S k_{\boldsymbol{\lambda}} - \bar{C}\right]^2 dS \\ &= \int_\Gamma \phi \frac{\kappa_p}{2} \left[H + S\frac{k_1 - k_2}{2}(2\cos^2\theta - 1) - \bar{C}\right]^2 dS,\end{aligned} \tag{9.16}$$

where $k_{\boldsymbol{\lambda}} = \boldsymbol{\lambda} \cdot \boldsymbol{k} \cdot \boldsymbol{\lambda}$ is the normal curvature along the nematic direction. We checked that this approximation to the curvature part of the free energy was insufficient to closely fit the free energy of cylinders (particularly the minimum energy paths and isotropic-to-nematic transition in Fig. 9.2a) and for this reason we consider an expanded ansantz for the curvature free energy of proteins of the form

$$\begin{aligned}\hat{\mathcal{F}}_{\mathrm{p,curv}}[\boldsymbol{x}, \phi, S] = &\int_\Gamma \phi \frac{\kappa_p}{2} \left[H + S\frac{k_1 - k_2}{2}(2\cos^2\theta - 1) - \bar{C}\right]^2 dS \\ &+ \int_\Gamma \phi \frac{\kappa_p}{2} S \sum_{i=0}^{3} \frac{B_i}{\bar{C}^{i-2}} \left(\frac{k_1 - k_2}{2}(2\cos^2\theta - 1) - \bar{C}\right)^i dS,\end{aligned} \tag{9.17}$$

where B_i are nondimensional fitting parameters. We note that the new term in the second line only adds a constant unless curvature is anisotropic. Combining Eqs. (9.14,9.17), we obtain an explicit form of the protein free-energy functional $\hat{\mathcal{F}}_{\mathrm{p}} = \hat{\mathcal{F}}_{\mathrm{p,entropy}} + \hat{\mathcal{F}}_{\mathrm{p,curv}}$ approximating the mean field functional $\mathcal{F}_{\mathrm{p}}$ and amenable to numerical calculations.

To fit the parameters A_i, we first focused on the purely entropic interaction of elliptical proteins on a flat membrane, which we evaluated with the mean field model in Eq. 9.9. We then fitted the functional proposed in Eq. 9.14 to the mean field landscape using a nonlinear least-squares method. In a second step, we included the bending energy in the mean field model, computed the free-energy landscape for flat, spherical and cylindrical configurations with different curvatures, see Fig. 9.2a, and used these free-energy landscapes to fit B_i using nonlinear leasts-squares.

See Fig. 9.3 for a comparison of the free-energy profiles obtained with both models. Although there are noticeable differences, these are small and the approximate functional $\hat{\mathcal{F}}_{\mathrm{p}}$ captures quantitatively the most salient features of the mean field model including the curvature-dependent isotropic-to-nematic transition.

We note that if the radius of curvature of a cylindrical membrane is larger than that of the protein $1/\bar{C}$, then the free energy is minimized for $\theta = 0$ [131]. Thus, although we fitted the mean fit model to include the smaller radii, in all our simulations radii of curvature were larger than $1/\bar{C}$, and thus the free-energy functional can be simplified by setting $2\cos^2\theta - 1 = 1$.

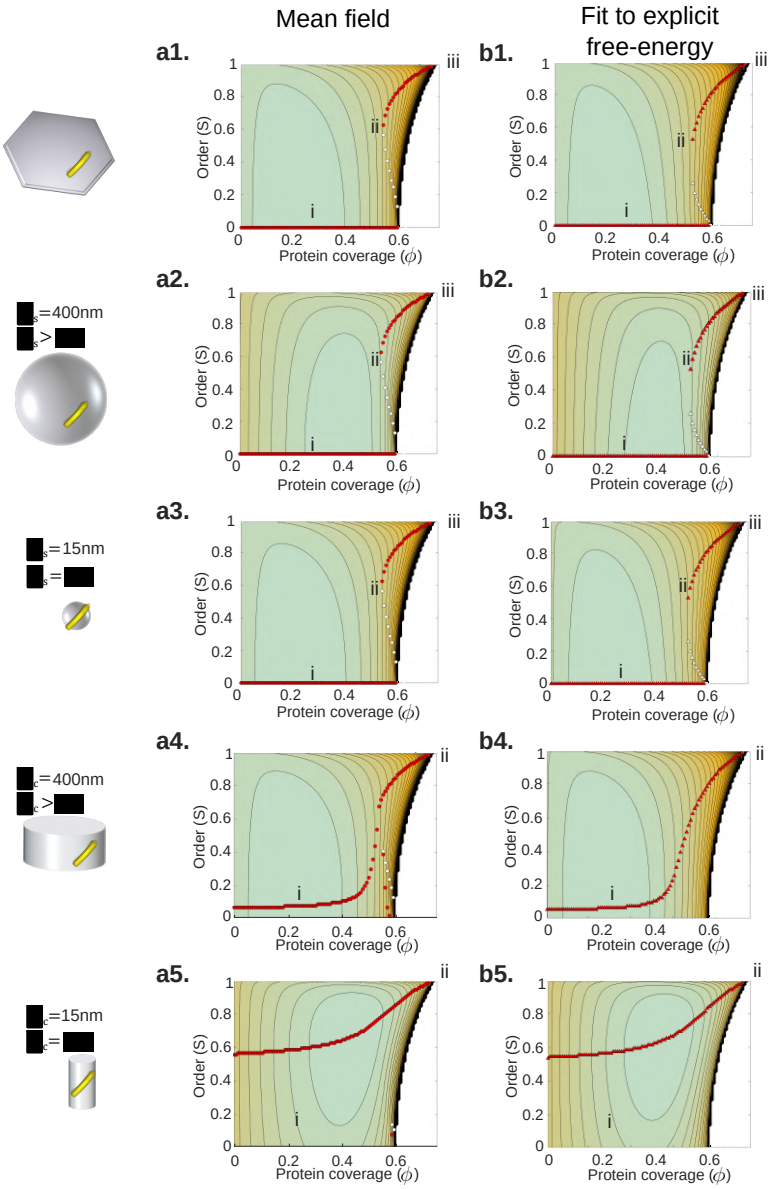

Figure 9.2: (a) Landscape of the free-energy density computed with the mean field model in Eq. (9.13) and described in detail in Chapter 6 and 7 for membranes of different curvature (flat, spherical and cylindrical with radii larger or equal to the intrinsic radius of a protein $1/\bar{C}$). (b) Analogous landscapes of free-energy density with the explicit model $\hat{\mathcal{F}}_{\rm p} = \hat{\mathcal{F}}_{\rm p,entropy} + \hat{\mathcal{F}}_{\rm p,curv}$ given by Eqs. (9.14,9.17) fitted to the mean field model. By minimizing the free-energy density with respect to S for a given protein coverage ϕ we find equilibrium paths $\phi(S)$. Stable branches are marked with red dots and unstable ones by white dots in (a) and (b).

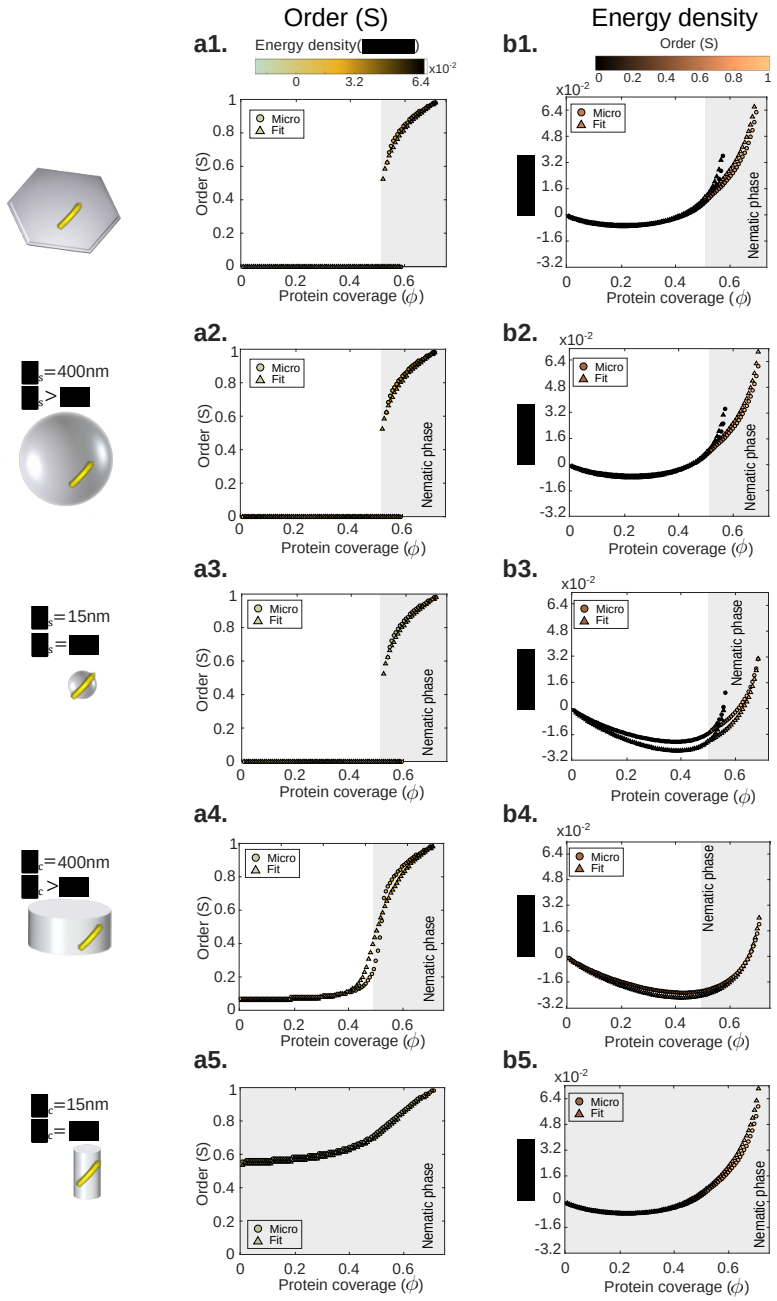

Figure 9.3: (a) Comparison of the stable branches in the $\phi - S$ plane with both models (color is energy density). (b) Comparison of the stable branches in the $\phi-$energy plane with both models (color is order).

Chapter 10

Results and discussion

10.1 Selection of parameters

Following [126], we assume a Morse potential for $U(z)$ with a membrane-support equilibrium distance of $z_0 = 4.4$ nm and adhesion energy $-U(z_0) \approx 1.5$ mJ/m^2. For the material properties of the lipid membrane, we consider $k_0 = 20\ k_BT$ for the bending stiffness and $\eta = 5 \cdot 10^{-9}$ Nsm^{-1} for the 2D viscosity. We consider N-BAR proteins to be elliptical with semi-axis lengths $a = 7.5$ nm and $b = 2.5$ nm, leading to the non-dimensional constants $c = 15.66$ and $d = 6$ appearing in the expression for the free-space as a function of density and order in Eq. (9.14). We assume that these proteins have an intrinsic curvature of $1/\bar{C} = 15$ nm, an area on the membrane of $a_p \approx 58$ nm^2, and a protein bending rigidity of $\phi_{max} k_p = 20\ k_BT$ at saturation ($\phi_{max} \approx 0.75$) based on a rigidity of the membrane-protein compound of 40 k_BT [134, 41, 130]. We consider a diffusion coefficient for proteins of $D_\mathrm{p} = 0.13$ μm^2/s. The fitting procedure of the functional given by Eqs. (9.14,9.17) results in $A_1 = 1.25$, $A_2 = 0.7$, $A_3 = 0.5$, $B_0 = 1.61$, $B_1 = -2.49$, $B_2 = 1.32$ and $B_3 = -0.43$. We consider an adsorption rate of $k_A = 1/30$ μM^{-1} s^{-1} and desorption rate to $k_D = 1/1800$ s^{-1}, in the order of that consider in previous works in a related system [124]. In the absence of measurements, we choose

$\Lambda_\phi/a_p = 10k_BT$ and $\Lambda_S/a_p = \Lambda_\theta/a_p = 1k_BT$ large enough so that, when phase separation occurs, domain boundaries have a finite thickness and simulations are devoid of numerical oscillations signal of ill-conditioning, and small enough so that the dynamics of the problem are not affect by these parameters.

10.2 Time-scales

Our chemo-mechanical model for protein-membrane interaction captures many different phenomena occurring at different time-scales. To interpret our simulations and understand the observed dynamics, we examine next the timescales of the major phenomena. We have already mentioned that we assume that orientational order relaxes very fast. We approximate the time required for membrane shape dynamics as $\tau_m \sim \bar{S}\eta/k_0$ where $\bar{S}$ is the typical surface area of a geometric feature [135], leading to the estimate $\tau_m \approx 0.01$ s. The timescale for protein diffusion is $\tau_p \sim \ell^2/D_\mathrm{p}$ where ℓ is either the radius of a spherical bud or the length of a tube where proteins diffuse. For the membrane protrusions studied here, we estimate τ_p to be a few seconds. The timescale for protein adsorption can be approximated as $\tau_A \approx 1/k_A c_\mathrm{bulk}$, which in our experimental conditions ranges between a few seconds to minutes depending on concentration. Thus, even if these estimates are crude, the system exhibits a significant scale separation, except at high protein concentrations where protein adsorption and diffusion may compete. In experiments there is another time-scale associated to bulk transport of proteins in the medium, not accounted for in the model.

10.3 Simulation protocol for protein-membrane interaction

To computationally examine the effect of BAR proteins on pre-existing membrane protrusions, we start from tubular or spherical protrusions in mechanical equilibrium as those in Fig. 9.1a and following the protocol described in Section 9.2. Then, we prescribe the protein concentration in the medium, c_bulk,

and computationally track the dynamics of the system as described in Section 9.3 with the explicit free energy of proteins described in Section 9.3. According to Eq. (9.8), protein adsorption is faster in highly curved regions of the membrane, such as necks of spherical buds. Furthermore, curvature gradients also generate gradients of chemical potential that drive protein diffusion on the membrane towards highly curved regions. As these regions, with possibly anisotropic curvature, become enriched, nematic order progressively develops, giving rise to the protein dynamics and reshaping described later.

In the actual system with many membrane protrusions interacting with proteins, the reshaping of one protrusion may result in lipid and enclosed water exchange with the rest of the system, in particular with the adhered part of the membrane surrounding it. Since in our computational model we study one protrusion in isolation, we need to specify a mechanical ensemble controlling lipid and enclosed volume exchange between a protrusion and the adhered membrane. In our simulations, we consider an inextensible and axisymmetric membrane patch. During dynamical simulations, we fix the volume enclosed between the membrane patch and the substrate to its initial value. At the boundary of the patch, we impose a constant membrane tension given by the membrane tension in the equilibrium state prior to protein exposure. Thus the edge of the patch can move to accommodate lipid exchange between the protrusion and the adhered part of the membrane. The protrusion can also exchange water with the adhered part of the system, either because the later is changing its size or because the membrane is changing its separation z with the substrate. We found that modifying the mechanical ensemble, e.g. fixing the projected area of the patch instead of tension or pressure difference instead of enclosed volume, had some effect on the dynamics but did not fundamentally modify the protein dynamics and reshaping mechanisms described here. With our ensemble, however, elongation of the neck of a bud did not lead to significant shrinkage of the spherical bud, as observed in many experimental instances, but rather to membrane exchange between the protrusion and the adhered part (Movie 10.1). We identified that this was due to the limited abil-

ity of the protrusion to expel enclosed volume underneath the adhered part in our simulations, and when this volume exchange was eased, for instance by considering a more compliant membrane-substrate interaction, we recovered the experimental phenomenology of bud consumption upon neck elongation (Movie 10.2).

10.4 Mean-filed theory supports coexistence of spheres and cylinders in dynamical structures.

On flat membranes and for elliptical particles of the size and aspect ratio of Amphiphysin, as already shown in Chapter 7, the theory predicts an entropically-controlled discontinuous isotropic-to-nematic transition during which the system abruptly changes from low to high order as protein coverage increases above $\phi \approx 0.5$, in agreement with previous results in 3D [2], Fig. 9.2a. On curved surfaces, our model also accounts for the elastic curvature energy of proteins, which depends on the curvature of the surface, and on their intrinsic curvature and orientation relative to the surface directions of principal curvatures (Fig.10.1a). We then examined the protein free-energy landscape on spherical surfaces, which according to the theory coincides with that of the flat membrane with a bias proportional to ϕ times the bending energy of proteins on the curved surface. Thus, the minimum energy paths as density increases (red dots in Fig.10.1b-e) and hence the abrupt isotropic-to-nematic transition persist regardless of sphere radius, Fig.10.1b, c, noting that on a complete sphere the nematic phase necessarily involves defects [37]. On cylindrical surfaces, however, curvature is anisotropic and the energy landscape is fundamentally modified according to our theory as proteins can lower their free energy by orienting along a direction of favorable curvature. The competition between protein bending and entropy results in a continuous isotropic-to-nematic transition (Fig.10.1d) and a significant degree of orientational order even at low coverage when the tube curvature is com-

parable to that of the protein (Fig.10.1e). The model thus predicts how the nematic ordering of the curved and elongated membrane depends on coverage, curvature, and curvature anisotropy.

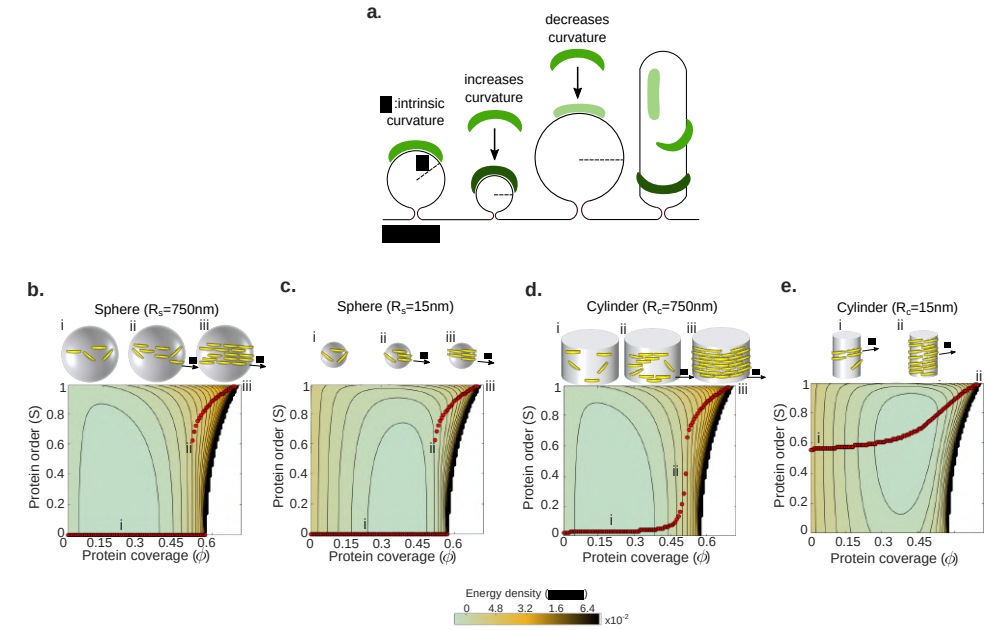

Figure 10.1: **a**, Schematic diagram of a BAR domain interacting with a lipid membrane. Protein elastic energy depends on surface curvature and protein orientation. For cylindrical surface, curvature is maximal (dark green) and minimal (light green) along perpendicular directions. **b-e**, Energy density landscape according to our mean field density functional theory depending on protein coverage ϕ, nematic alignment S, and the shape and size of the underlying membrane (sphere or cylinder as illustrated on top of each plot). Red dots denote states of equilibrium alignments S for a given protein coverage ϕ, i.e. minimizers of the free energy along vertical profiles, depicting the transition from isotropic (i) to nematic phase (ii-iii). The white region in the energy landscape is forbidden due to crowding. **b-c**, show discontinuous transitions for protein alignment on isotropically curved membranes. **d-e**, show continuous transitions for anisotropically curved membrane. The intrinsic protein radius of curvature is $1/\bar{C} = 15$ nm.

We then studied whether the model predicted the experimentally observed coexistence of thin tubes (which according to the theory should have higher

coverage and order) and larger spheres (which should have lower coverage and isotropic organization). We examined the energy landscape along the minimizing paths (red dots) for spheres and tubes of varying radius (Fig. 10.2). Since the slope of these curves is the chemical potential of proteins on the membrane, which tends to equilibrate with the fixed chemical potential of dissolved proteins in the medium, points of chemical coexistence are characterized by a common slope (red circles). This figure shows the largely non-unique combinations of geometry and membrane coverage compatible with coexistence in chemical equilibrium between higher-coverage nematic phases on cylinders and lower-coverage isotropic phases on spheres, supporting plausibility of such coexistence in the dynamical structures.

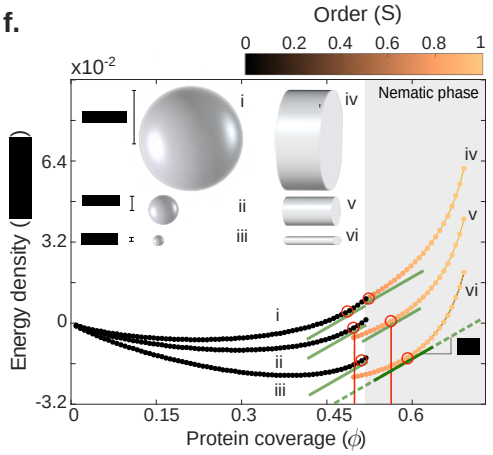

Figure 10.2: Free energy profiles for spheres and cylinders of different sizes along the equilibrium paths. The chemical potential of proteins is the slope of these curves. All points marked with red circles have the same chemical potential at the tangent points μ_b and hence are in chemical equilibrium.

10.5 Dynamics: simulations and experiments

Starting from membrane protrusions in mechanical equilibrium (tubular or spherical, Fig. 9.1a) off a supported bilayer in the absence of proteins and for

a fixed membrane tension and enclosed volume [126, 127], this model predicts the dynamics of membrane shape, ϕ, and S following a sudden increase of dissolved protein concentration in the medium (Fig. 10.3).

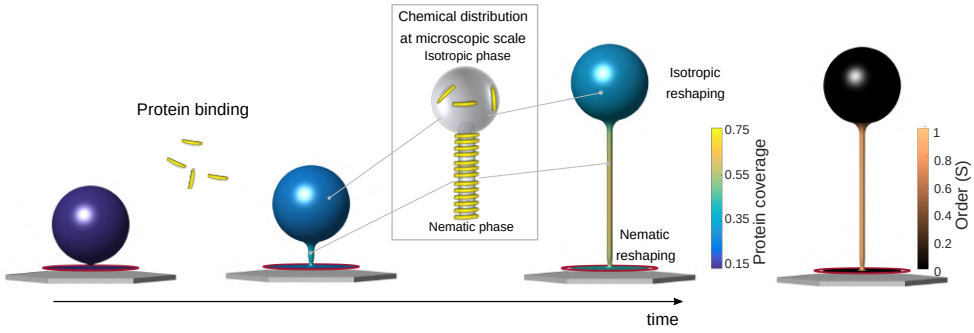

Figure 10.3: Schematic of reshaping dynamics involving membrane relaxation, and protein binding, diffusion and ordering.

Bud reshaping

First, we considered the dynamics of a spherical bud connected to the supported bilayer by a neck. As per the model, proteins should adsorb on the entire membrane but at a faster rate at the neck, where membrane curvature is more favourable than on the vesicles or on the flat part. Furthermore, due to a local gradient in chemical potential, proteins are further recruited by diffusion towards the neck, where they rapidly adopt a nematic order (Fig. 10.1e) in contrast with the isotropic order in the vesicle. The lower energy of proteins on the thin neck (Fig. 10.2) outweighs both the higher membrane curvature energy of a tube relative to a larger vesicle and the entropic penalty of a local protein enrichment. This leads to a progressive elongation of the neck into a thin tube with higher coverage and nematic order (Fig. 10.4a, and Movie 10.1). If the protrusion is allowed to exchange enclosed volume with the adhered part of the membrane, tube elongation occurs at the expense of the vesicle area (Fig. 10.4b and Movie 10.2). According to our simulations, the radius of these thin tubes is of about 15 nm, close to the radius of tubes

scaffolded by Amphiphysin (see Fig. 10.5a). Consistent with model predictions, the experimental observations systematically captured the growth of thin necks connecting shrinking vesicles to the supported bilayer (Fig. 10.4a, Fig. 10.5b,c and Movie 10.3). The contrast of nematic order between vesicles and tubes predicted by our simulations was not accessible experimentally. However, another hallmark of the isotropic-nematic coexistence suggested by the model is a protein enrichment on the tube relative to the vesicle. For a wide range of bud diameters and protein concentrations, our simulations predicted a stable and approximately two-fold higher protein concentration in tubular versus bud regions (Fig. 10.4c-right). When we estimated this experimentally, this enrichment was confirmed (Fig. 10.4c-left).

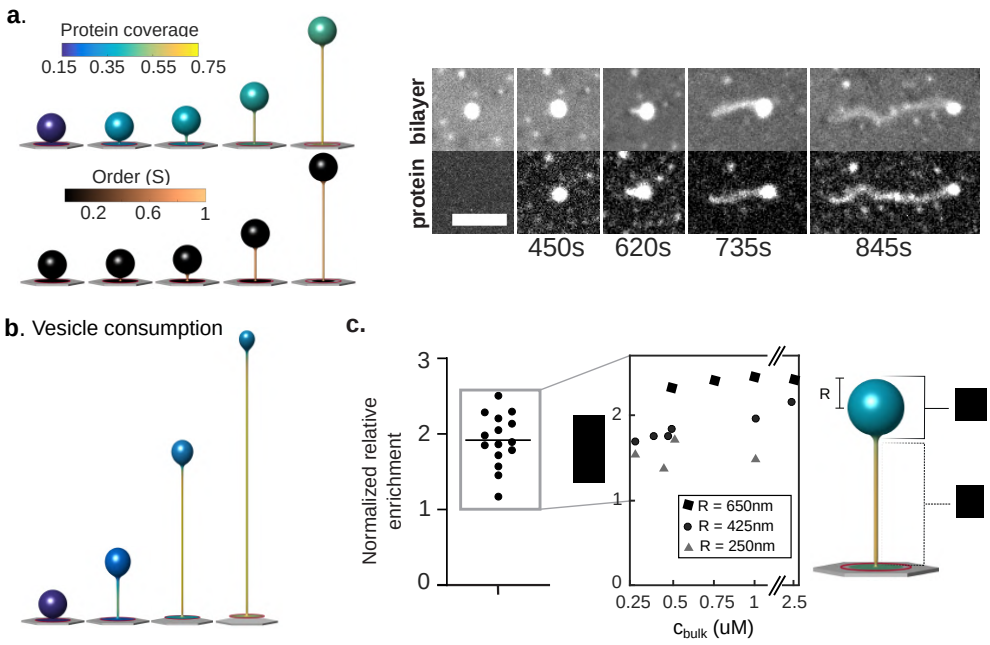

Figure 10.4: **a**, Results of simulations (left) and experiments (right) showing bud reshaping with time in response to Amphiphysin. **b**, Simulation of a bud of 850 nm diameter exposed to a concentration of 0.5 μM where exchange of the volume enclosed by the protrusion is eased by considering a softer substrate interaction. **b**, Ratios of protein coverage on tubes versus buds, normalised to the values measured for the lipid bilayer. Left, experimental values (n=15), right, computational estimation of relative protein enrichment between mean coverage on the tube ($\bar{\phi}_t$) and mean coverage on the vesicle ($\bar{\phi}_v$) for buds of different sizes exposed to different protein concentrations.

Experimentally, we found that a threshold bulk concentration was required for the growth of such tubes within the observed time frame (no growth observed at 0.05μM after 1100s, see Fig. 10.5c). We also found that the higher the concentration, the faster reshaping occurred. We thus systematically studied how increasing concentrations of protein in the bulk affected model outcome and reshaping over time. This led to a dynamical diagram of bud shape as a function of time and protein concentration (Fig. 10.6a). We note that we lacked a precise experimental control of the dynamics of protein delivery to the membrane due to diffusive and possibly advective transport from the in-

jection to the observation point, and hence a fully quantitative comparison between theory and experiment regarding the time-scales of reshaping was not possible. However, our simulations assuming instantaneous exposure of protein in solution also show a strong concentration dependence in the reshaping dynamics (Fig. 10.6a). Increasing protein concentration decreases the time required to initiate tubulation, representative of the time at which proteins nematically arrange (Fig. 10.5b). This was experimentally confirmed by measuring the times of tubulation initiation (Fig. 10.6b) and by looking at the protein binding curves on the buds. Such curves were obtained by plotting the mean intensity of the protein fluorescence on buds over time, until tubulation starts (See [1] for the protocol followed to estimate the protein coverage on the tubes or buds over time). The protein concentration triggering tubulation was reached faster at higher concentration (Fig. 10.6c and compare Movies 10.3 and 10.4, in which tube elongation starts much faster at 0.5μM bulk Amphiphysin concentration versus 0.25μM). Representative images of the reshaped state of buds at increasing times are plotted in Fig. 10.5c.

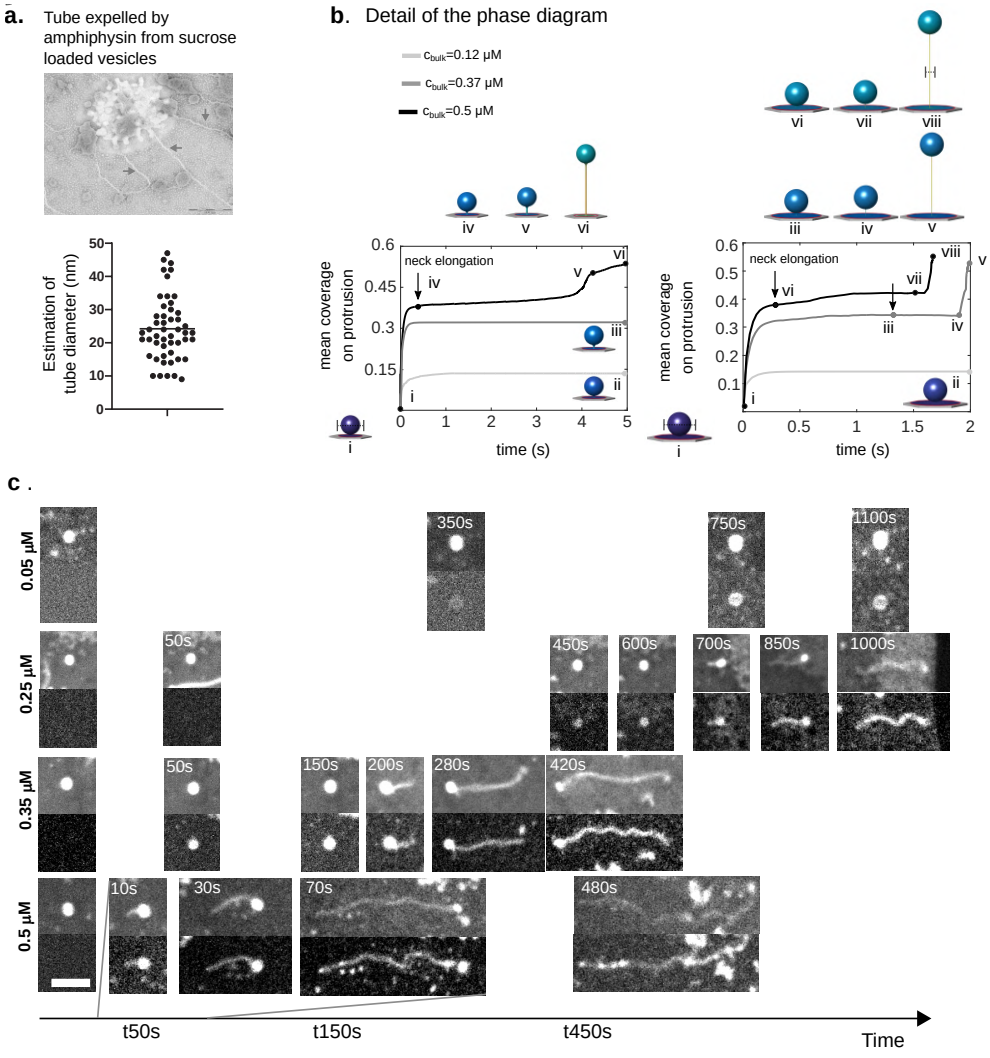

Figure 10.5: **a**, Estimation of the diameter of tubes reshaped by Amphiphysin using vesicles incubated with the protein and subsequently observed by transmission electron microscopy (TEM). **b**. Examples of the numerical simulations used to build the dynamical diagram where two buds of different initial radius are exposed to a set of protein bulk concentrations. Membrane tension is fixed to that prior to protein exposure and the volume enclosed between the membrane (protrusion and adhered part) and the substrate is fixed. Membrane reshaping is faster at higher concentration and a threshold protein coverage is required for neck elongation. **c**, Experimental examples of buds elongated from their neck, at different concentrations of Amphiphysin in the bulk. Buds are elongated faster at higher concentration. Scale bar, 5 μm.

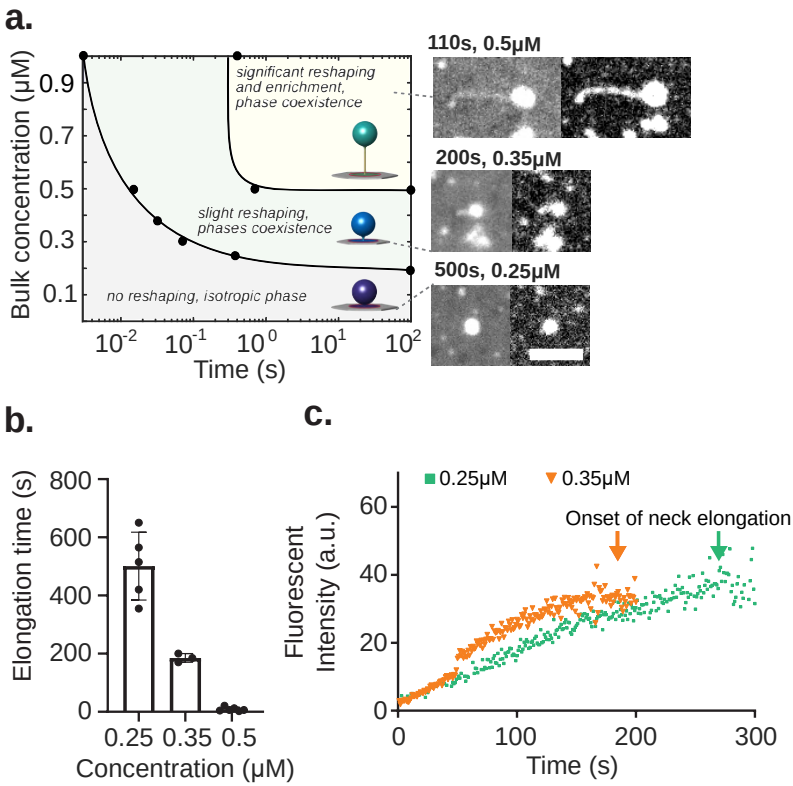

Figure 10.6: **a**, Dynamical diagram of bud reshaping as a function of time and bulk protein concentration, classifying the state of the system as one with no reshaping and isotropic protein organization ($S \approx 0$) , one with slight tube elongation, pearling, some degree of order ($S < 0.5$) and low coverage, and one with significant elongation, enrichment and phase coexistence. Inserts are experimental examples. **b**, Times at which bud elongation starts as a function of concentration (n=5,3 and 6 for 0.25, 0.35 and 0.5 μM respectively). **c**, Examples of Amphiphysin fluorescence intensities in buds incubated at two different concentrations. Bud elongation times are marked with an arrow.

Tube reshaping

Then, we considered the reshaping dynamics of tubes, which were frequently formed upon compression. For low protein concentration, proteins adsorbed onto the tubes and did not lead to an observable reshaping. Unlike the tubes that spontaneously relax into buds in absence of proteins (see Fig. 10.7), the

other exposed to 0.05μM bulk protein concentration maintain their morphology proving the stabilization role of BAR proteins.

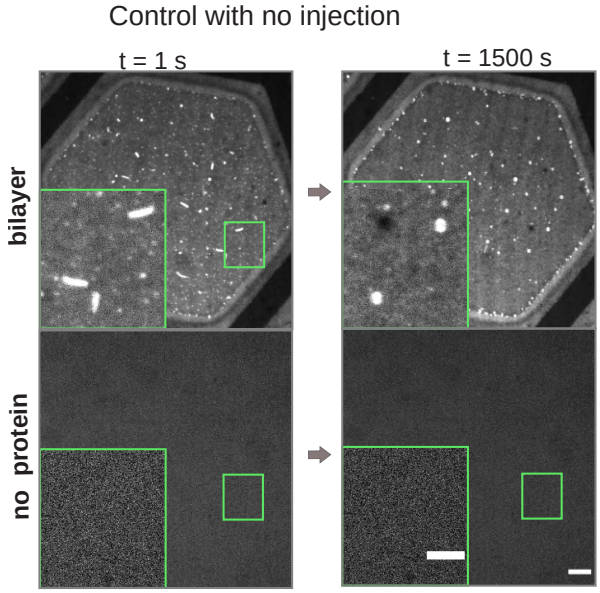

Figure 10.7: Control in which no protein is injected on top of the pSLB. Scale bar, 5 μm.

At higher concentrations, however, we systematically found that tube reshaping was initiated by the formation of a sequence of pearls (Fig. 10.8b and Movies 10.5 and 10.6). Previous results have shown the formation of pearled membrane tubes as a result of a sufficiently large isotropic and uniform spontaneous curvature [115, 136, 137]. Indeed, we hypothesized and our simulations show that, if initial tubes were large-enough, then at low coverage they should exhibit a largely uniform and isotropic arrangement of molecules (Fig. 10.8d, e), hence impinging an isotropic spontaneous curvature on the membrane leading to pearling (Fig. 10.8f; in the absence of a nematic transition, no further reshaping would follow this pearling phase). The pearling instability produces several membrane necks along the tube. If coverage is high enough, sufficiently many proteins may be drawn to those necks. This triggers an isotropic-to-nematic transition, a progressive elongation of thin

tubes, and a consumption of spheres analogous to that described above in membrane buds (Fig. 10.8b). Analogously to the case of bud elongation, we built a dynamical diagram of tube shape as a function of bulk protein concentration and time (Fig. 10.8c). Increasing concentration decreases the time to initiate pearling, which was also observed experimentally (Fig. 10.8d, e) and compare the earlier tube pearling observed in Movie 10.6, 0.25μM bulk Amphiphysin concentration, with Movie 10.7 at 0.35 μM.). Concentration also accelerates the subsequent transitions from uniform to pearled tubes, then to pearls connected by tubes (Fig. 10.8c, Fig. 10.9). This configuration was stable for long times in simulations and experiments (though such reshaped tubes collapsed on themselves, likely due to the related loss of tension [123, 138] this phase is best observed in the movie, see Movie 10.7).

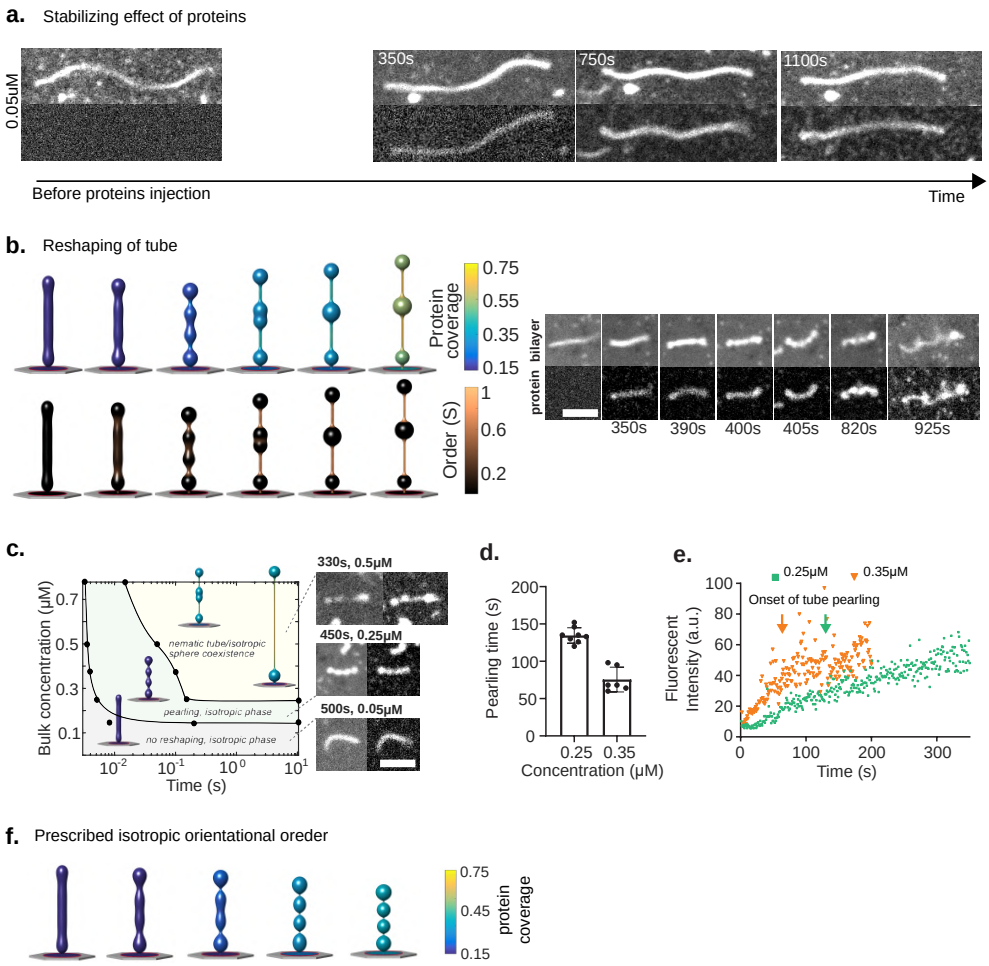

Figure 10.8: **a**, Experimental example of tube stabilization exposed to low concentration of Amphiphysin in the bulk. **b**, Results of simulations (left) and experiments (right) showing tube reshaping with time in response to Amphiphysin. **c**, Dynamical diagram of tube reshaping as a function of time and bulk protein concentration. **d**, Times at which tube pearling starts as a function of concentration (n=5 and 6 for 0.25 and 0.35 μM respectively). **e**, Examples of Amphiphysin fluorescence intensities in tubes incubated at two different concentrations. Tube pearling times are marked with an arrow. **f**, Membrane reshaping in the absence of a nematic transition (by prescribing isotropic orientational order, S=0); as predicted in the mean field theory, the saturation protein coverage is ≈ 0.55.

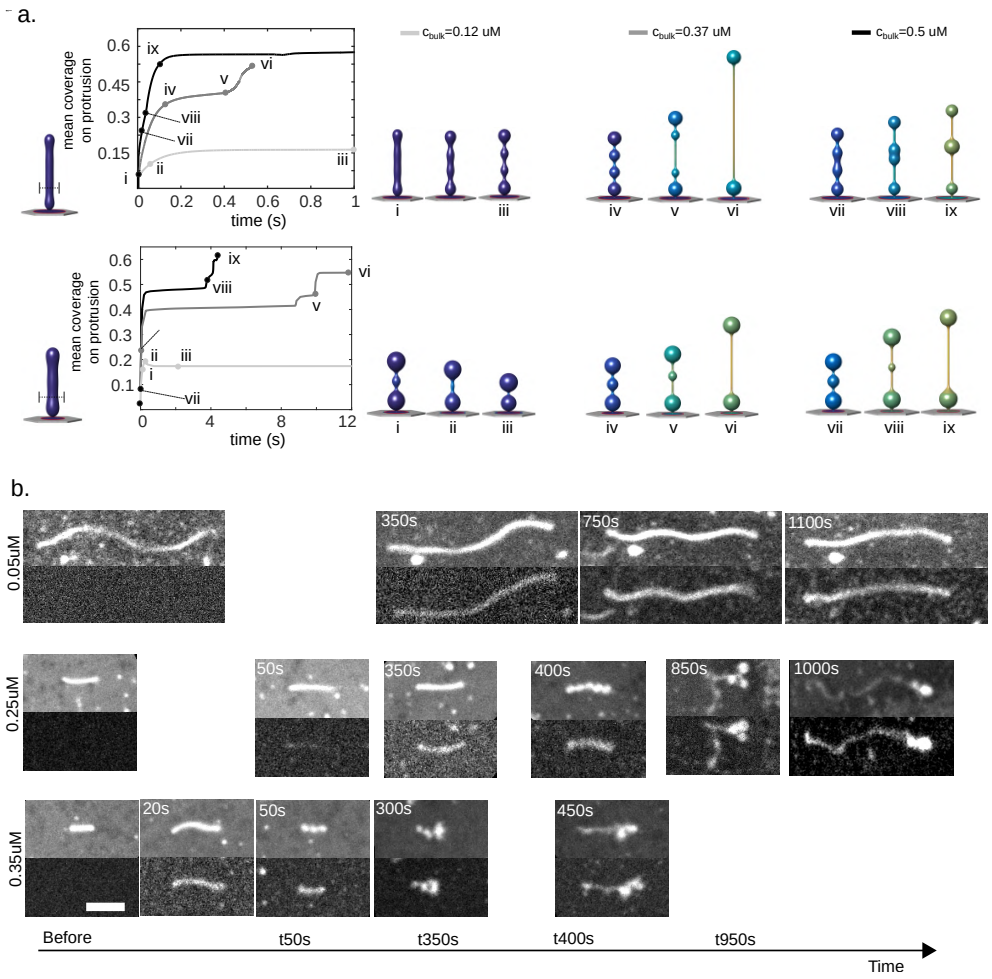

Figure 10.9: **a**, Examples of the numerical simulations used to build the dynamical diagram where two tubes of different initial radius are exposed to a set of protein bulk concentrations. Membrane reshaping is faster at higher concentration. While proteins bind, the tubes connecting the pearl are shrinking. **b**, Experimental examples of tubes reshaped at different concentrations of Amphiphysin in the bulk. Pearling and elongation occur faster at higher concentration. Scale bars, 5 μm.

For both tubes and buds, we evaluated the protein coverage required to trigger reshaping. Though measuring protein coverage in our experimental set up is very challenging, we developed a protocol to obtain an estimate. We

performed a classical calibration of the protein fluorescence versus coverage [139], and subsequently corrected the data by a geometrical factor taking into account the out-of-plane loss of signal and the geometrical signal integration of non-planar structures (Fig. 10.10a). As a result, initiation of bud elongation or tube pearling occurred at ≈ 0.4 and $\approx 0.25 - 0.35$ coverage respectively, approximately matching theoretical predictions (Fig. 10.10a, b).

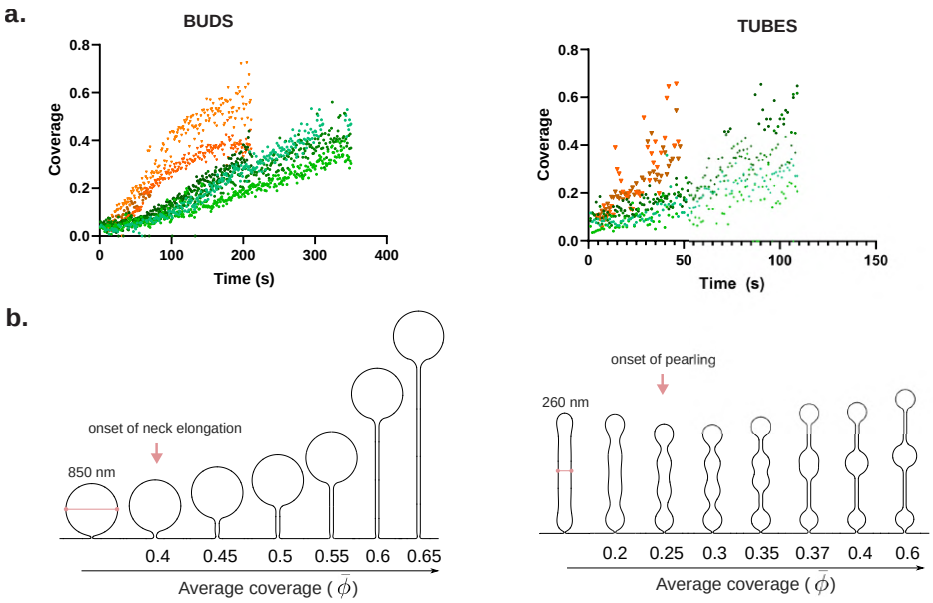

Figure 10.10: **a**, Binding curves of the protein binding to several buds (left) or tubes (right) at 0.25 μM (green colours) or 0.35 μM (orange colours) bulk protein concentration. We used the protocol described in [1] to plot the protein coverage on tubes or buds over time. Tube elongation from buds (left) starts when the plot ends, tube pearling (right) starts when the plot ends. **b**, Bud and tube reshaping upon protein adsorption and corresponding protein average coverage on the membrane protrusions.

Taken together, our results show that membrane curved templates exposed to sufficiently high concentrations of BAR proteins evolve towards uniformly thin and protein-rich nematic tubes. During the process, heterogeneous intermediates are formed, exhibiting mixtures of low curvature and low isotropic

coverage regions with others of high cylindrical curvature, high coverage, and nematic order.

Lysis of pressurized shallow caps

Finally, we evaluated the case of shallow spherical cap protrusions, which develop when hypo-osmotic shocks are generated both in vitro and in cells [126, 127]. In this case, the membrane needs to accommodate a significant excess volume of liquid with little excess membrane area, leading to a structure under significant tension [126]. Under these conditions of small excess area, shape changes are very difficult. Our model predicts that upon exposure of such shallow caps to BAR proteins, shape changes are negligible. Instead, tension in the membrane sharply increases, potentially leading to membrane tearing [140, 141] (Fig. 10.11). Accordingly (acknowledging as before that direct comparison of concentrations in experiments and simulations is not straightforward), shallow spherical caps formed by a hypo-osmotic shock in our experimental system were not visibly reshaped by Amphiphysin even at significant concentrations (Fig. 10.11), and teared and collapsed upon exposure to higher Amphiphysin concentrations (Fig. 10.11).

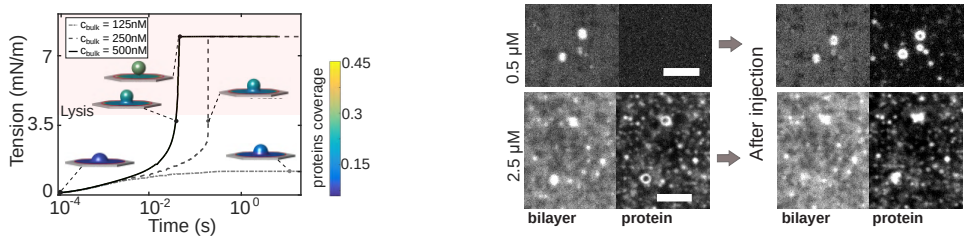

Figure 10.11: Left, Model prediction in pressurized caps of about 400 nm in radius exposed to different Amphiphysin concentrations. States in the pink shaded area are prone to membrane lysis. Right, Initial and final states of pressurized caps (obtained from an hypoosmotic shock) upon incubation with Amphiphysin. At 2.5 μM concentration, lysis of the caps can be observed. Scale bars, 5 μm.

Movie 10.1: Numerical simulation of the reshaping of a lipid bud of initial diameter 850 nm following protein binding from a protein bulk concentration of 0.5 μM. Color is protein coverage (left) and order (right). Membrane tension is fixed to that prior to protein exposure and the volume enclosed between the membrane and the substrate is fixed. `https://www.youtube.com/watch?v=B9spR9iexNg`

Movie 10.2: Numerical simulation of the reshaping of a lipid bud of initial diameter 850 nm following protein binding from a protein bulk concentration of 0.5 μM. Color is protein coverage (left) and order (right). Membrane tension is fixed to that prior to protein exposure and the exchange of the volume enclosed by the protrusion is eased by considering a softer substrate interaction.
`https://youtu.be/yVebSpxSwCg`

Movie 10.3: Time sequence of the reshaping of lipid tubes and buds formed through pSLB destretch, before and after incubation with 0.5 μM Amphiphysin. Fluorescence images show the membrane marker (left) and Amphiphysin marker (right). Insets show magnifications of the regions marked with squares.
`https://youtu.be/k7nSvMWipXA`

Movie 10.4: Time sequence of the reshaping of lipid tubes and buds formed through pSLB destretch, after incubation with 0.25 μM Amphiphysin. Fluorescence images show the membrane marker (left) and Amphiphysin marker (right). Insets show magnifications of the regions marked with squares.
`https://youtu.be/EBSX11XeLrc`

Movie 10.5: Numerical simulation of the reshaping of a lipid tube of initial diameter 260 nm following protein binding from a bulk concentration of 0.5 μM. Color is protein coverage (left) and order (right). `https://youtu.be/s_O_xMcXJbg`

Movie 10.6: Time sequence of the reshaping of lipid tubes and buds formed through pSLB destretch, before and after incubation with 0.25 μM amphiphysin. Fluorescence images show the membrane marker (left) and amphiphysin marker (right). Insets show magnifications of the regions marked with squares.
`https://youtu.be/pAQFvdqF5AI`

Movie 10.7: Time sequence of the reshaping of lipid tubes and buds formed through pSLB destretch, before and after incubation with 0.35 μM amphiphysin. Fluorescence images show the membrane marker (left) and amphiphysin marker (right). Insets show magnifications of the regions marked with squares.
`https://youtu.be/I0AL0H-8e2c`

Chapter 11

Summary and future work

In this second Part of the thesis we have presented an extensive study on elongated and curved proteins. Firstly, we have developed a mean field theory that captures the microscopic self-organization of elongated particles. Using this theory we have analysed the isotropic-to-nematic phase transition and how this self-organization depends on proteins coverage and on the curvature or anisotropy of the underlying membrane. The strong point of this theory is the connection from a micro- to a mesoscale to evaluate the free-energy landscape of proteins on selected surfaces. Later, to have a broader picture of the role of BAR proteins in many physiological situations, we have introduced a dynamical model, where the mean field theory is coupled with one of membrane dynamics. We have examined, both experimentally and through modelling, how BAR proteins dynamically interact with mechanically-induced membrane templates. We have captured protein binding to these curved templates starting from low protein coverage. We have demonstrated and characterised reshaping at low concentration, low curvature, and low tension, a highly relevant scenario in cells. As suggested by the mean field theory, the events can be generally understood by an isotropic-to-nematic phase transition, in which low curvature structures with isotropic protein orientation and

curvature progress towards highly curved lipid tubes with nematic protein arrangement, in a manner such that both phases coexist during the reshaping process.

More specifically:

- In Chapter 6 we have presented an adaptation to 2D of the work done by [2], where we focus on the orientational order of hard elliptical particles on planar surface. The free-energy landscape of the system is expressed in terms of the net orientation of proteins relative to the principal curvature directions θ, of the classical order parameter S, and of the number density f, and it depends on the aspect ratio of the proteins. We have shown that, on planar surfaces, the system exhibits a density-dependent discontinuous isotropic-to-nematic transition. We have also studied how the density-dependence transition changes when we consider particles of different aspect ratios.

- In Chapter 7 we have extended the mean-field density functional theory presented in Chapter 6 to study the ordering of elongated and curved proteins on differently curved fixed shapes. In this case, the free-energy landscape also depends on the intrinsic curvature of the proteins, on their bending rigidity, and on the second fundamental form of the membrane. In addition to the free-energy landscape, we have provided the orientational probability distribution of proteins. We have shown that, on spherical surfaces the system exhibits a density-dependent discontinuous isotropic-to nematic transition, as on planar membranes, while this transition is continuous on surfaces with anisotropic curvature such as cylinders or catenoids. We have shown that anisotropic curvature biases the system towards a slightly nematic state even at low protein concentrations. When the curvature of cylindrical membranes is higher than that of the proteins, then the orientational distribution becomes bimodal at low densities and asymmetric with respect to the principal direction of curvatures at high densities. Our theory has also allowed

us to examine the coexistence of isotropic and nematic phases under different conditions.

- We have used a novel experimental set up that tests the reshaping ability of BAR proteins depending on their orientational order. The experimental data used in this thesis have been provided and analysed by our collaborators at the Institute for Bioengineering of Catalonia (IBEC).

- In Chapter 9 we have proposed a continuum model for membranes and BAR protein dynamics. Here, in addition to protein diffusion and membrane elasticity and hydrodynamics (already presented in Chapter 2), we have accounted for protein sorption and orientational order. To capture the isotropic-to-nematic transition in the continuum framework we have started from the mean field theory presented in Chapters 6 and 7 and we have fitted an explicit functional form, that accurately reproduces the salient features of the microscopic problem, including the curvature-dependent isotropic-to-nematic transition.

- Through numerical simulations we have shown that the reshaping dynamics emerge naturally from the fundamental physics of membrane mechanics and its chemo-mechanical interaction with elongated and curved proteins, generating a non-trivial feedback between membrane stimulation and subsequent response. We have selected a series of numerical simulations and experimental data that characterize the reshaping process of BAR proteins on mechanically bent membranes, showing the interplay between membrane mechanical stimuli and BAR protein response. First, we have tested the sorption dynamics of BAR proteins on a variety of spherical buds of different sizes connected to the supported bilayer by a neck. The membrane curvature favores a faster binding of proteins on the neck where they nematically orient, in contrast with the isotropic organization of proteins on the vesicle. The inhomogeneous distribution and orientation of proteins along the membrane leads to a progressive elongation of the neck into a thin tube at the expense of the

vesicle area. Afterwards, we have characterized the reshaping dynamics of tubes that exhibit an initial sequence of pearls explained as an instability caused by the isotropic and uniform spontaneous curvature induced by the proteins. Pearling then evolves to a progressive elongation of the necks, that become tubes merging or consuming the initial pearls. For both the templates we have computed the protein coverage required to trigger the reshaping, which agree with the experimental data. Finally, we have considered the sorption on a shallow spherical cap protrusion and we have tracked how the membrane tension increases, eventually leading to membrane tearing.

Our formulation also sets the basis for future works:

- Several species:
  The theoretical framework used in this thesis could be easily extended for systems that account for several species. In the recent work [142], our theory has been used to describe the transport for procollagen export, that involve the diffusion and interaction of two membrane-bound species (COPII and TANGO1). Furthermore, our model could be extended to describe more complex systems that account for membrane reshaping due to the action of proteins coupled with cortex or cytoskeleton. This would lead to a broader understanding of the mechanics involved in the evolution of different organelles in cells.

- Three-dimensional description:
  Although many cellular structures adopt axisymmetric shapes, others do not. Our theoretical framework can successfully describe the membrane-protein interaction also in 3D, but the subsequent limitation to axisymmetry and the corresponding numerical approximation represent the main obstacles to study nonaxisymmetric shapes or ensembles of several domains. A fully 3D description would make it possible to study the case of multiple interacting caveolae or rosettes [5] and to address the open question related to the mechano-protection role of Caveolae in cells.

Appendix A

A.1 Stress Vectors

We identify the stress for the membrane-protein system considered here. We first note that, for a surface, stress can expressed in terms of stress vectors with tangential and normal components, $\boldsymbol{\sigma}^\alpha = \sigma^{\alpha\beta}\boldsymbol{g}_\beta + \sigma_n^\alpha \boldsymbol{n}$, performing power against $\boldsymbol{V}_{;\alpha}$ [88], which can be expressed as

$$\boldsymbol{V}_{;\alpha} = \left(v^\gamma \boldsymbol{g}_\gamma + v_n \boldsymbol{n}\right)_{;\alpha} = \left(v^\gamma{}_{;\alpha} - v_n k^\gamma{}_\alpha\right)\boldsymbol{g}_\gamma + \left(v^\gamma k_{\gamma\alpha} + v_{n,\alpha}\right)\boldsymbol{n}. \tag{A.1}$$

Here, $()_{;\alpha}$ denotes covariant differentiation and $()_{,\alpha}$ partial differentiation. Onsager's formalism naturally allows us to identify each contribution to the stress. For this, we write the Lagrangian in Eq. (2.19), ignoring external power input, enclosed volume constraints, freezing protein diffusive transport and assuming for simplicity a closed surface, since our interest here is in the stress, as

$$\delta\left(\dot{\mathcal{F}} + \mathcal{D} + \int_\Gamma \sigma \operatorname{tr} \boldsymbol{d}\, dS\right) = \int_\Gamma \left(\hat{\boldsymbol{\sigma}}^\alpha + \tilde{\boldsymbol{\sigma}}^\alpha + \bar{\boldsymbol{\sigma}}^\alpha\right)\cdot \delta\boldsymbol{V}_{;\alpha}\, dS = -\int_\Gamma \boldsymbol{\sigma}^\alpha_{;\alpha}\cdot\delta\boldsymbol{V}\, dS, \tag{A.2}$$

where $\hat{\boldsymbol{\sigma}}^\alpha$, $\tilde{\boldsymbol{\sigma}}^\alpha$, $\bar{\boldsymbol{\sigma}}^\alpha$ are the stress vectors associated to the free-energy, dissipation, and inextensibility constraint, and the total stress vector is the sum of these contributions. The expression in the right-hand side leads to the tangential and normal contributions of the stress in the mechanical Euler-Lagrange equation since

$$\boldsymbol{\sigma}^\alpha_{;\alpha} = \left(\sigma^{\alpha\beta}\boldsymbol{g}_\beta + \sigma_n^\alpha \boldsymbol{n}\right)_{;\alpha} = \left(\sigma^{\alpha\beta}{}_{;\alpha} - \sigma_n^\alpha k^\beta{}_\alpha\right)\boldsymbol{g}_\beta + \left(\sigma^{\alpha\beta}k_{\alpha\beta} + \sigma^\alpha_{n\,;\alpha}\right)\boldsymbol{n}. \tag{A.3}$$

We focus first on the free-energy part of the stress and use the fact that for a Lagrangian parametrization $\delta \boldsymbol{V}_{;\alpha} = \delta \dot{\boldsymbol{g}}_\alpha$. To identify the stress we assume that proteins do not diffuse, hence the energy only depends on the configuration of the membrane and invoking the chain rule we can write

$$\hat{\boldsymbol{\sigma}}^\alpha = \frac{\partial W}{\partial \boldsymbol{g}_\alpha} + \frac{W}{J}\frac{\partial J}{\partial \boldsymbol{g}_\alpha}. \tag{A.4}$$

Since protein transport is frozen for this calculation, W depends on $g_{\alpha\beta}$ and $k_{\alpha\beta}$ and we have [80, 143]

$$\frac{\partial W}{\partial \boldsymbol{g}_\alpha} = 2\left(\frac{\partial W}{\partial g_{\alpha\beta}}\right)\boldsymbol{g}_\beta + k^\beta_\mu \frac{\partial W}{\partial k_{\alpha\mu}}\boldsymbol{g}_\beta - \left(\frac{\partial W}{\partial k_{\alpha\beta}}\right)_{;\beta}\boldsymbol{n}. \tag{A.5}$$

Using Jacobi's relation, we further have

$$\frac{\partial J}{\partial \boldsymbol{g}_\alpha} = 2\left(\frac{\partial J}{\partial g_{\alpha\beta}}\right)\boldsymbol{g}_\beta = J g^{\alpha\beta}\boldsymbol{g}_\beta. \tag{A.6}$$

Substituting the above relation in last term of Eq. A.4, we obtain

$$\frac{W}{J}\frac{\partial J}{\partial \boldsymbol{g}_\alpha} = W g^{\alpha\beta}\boldsymbol{g}_\beta. \tag{A.7}$$

For the free energy density of the membrane considered here, $W(H, \phi, |\nabla\phi|^2)$, we have

$$\frac{\partial W}{\partial g_{\alpha\beta}} = D_1 W \frac{\partial H}{\partial g_{\alpha\beta}} + D_2 W \frac{\partial \phi}{\partial g_{\alpha\beta}} + D_3 W \frac{\partial |\nabla\phi|^2}{\partial g_{\alpha\beta}}. \tag{A.8}$$

Using $H = k_{\eta\gamma} g^{\eta\gamma}$ and the relation $\partial g^{\eta\gamma}/\partial g_{\alpha\beta} = -g^{\eta\alpha}g^{\gamma\beta}$, we obtain

$$\frac{\partial H}{\partial g_{\alpha\beta}} = -k^{\alpha\beta}. \tag{A.9}$$

Invoking balance of mass of proteins, $\delta\phi = -\phi\delta J/J$, we have

$$\frac{\partial \phi}{\partial g_{\alpha\beta}} = -\frac{\phi}{J}\frac{\partial J}{\partial g_{\alpha\beta}} = -\frac{\phi}{2}g^{\alpha\beta}. \tag{A.10}$$

The equation above can be further used to obtain

$$\frac{\partial |\nabla\phi|^2}{\partial g_{\alpha\beta}} = \frac{\partial(\phi_{,\eta}\phi_{,\gamma}g^{\eta\gamma})}{\partial g_{\alpha\beta}} = 2\frac{\partial \phi_{,\eta}}{\partial g_{\alpha\beta}}\phi_{,\gamma}g^{\eta\gamma} - \phi_{,\eta}\phi_{,\gamma}g^{\eta\alpha}g^{\gamma\beta}. \tag{A.11}$$

The first term in the right-hand side can be further simplified to $\phi\Delta\phi g^{\alpha\beta}$ by going back to the definition of stress in Eq. (A.2) and integrating by parts. The derivatives of energy density with respect to second fundamental form are given by

$$\frac{\partial W}{\partial k_{\alpha\beta}} = D_1 W \frac{\partial H}{\partial k_{\alpha\beta}}, \text{ where } \frac{\partial H}{\partial k_{\alpha\beta}} = g^{\alpha\beta}. \tag{A.12}$$

Substituting all the above relations into Eq. A.4, we obtain the free-energy contribution to the stress vectors as

$$\left\{-D_1 W k^{\alpha\beta} + (W - D_2 W\phi)g^{\alpha\beta} + 2D_3 W\left[\phi\Delta\phi g^{\alpha\beta} - \boldsymbol{g}^{\alpha}\cdot(\nabla\phi\otimes\nabla\phi)\cdot\boldsymbol{g}^{\beta}\right]\right\}\boldsymbol{g}_{\beta} - (D_1 W)_{,\beta} g^{\alpha\beta}\boldsymbol{n} = \hat{\boldsymbol{\sigma}}^{\alpha}. \tag{A.13}$$

Taking the variation of the dissipation potential, a direct calculation allows us to identify $\tilde{\boldsymbol{\sigma}}^{\alpha} = 2\eta d^{\alpha\beta}\boldsymbol{g}_{\beta}$. Similarly, we can identify the component due to inextensibility as $\bar{\boldsymbol{\sigma}}^{\alpha} = \sigma g^{\alpha\beta}\boldsymbol{g}_{\beta}$. These equations above specify the total stress vectors $\boldsymbol{\sigma}^{\alpha} = \hat{\boldsymbol{\sigma}}^{\alpha} + \tilde{\boldsymbol{\sigma}}^{\alpha} + \bar{\boldsymbol{\sigma}}^{\alpha}$ for the protein-membrane system. A calculation shows that the tangential and normal components of the equation $\boldsymbol{\sigma}^{\alpha}_{;\alpha} + p\boldsymbol{n} = \boldsymbol{0}$ coincide with the tangential and normal statements of force balance in Eqs. (2.30) and (2.33).

A.2 Stability Analysis

We summarize here the classical linearized stability analysis around a flat square membrane Γ_0 of lateral size L covered with homogeneous distribution of proteins with area fraction $\bar{\phi}$. We analyze stability of this homogeneous equilibrium configuration for perturbations in shape and protein density. Placing the flat membrane in the $x-y$ plane and considering shape perturbations described by a Monge parametrization, $\boldsymbol{r} = x\mathbf{i}+y\mathbf{j}+h(x,y)\mathbf{k}$, the areal stretch ratio can be computed as

$$J = \sqrt{1+|\nabla h|^2}. \tag{A.14}$$

A perturbation in height of the membrane results in changes in local area and balance of mass of proteins requires that the area fraction of proteins should

reduce to $\bar{\phi}/J$. We consider density perturbations about $\bar{\phi}/J$ to uncouple them from the perturbations in height. We thus express perturbed area-fractions as

$$\tilde{\phi} = \frac{\bar{\phi}}{J} + \phi, \tag{A.15}$$

where ϕ is the perturbation.

Expressing the free energy of Section 2.2 in the reference configuration Γ_0

$$\begin{aligned}\tilde{\mathcal{E}} = \int_{\Gamma_0} \Big\{ &\frac{\kappa}{2}(H - \bar{C}\tilde{\phi})^2 + \frac{k_B T}{a_p}[\tilde{\phi}\log\tilde{\phi} + (\phi_m - \tilde{\phi})\log(\phi_m - \tilde{\phi})] \\ &+ \frac{1}{2a_p}\chi\tilde{\phi}^2 + \frac{\Lambda}{2a_p}|\nabla\tilde{\phi}|^2 + \frac{\mu_0}{a_p}\tilde{\phi}\Big\} J\,dx\,dy + \int_{\Gamma_0}\sigma J\,dx\,dy,\end{aligned} \tag{A.16}$$

and expanding it up to second order in ϕ and h we obtain

$$\delta^2\mathcal{E} = \int_{\Gamma_0}\left\{\frac{\kappa}{2}(\Delta h)^2 + \sigma^{\text{eff}}\frac{|\nabla h|^2}{2} - \kappa(\Delta h)\bar{C}\phi + \frac{a^{\text{eff}}}{2a_p}\phi^2 + \frac{\Lambda}{2a_p}|\nabla\phi|^2\right\} dx\,dy, \tag{A.17}$$

where σ^{eff} and a^{eff} are the effective surface tension and self interaction of proteins defined in Eqs. (2.32) and (4.2). To evaluate the integral in Eq. (A.17), we Fourier transform the perturbations to write

$$h = \sum_{\boldsymbol{q}} h_{\boldsymbol{q}} e^{i\boldsymbol{q}\cdot\boldsymbol{r}_0}, \quad \phi = \sum_{\boldsymbol{q}} \phi_{\boldsymbol{q}} e^{i\boldsymbol{q}\cdot\boldsymbol{r}_0} \tag{A.18}$$

for $\boldsymbol{r}_0 = x\mathbf{i} + y\mathbf{j}$ and $\boldsymbol{q} = \frac{2\pi}{L}\{n_x, n_y\}$ where $n_x, n_y \in \mathbb{Z}$, leading to

$$\begin{aligned}\delta^2\mathcal{E} = L^2\sum_{\boldsymbol{q}}\Bigg[&\left(\frac{\kappa}{2}q^4\right)h_{\boldsymbol{q}}h_{-\boldsymbol{q}} + \left(\frac{\sigma^{\text{eff}}}{2}q^2\right)h_{\boldsymbol{q}}h_{-\boldsymbol{q}} + \left(\frac{\kappa\bar{C}q^2}{2}\right)(h_{\boldsymbol{q}}\phi_{-\boldsymbol{q}} + h_{-\boldsymbol{q}}\phi_{\boldsymbol{q}}) \\ &+ \left(\frac{a^{\text{eff}}}{2a_p}\right)\phi_{\boldsymbol{q}}\phi_{-\boldsymbol{q}} + \left(\frac{\Lambda}{2a_p}q^2\right)\phi_{\boldsymbol{q}}\phi_{-\boldsymbol{q}}\Bigg].\end{aligned} \tag{A.19}$$

and further to

$$\delta^2\mathcal{E} = L^2\sum_{\boldsymbol{q}} \boldsymbol{p}_{\boldsymbol{q}}^* \cdot \boldsymbol{A}\boldsymbol{p}_{\boldsymbol{q}}, \tag{A.20}$$

where $\boldsymbol{p}_{\boldsymbol{q}} = \{h_{\boldsymbol{q}}, \phi_{\boldsymbol{q}}\}$, $\boldsymbol{p}_{\boldsymbol{q}}^*$ its complex conjugate and $\boldsymbol{A} = \begin{bmatrix} \frac{\kappa q^4 + \sigma^{\text{eff}} q^2}{2} & \frac{\kappa\bar{C}q^2}{2} \\ \frac{\kappa\bar{C}q^2}{2} & \frac{a^{\text{eff}} + \Lambda q^2}{2a_p} \end{bmatrix}$. Unstable modes can develop when this matrix ceases to be positive definite. Obvious conditions for instability are

$\sigma^{\text{eff}} < 0$ (Euler buckling) and $a^{\text{eff}} < 0$ (purely chemical phase separation). More interesting chemo-mechanical modes of instability develop when both of these quantities are positive but $\det(A) < 0$ or

$$(\kappa q^4 + \sigma^{\text{eff}} q^2)(a^{\text{eff}} + \Lambda q^2)/a_p - \kappa^2 \bar{C}^2 q^4 \leq 0. \tag{A.21}$$

Since $\sigma^{\text{eff}}, a^{\text{eff}} > 0$, for real unstable modes to exist we require that

$$\kappa|\bar{C}| - \sqrt{\kappa(a^{\text{eff}}/a_p)} \geq \sqrt{\sigma^{\text{eff}}\Lambda/a_p}. \tag{A.22}$$

A similar analysis applies to the free energy discussed in Section 4.5, where now

$$\begin{aligned}\tilde{\mathcal{E}} = \int_{\Gamma_0} \Bigg\{ &\frac{\kappa}{2} H^2 + \frac{\bar{\kappa}_p \tilde{\phi}}{2}(H - C_p)^2 + \frac{k_B T}{a_p}[\tilde{\phi}\log\tilde{\phi} + (\phi_m - \tilde{\phi})\log(\phi_m - \tilde{\phi})] \\ &+ \frac{1}{2a_p}\chi\tilde{\phi}^2 + \frac{\Lambda}{2a_p}|\nabla\tilde{\phi}|^2 + \frac{\mu_0}{a_p}\tilde{\phi}\Bigg\} J\,dx\,dy + \int_{\Gamma_0} \sigma J\,dx\,dy.\end{aligned} \tag{A.23}$$

The second variation has the same structure as Eq. (A.17), the difference being in the interpretation of the coefficients. Now, we have

$$\delta^2\mathcal{E} = \int_{\Gamma_0} \left\{ \frac{\kappa + \bar{\kappa}_p\bar{\phi}}{2}(\Delta h)^2 + \sigma^{\text{eff}}\frac{|\nabla h|^2}{2} - \bar{\kappa}_p(\Delta h)C_p\phi + \frac{a^{\text{eff}}}{2a_p}\phi^2 + \frac{\Lambda}{2a_p}|\nabla\phi|^2 \right\} dx\,dy, \tag{A.24}$$

where

$$\begin{aligned}\sigma^{\text{eff}} &= \sigma + \frac{k_B T}{a_p}[\phi_m \log(\phi_m - \bar{\phi})] - \frac{\chi}{2a_p}\bar{\phi}^2 \\ a^{\text{eff}} &= \chi + k_B T \frac{\phi_m}{(\phi_m - \bar{\phi})\bar{\phi}}.\end{aligned} \tag{A.25}$$

Following the same procedure as before, we obtain the following condition for a chemo-mechanical instability

$$\bar{\kappa}_p|\bar{C}_p| - \sqrt{(\kappa + \bar{\kappa}_p\bar{\phi})(a^{\text{eff}}/a_p)} \geq \sqrt{\sigma^{\text{eff}}\Lambda/a_p}. \tag{A.26}$$

Qualitatively this condition is similar to that in Eq. (A.26). However, there is one subtle difference since now a^{eff} and σ^{eff} are independent of the spontaneous curvature of the proteins, which was not the case before.

Bibliography

[1] A.-L. Le Roux, C. Tozzi, N. Walani, X. Quiroga, D. Zalvidea, X. Trepat, M. Staykova, M. Arroyo, and P. Roca-Cusachs, "Dynamic mechanochemical feedback between curved membranes and bar protein self-organization," *bioRxiv*, 2020.

[2] E. S. Nascimento, P. Palffy-Muhoray, J. M. Taylor, E. G. Virga, and X. Zheng, "Density functional theory for dense nematic liquid crystals with steric interactions," *Physical Review E*, vol. 96, no. 2, p. 022704, 2017.

[3] B. Alberts, D. Bray, K. Hopkin, A. D. Johnson, J. Lewis, M. Raff, K. Roberts, and P. Walter, *Essential cell biology*. Garland Science, 2013.

[4] Y. Shibata, J. Hu, M. M. Kozlov, and T. A. Rapoport, "Mechanisms Shaping the Membranes of Cellular Organelles," *Annual Review of Cell and Developmental Biology*, vol. 25, no. 1, pp. 329–354, 2009.

[5] B. Sinha, D. Köster, R. Ruez, P. Gonnord, M. Bastiani, D. Abankwa, R. V. Stan, G. Butler-Browne, B. Vedie, L. Johannes, N. Morone, R. G. Parton, G. Raposo, P. Sens, C. Lamaze, and P. Nassoy, "Cells Respond to Mechanical Stress by Rapid Disassembly of Caveolae," *Cell*, vol. 144, pp. 402–413, Feb. 2011.

[6] R. Lipowsky, "The conformation of membranes," *Nature*, vol. 349, p. 475, Feb. 1991.

[7] R. Dimova, S. Aranda, N. Bezlyepkina, V. Nikolov, K. A. Riske, and R. Lipowsky, "A practical guide to giant vesicles. Probing the membrane nanoregime via optical microscopy," *Journal of Physics. Condensed Matter: An Institute of Physics Journal*, vol. 18, pp. S1151–1176, July 2006.

[8] T. Baumgart, B. R. Capraro, C. Zhu, and S. L. Das, "Thermodynamics and Mechanics of Membrane Curvature Generation and Sensing by Proteins and Lipids," *Annual Review of Physical Chemistry*, vol. 62, no. 1, pp. 483–506, 2011.

[9] B. J. Peter, H. M. Kent, I. G. Mills, Y. Vallis, P. J. G. Butler, P. R. Evans, and H. T. McMahon, "BAR Domains as Sensors of Membrane Curvature: The Amphiphysin BAR Structure," *Science*, vol. 303, pp. 495–499, Jan. 2004.

[10] M. Hoernke, J. Mohan, E. Larsson, J. Blomberg, D. Kahra, S. Westenhoff, C. Schwieger, and R. Lundmark, "EHD2 restrains dynamics of caveolae by an ATP-dependent, membrane-bound, open conformation," *Proc. Natl. Acad. Sci. U. S. A.*, vol. 114, pp. E4360–E4369, May 2017.

[11] H. T. McMahon and J. L. Gallop, "Membrane curvature and mechanisms of dynamic cell membrane remodelling," *Nature*, vol. 438, p. 590, Dec. 2005.

[12] F. Campelo, H. T. McMahon, and M. M. Kozlov, "The Hydrophobic Insertion Mechanism of Membrane Curvature Generation by Proteins," *Biophysical Journal*, vol. 95, pp. 2325–2339, Sept. 2008.

[13] J. C. Stachowiak, C. C. Hayden, and D. Y. Sasaki, "Steric confinement of proteins on lipid membranes can drive curvature and tubulation," *Proceedings of the National Academy of Sciences*, vol. 107, pp. 7781–7786, Apr. 2010.

[14] I. Tsafrir, Y. Caspi, M.-A. Guedeau-Boudeville, T. Arzi, and J. Stavans, "Budding and Tubulation in Highly Oblate Vesicles by Anchored Am-

phiphilic Molecules," *Physical Review Letters*, vol. 91, p. 138102, Sept. 2003.

[15] C. R. Shurer, J. C.-H. Kuo, L. M. Roberts, J. G. Gandhi, M. J. Colville, T. A. Enoki, H. Pan, J. Su, J. M. Noble, M. J. Hollander, J. P. O'Donnell, R. Yin, K. Pedram, L. Möckl, L. F. Kourkoutis, W. Moerner, C. R. Bertozzi, G. W. Feigenson, H. L. Reesink, and M. J. Paszek, "Physical Principles of Membrane Shape Regulation by the Glycocalyx," *Cell*, May 2019.

[16] P. Sens, L. Johannes, and P. Bassereau, "Biophysical approaches to protein-induced membrane deformations in trafficking," *Current Opinion in Cell Biology*, vol. 20, pp. 476–482, Aug. 2008.

[17] B. Antonny, "Mechanisms of membrane curvature sensing," *Annual review of biochemistry*, vol. 80, pp. 101–123, 2011.

[18] N. S. Hatzakis, V. K. Bhatia, J. Larsen, K. L. Madsen, P.-Y. Bolinger, A. H. Kunding, J. Castillo, U. Gether, P. Hedegård, and D. Stamou, "How curved membranes recruit amphipathic helices and protein anchoring motifs," *Nature Chemical Biology*, vol. 5, pp. 835–841, Nov. 2009.

[19] M. Heinrich, A. Tian, C. Esposito, and T. Baumgart, "Dynamic sorting of lipids and proteins in membrane tubes with a moving phase boundary," *Proceedings of the National Academy of Sciences*, vol. 107, pp. 7208–7213, Apr. 2010.

[20] B. Sorre, A. Callan-Jones, J. Manzi, B. Goud, J. Prost, P. Bassereau, and A. Roux, "Nature of curvature coupling of amphiphysin with membranes depends on its bound density," *Proceedings of the National Academy of Sciences*, vol. 109, pp. 173–178, Jan. 2012.

[21] W.-T. Hsieh, C.-J. Hsu, B. R. Capraro, T. Wu, C.-M. Chen, S. Yang, and T. Baumgart, "Curvature Sorting of Peripheral Proteins on Solid-

Supported Wavy Membranes," *Langmuir*, vol. 28, pp. 12838–12843, Sept. 2012.

[22] M. C. Heinrich, B. R. Capraro, A. Tian, J. M. Isas, R. Langen, and T. Baumgart, "Quantifying Membrane Curvature Generation of Drosophila Amphiphysin N-BAR Domains," *The Journal of Physical Chemistry Letters*, vol. 1, pp. 3401–3406, Nov. 2010.

[23] J. C. Stachowiak, E. M. Schmid, C. J. Ryan, H. S. Ann, D. Y. Sasaki, M. B. Sherman, P. L. Geissler, D. A. Fletcher, and C. C. Hayden, "Membrane bending by protein-protein crowding," *Nature Cell Biology*, vol. 14, pp. 944–949, Sept. 2012.

[24] Z. Shi and T. Baumgart, "Membrane tension and peripheral protein density mediate membrane shape transitions," *Nature Communications*, vol. 6, p. 5974, Jan. 2015.

[25] S. Boulant, C. Kural, J.-C. Zeeh, F. Ubelmann, and T. Kirchhausen, "Actin dynamics counteract membrane tension during clathrin-mediated endocytosis," *Nature Cell Biology*, vol. 13, pp. 1124–1131, Aug. 2011.

[26] D. Kabaso, E. Gongadze, P. Elter, U. van Rienen, J. Gimsa, V. Kralj-Iglič, and A. Iglič, "Attachment of rod-like (BAR) proteins and membrane shape," *Mini Rev. Med. Chem.*, vol. 11, pp. 272–282, Apr. 2011.

[27] T. Kishimoto, Y. Sun, C. Buser, J. Liu, A. Michelot, and D. G. Drubin, "Determinants of endocytic membrane geometry, stability, and scission," *Proceedings of the National Academy of Sciences*, vol. 108, no. 44, pp. E979–E988, 2011.

[28] A. Frost, R. Perera, A. Roux, K. Spasov, O. Destaing, E. H. Egelman, P. De Camilli, and V. M. Unger, "Structural basis of membrane invagination by F-BAR domains," *Cell*, vol. 132, pp. 807–817, Mar. 2008.

[29] C. Mim, H. Cui, J. A. Gawronski-Salerno, A. Frost, E. Lyman, G. A. Voth, and V. M. Unger, "Structural basis of membrane bending by the N-BAR protein endophilin," *Cell*, vol. 149, pp. 137–145, Mar. 2012.

[30] W. M. Henne, E. Boucrot, M. Meinecke, E. Evergren, Y. Vallis, R. Mittal, and H. T. McMahon, "FCHo proteins are nucleators of clathrin-mediated endocytosis," *Science*, vol. 328, pp. 1281–1284, June 2010.

[31] E. Boucrot, A. P. A. Ferreira, L. Almeida-Souza, S. Debard, Y. Vallis, G. Howard, L. Bertot, N. Sauvonnet, and H. T. McMahon, "Endophilin marks and controls a clathrin-independent endocytic pathway," *Nature*, vol. 517, pp. 460–465, Jan. 2015.

[32] C. Zhu, S. L. Das, and T. Baumgart, "Nonlinear sorting, curvature generation, and crowding of endophilin N-BAR on tubular membranes," *Biophysical Journal*, vol. 102, pp. 1837–1845, Apr. 2012.

[33] P. D. Blood and G. A. Voth, "Direct observation of Bin/amphiphysin/Rvs (BAR) domain-induced membrane curvature by means of molecular dynamics simulations," *Proceedings of the National Academy of Sciences*, vol. 103, pp. 15068–15072, Oct. 2006.

[34] H. Yu and K. Schulten, "Membrane Sculpting by F-BAR Domains Studied by Molecular Dynamics Simulations," *PLOS Computational Biology*, vol. 9, p. e1002892, Jan. 2013.

[35] B. J. Reynwar, G. Illya, V. A. Harmandaris, M. M. Müller, K. Kremer, and M. Deserno, "Aggregation and vesiculation of membrane proteins by curvature-mediated interactions," *Nature*, vol. 447, pp. 461–464, May 2007.

[36] M. Simunovic, A. Srivastava, and G. A. Voth, "Linear aggregation of proteins on the membrane as a prelude to membrane remodeling," *Proceedings of the National Academy of Sciences of the United States of America*, vol. 110, pp. 20396–20401, Dec. 2013.

[37] H. Noguchi, "Membrane tubule formation by banana-shaped proteins with or without transient network structure," *Scientific Reports*, vol. 6, p. 20935, Feb. 2016.

[38] T. V. Sachin Krishnan, S. L. Das, and P. B. S. Kumar, "Transition from curvature sensing to generation in a vesicle driven by protein binding strength and membrane tension," *Soft Matter*, vol. 15, pp. 2071–2080, 2019.

[39] H. Aranda-Espinoza, A. Berman, N. Dan, P. Pincus, and S. Safran, "Interaction between inclusions embedded in membranes," *Biophysical Journal*, vol. 71, pp. 648–656, Aug. 1996.

[40] P. G. Dommersnes and J.-B. Fournier, "N-body study of anisotropic membrane inclusions: Membrane mediated interactions and ordered aggregation," *European Physical Journal B*, vol. 12, pp. 9–12, Oct. 1999.

[41] F. Bonazzi and T. R. Weikl, "Membrane morphologies induced by arc-shaped scaffolds are determined by arc angle and coverage," *Biophysical journal*, vol. 116, no. 7, pp. 1239–1247, 2019.

[42] C. Hiergeist and R. Lipowsky, "Elastic Properties of Polymer-Decorated Membranes," *Journal de Physique II*, vol. 6, pp. 1465–1481, Oct. 1996.

[43] M. Breidenich, R. R. Netz, and R. Lipowsky, "The shape of polymer-decorated membranes," *Europhysics Letters*, vol. 49, p. 431, Feb. 2000.

[44] K. S. Kim, J. Neu, and G. Oster, "Curvature-Mediated Interactions Between Membrane Proteins," *Biophysical Journal*, vol. 75, pp. 2274–2291, Nov. 1998.

[45] W. Helfrich, "Elastic Properties of Lipid Bilayers: Theory and Possible Experiments," *Zeitschrift für Naturforschung C*, vol. 28, no. 11-12, pp. 693–703, 1973.

[46] P. J. Flory, "Thermodynamics of High Polymer Solutions," *The Journal of Chemical Physics*, vol. 10, pp. 51–61, Jan. 1942.

[47] M. L. Huggins, "Solutions of Long Chain Compounds," *The Journal of Chemical Physics*, vol. 9, pp. 440–440, May 1941.

[48] N. S. Gov, "Guided by curvature: shaping cells by coupling curved membrane proteins and cytoskeletal forces," *Philosophical Transactions of the Royal Society of London. Series B, Biological Sciences*, vol. 373, no. 1747, p. 20170115, 2018.

[49] H. Alimohamadi and P. Rangamani, "Modeling Membrane Curvature Generation due to Membrane Protein Interactions," *Biomolecules*, vol. 8, no. 4, p. 120, 2018.

[50] S. Leibler, "Curvature instability in membranes," *Journal de Physique*, vol. 47, pp. 507–516, Mar. 1986.

[51] J. Agudo-Canalejo and R. Golestanian, "Pattern formation by curvature-inducing proteins on spherical membranes," *New Journal of Physics*, vol. 19, p. 125013, Dec. 2017.

[52] P. Singh, P. Mahata, T. Baumgart, and S. L. Das, "Curvature sorting of proteins on a cylindrical lipid membrane tether connected to a reservoir," *Physical Review E*, vol. 85, p. 051906, May 2012.

[53] C. Prévost, H. Zhao, J. Manzi, E. Lemichez, P. Lappalainen, A. Callan-Jones, and P. Bassereau, "IRSp53 senses negative membrane curvature and phase separates along membrane tubules," *Nature Communications*, vol. 6, p. 8529, Oct. 2015.

[54] S. Katz and S. Givli, "Curvature-induced spatial ordering of composition in lipid membranes," *Computational and Mathematical Methods in Medicine*, vol. 2017, 2017.

[55] Y.-C. Su and J. Z. Y. Chen, "A model of vesicle tubulation and pearling induced by adsorbing particles," *Soft Matter*, vol. 11, pp. 4054–4060, May 2015.

[56] W. Góźdź, "Shape transformation of lipid vesicles induced by diffusing macromolecules," *The Journal of Chemical Physics*, vol. 134, p. 024110, Jan. 2011.

[57] A. Agrawal and D. J. Steigmann, "A model for surface diffusion of transmembrane proteins on lipid bilayers," *Zeitschrift für angewandte Mathematik und Physik*, vol. 62, p. 549, May 2011.

[58] A. Arkhipov, Y. Yin, and K. Schulten, "Membrane-bending mechanism of amphiphysin n-bar domains," *Biophysical journal*, vol. 97, no. 10, pp. 2727–2735, 2009.

[59] H. Yu and K. Schulten, "Membrane sculpting by f-bar domains studied by molecular dynamics simulations," *PLoS Comput Biol*, vol. 9, no. 1, p. e1002892, 2013.

[60] N. Ramakrishnan, P. S. Kumar, and J. H. Ipsen, "Membrane-mediated aggregation of curvature-inducing nematogens and membrane tubulation," *Biophysical journal*, vol. 104, no. 5, pp. 1018–1028, 2013.

[61] N. Ramakrishnan, P. S. Kumar, and R. Radhakrishnan, "Mesoscale computational studies of membrane bilayer remodeling by curvature-inducing proteins," *Physics reports*, vol. 543, no. 1, pp. 1–60, 2014.

[62] H. Noguchi, "Shape transition from elliptical to cylindrical membrane tubes induced by chiral crescent-shaped protein rods," *Scientific reports*, vol. 9, no. 1, pp. 1–7, 2019.

[63] W. Pezeshkian and J. H. Ipsen, "Fluctuations and conformational stability of a membrane patch with curvature inducing inclusions," *Soft matter*, vol. 15, no. 48, pp. 9974–9981, 2019.

[64] D. Kabaso, N. Bobrovska, W. Góźdź, N. Gov, V. Kralj-Iglič, P. Veranič, and A. Iglič, "On the role of membrane anisotropy and bar proteins in the stability of tubular membrane structures," *Journal of biomechanics*, vol. 45, no. 2, pp. 231–238, 2012.

[65] N. Walani, J. Torres, and A. Agrawal, "Anisotropic spontaneous curvatures in lipid membranes," *Physical Review. E, Statistical, Nonlinear, and Soft Matter Physics*, vol. 89, p. 062715, June 2014.

[66] J.-B. Fournier and P. Galatola, "Bilayer membranes with 2d-nematic order of the surfactant polar heads," *Brazilian journal of physics*, vol. 28, no. 4, pp. 00–00, 1998.

[67] S. Penič, L. Mesarec, M. Fošnarič, L. Mrówczyńska, H. Hägerstrand, V. Kralj-Iglič, and A. Iglič, "Budding and fission of membrane vesicles: a mini review," *Frontiers in Physics*, vol. 8, p. 342, 2020.

[68] M. Doi, "OnsagerÕs variational principle in soft matter," *Journal of Physics: Condensed Matter*, vol. 23, no. 28, p. 284118, 2011.

[69] M. Arroyo, N. Walani, A. Torres-Sánchez, and D. Kaurin, "Onsager's variational principle in soft matter: Introduction and application to the dynamics of adsorption of proteins onto fluid membranes," in *The Role of Mechanics in the Study of Lipid Bilayers*, pp. 287–332, Springer, 2018.

[70] M. A. Peletier, "Variational modelling: Energies, gradient flows, and large deviations," *arXiv preprint arXiv:1402.1990*, 2014.

[71] K. L. Madsen, V. K. Bhatia, U. Gether, and D. Stamou, "Bar domains, amphipathic helices and membrane-anchored proteins use the same mechanism to sense membrane curvature," *FEBS letters*, vol. 584, no. 9, pp. 1848–1855, 2010.

[72] W.-T. Hsieh, C.-J. Hsu, B. R. Capraro, T. Wu, C.-M. Chen, S. Yang, and T. Baumgart, "Curvature sorting of peripheral proteins on solid-supported wavy membranes," *Langmuir*, vol. 28, no. 35, pp. 12838–12843, 2012.

[73] M. Galic, S. Jeong, F.-C. Tsai, L.-M. Joubert, Y. I. Wu, K. M. Hahn, Y. Cui, and T. Meyer, "External push and internal pull forces recruit

curvature-sensing n-bar domain proteins to the plasma membrane," *Nature cell biology*, vol. 14, no. 8, pp. 874–881, 2012.

[74] M. Rahimi and M. Arroyo, "Shape dynamics, lipid hydrodynamics, and the complex viscoelasticity of bilayer membranes," *Physical Review E*, vol. 86, p. 011932, July 2012.

[75] A. Torres-Sánchez, D. Millán, and M. Arroyo, "Modelling fluid deformable surfaces with an emphasis on biological interfaces," *arXiv preprint arXiv:1812.02837*, Dec. 2018.

[76] M. M. Kozlov, F. Campelo, N. Liska, L. V. Chernomordik, S. J. Marrink, and H. T. McMahon, "Mechanisms shaping cell membranes," *Current Opinion in Cell Biology*, vol. 29, pp. 53–60, Aug. 2014.

[77] M. d. Carmo, *Riemannian Geometry*. Mathematics: Theory & Applications, Birkhäuser, 1992.

[78] J. E. Marsden and T. J. R. Hughes, *Mathematical Foundations of Elasticity*. Dover, 1994.

[79] M. Doi, *Soft Matter Physics*. Oxford, New York: Oxford University Press, July 2013.

[80] D. J. Steigmann, "Fluid Films with Curvature Elasticity," *Archive for Rational Mechanics and Analysis*, vol. 150, pp. 127–152, Dec. 1999.

[81] J. Carr, M. E. Gurtin, and M. Slemrod, "Structured phase transitions on a finite interval," *Archive for Rational Mechanics and Analysis*, vol. 86, pp. 317–351, Dec. 1984.

[82] Zheng Q.S., "Two-dimensional tensor function representation for all kinds of material symmetry," *Proceedings of the Royal Society of London. Series A: Mathematical and Physical Sciences*, vol. 443, pp. 127–138, Oct. 1993.

[83] M. Arroyo and A. DeSimone, "Relaxation dynamics of fluid membranes," *Physical Review E*, vol. 79, p. 031915, Mar. 2009.

[84] U. Seifert and S. A. Langer, "Viscous Modes of Fluid Bilayer Membranes," *Europhysics Letters (EPL)*, vol. 23, pp. 71–76, July 1993.

[85] M. Arroyo, A. DeSimone, and L. Heltai, "The role of membrane viscosity in the dynamics of fluid membranes," *arXiv preprint arXiv:1007.4934*, 2010.

[86] W. Kukulski, M. Schorb, M. Kaksonen, and J. A. G. Briggs, "Plasma membrane reshaping during endocytosis is revealed by time-resolved electron tomography," *Cell*, vol. 150, pp. 508–520, Aug. 2012.

[87] R. G. Parton and M. A. Pozo, "Caveolae as plasma membrane sensors, protectors and organizers," *Nature Reviews Molecular Cell Biology*, vol. 14, pp. 98–112, 2013.

[88] P. M. Naghdi, "The Theory of Shells and Plates," in *Linear Theories of Elasticity and Thermoelasticity: Linear and Nonlinear Theories of Rods, Plates, and Shells* (C. Truesdell, ed.), pp. 425–640, Berlin, Heidelberg: Springer Berlin Heidelberg, 1973.

[89] A. Agrawal and D. J. Steigmann, "Boundary-value problems in the theory of lipid membranes," *Continuum Mechanics and Thermodynamics*, vol. 21, pp. 57–82, June 2009.

[90] C. M. Elliott and Z. Songmu, "On the Cahn-Hilliard equation," *Archive for Rational Mechanics and Analysis*, vol. 96, pp. 339–357, Dec. 1986.

[91] A. Novick-Cohen and L. A. Segel, "Nonlinear aspects of the Cahn-Hilliard equation," *Physica D: Nonlinear Phenomena*, vol. 10, pp. 277–298, Mar. 1984.

[92] M. Rahimi, A. DeSimone, and M. Arroyo, "Curved fluid membranes behave laterally as effective viscoelastic media," *Soft Matter*, vol. 9, pp. 11033–11045, Nov. 2013.

[93] P. G. Saffman and M. Delbrück, "Brownian motion in biological membranes," *Proceedings of the National Academy of Sciences*, vol. 72, pp. 3111–3113, Aug. 1975.

[94] L. Piegl and W. Tiller, *The NURBS Book*. Monographs in Visual Communication, Berlin Heidelberg: Springer-Verlag, 1995.

[95] A. Buffa, C. d. Falco, and G. Sangalli, "IsoGeometric Analysis: Stable elements for the 2d Stokes equation," *International Journal for Numerical Methods in Fluids*, vol. 65, no. 11-12, pp. 1407–1422, 2011.

[96] R. A. Sauer, T. X. Duong, K. K. Mandadapu, and D. J. Steigmann, "A stabilized finite element formulation for liquid shells and its application to lipid bilayers," *Journal of Computational Physics*, vol. 330, pp. 436–466, Feb. 2017.

[97] J. C. Stachowiak, C. C. Hayden, and D. Y. Sasaki, "Steric confinement of proteins on lipid membranes can drive curvature and tubulation," *Proceedings of the National Academy of Sciences*, vol. 107, no. 17, pp. 7781–7786, 2010.

[98] J. C. Stachowiak, E. M. Schmid, C. J. Ryan, H. S. Ann, D. Y. Sasaki, M. B. Sherman, P. L. Geissler, D. A. Fletcher, and C. C. Hayden, "Membrane bending by protein–protein crowding," *Nature cell biology*, vol. 14, no. 9, pp. 944–949, 2012.

[99] F. Campelo and A. Hernández-Machado, "Model for Curvature-Driven Pearling Instability in Membranes," *Physical Review Letters*, vol. 99, p. 088101, Aug. 2007.

[100] N. Khalifat, M. Rahimi, A.-F. Bitbol, M. Seigneuret, J.-B. Fournier, N. Puff, M. Arroyo, and M. I. Angelova, "Interplay of Packing and Flip-flop in Local Bilayer Deformation. How Phosphatidylglycerol Could Rescue Mitochondrial Function in a Cardiolipin-deficient Yeast Mutant," *Biophysical Journal*, vol. 107, pp. 879–890, Aug. 2014.

[101] A. Roux, G. Koster, M. Lenz, B. Sorre, J.-B. Manneville, P. Nassoy, and P. Bassereau, "Membrane curvature controls dynamin polymerization," *Proceedings of the National Academy of Sciences*, vol. 107, pp. 4141–4146, Mar. 2010.

[102] H. J. Lee, E. L. Peterson, R. Phillips, W. S. Klug, and P. A. Wiggins, "Membrane shape as a reporter for applied forces," *Proceedings of the National Academy of Sciences*, vol. 105, pp. 19253–19257, Dec. 2008.

[103] G. J. Doherty and H. T. McMahon, "Mechanisms of Endocytosis," *Annual Review of Biochemistry*, vol. 78, no. 1, pp. 857–902, 2009.

[104] J. Weinberg and D. G. Drubin, "Clathrin-mediated endocytosis in budding yeast," *Trends in Cell Biology*, vol. 22, pp. 1–13, Jan. 2012.

[105] F. M. Hochmuth, J. Y. Shao, J. Dai, and M. P. Sheetz, "Deformation and flow of membrane into tethers extracted from neuronal growth cones," *Biophysical Journal*, vol. 70, pp. 358–369, Jan. 1996.

[106] P. Sens and M. S. Turner, "Budded membrane microdomains as tension regulators," *Physical Review. E, Statistical, Nonlinear, and Soft Matter Physics*, vol. 73, p. 031918, Mar. 2006.

[107] N. Walani, J. Torres, and A. Agrawal, "Endocytic proteins drive vesicle growth via instability in high membrane tension environment," *Proceedings of the National Academy of Sciences*, vol. 112, pp. E1423–E1432, Mar. 2015.

[108] M. G. Hilgers and A. C. Pipkin, "Energy-minimizing deformations of elastic sheets with bending stiffness," *Journal of Elasticity*, vol. 31, pp. 125–139, May 1993.

[109] L. Onsager, "The effects of shape on the interaction of colloidal particles," *Annals of the New York Academy of Sciences*, vol. 51, no. 4, pp. 627–659, 1949.

[110] X. Zheng and P. Palffy-Muhoray, "Distance of closest approach of two arbitrary hard ellipses in two dimensions," *Physical Review E*, vol. 75, no. 6, p. 061709, 2007.

[111] J. Vieillard-Baron, "Phase transitions of the classical hard-ellipse system," *The Journal of Chemical Physics*, vol. 56, no. 10, pp. 4729–4744, 1972.

[112] J. M. Taylor, "An analysis of equilibria in dense nematic liquid crystals," *SIAM Journal on Mathematical Analysis*, vol. 50, no. 2, pp. 1918–1957, 2018.

[113] J. Zimmerberg and M. M. Kozlov, "How proteins produce cellular membrane curvature," *Nature reviews Molecular cell biology*, vol. 7, no. 1, pp. 9–19, 2006.

[114] R. Lipowsky, "Bending of membranes by anchored polymers," *Europhysics Letters (EPL)*, vol. 30, pp. 197–202, May 1995.

[115] C. Tozzi, N. Walani, and M. Arroyo, "Out-of-equilibrium mechanochemistry and self-organization of fluid membranes interacting with curved proteins," *New journal of physics*, vol. 21, no. 9, p. 093004, 2019.

[116] J. R. Frank and M. Kardar, "Defects in nematic membranes can buckle into pseudospheres," *Phys. Rev. E*, vol. 77, p. 041705, Apr 2008.

[117] E. C. Gartland and E. G. Virga, "Minimum principle for indefinite mean-field free energies," *Archive for rational mechanics and analysis*, vol. 196, no. 1, pp. 143–189, 2010.

[118] M. Simunovic, C. Prévost, A. Callan-Jones, and P. Bassereau, "Physical basis of some membrane shaping mechanisms," *Philosophical Transactions of the Royal Society A: Mathematical, Physical and Engineering Sciences*, vol. 374, no. 2072, p. 20160034, 2016.

[119] C. Prévost, H. Zhao, J. Manzi, E. Lemichez, P. Lappalainen, A. Callan-Jones, and P. Bassereau, "Irsp53 senses negative membrane curvature and phase separates along membrane tubules," *Nature communications*, vol. 6, no. 1, pp. 1–11, 2015.

[120] H. Noguchi, "Formation of polyhedral vesicles and polygonal membrane tubes induced by banana-shaped proteins," *The Journal of chemical physics*, vol. 143, no. 24, p. 243109, 2015.

[121] A. Frost, V. M. Unger, and P. De Camilli, "The bar domain superfamily: membrane-molding macromolecules," *Cell*, vol. 137, no. 2, pp. 191–196, 2009.

[122] C. Mim, H. Cui, J. A. Gawronski-Salerno, A. Frost, E. Lyman, G. A. Voth, and V. M. Unger, "Structural basis of membrane bending by the n-bar protein endophilin," *Cell*, vol. 149, no. 1, pp. 137–145, 2012.

[123] Z. Shi and T. Baumgart, "Membrane tension and peripheral protein density mediate membrane shape transitions," *Nature communications*, vol. 6, no. 1, pp. 1–8, 2015.

[124] B. Sorre, A. Callan-Jones, J. Manzi, B. Goud, J. Prost, P. Bassereau, and A. Roux, "Nature of curvature coupling of amphiphysin with membranes depends on its bound density," *Proceedings of the National Academy of Sciences*, vol. 109, no. 1, pp. 173–178, 2012.

[125] X. Li, L. Matino, W. Zhang, L. Klausen, A. F. McGuire, C. Lubrano, W. Zhao, F. Santoro, and B. Cui, "A nanostructure platform for live-cell manipulation of membrane curvature," *Nature protocols*, vol. 14, no. 6, p. 1772, 2019.

[126] M. Staykova, M. Arroyo, M. Rahimi, and H. A. Stone, "Confined bilayers passively regulate shape and stress," *Physical review letters*, vol. 110, no. 2, p. 028101, 2013.

[127] A. J. Kosmalska, L. Casares, A. Elosegui-Artola, J. J. Thottacherry, R. Moreno-Vicente, V. González-Tarragó, M. Á. Del Pozo, S. Mayor, M. Arroyo, D. Navajas, *et al.*, "Physical principles of membrane remodelling during cell mechanoadaptation," *Nature communications*, vol. 6, no. 1, pp. 1–11, 2015.

[128] E. Boucrot, A. P. Ferreira, L. Almeida-Souza, S. Debard, Y. Vallis, G. Howard, L. Bertot, N. Sauvonnet, and H. T. McMahon, "Endophilin marks and controls a clathrin-independent endocytic pathway," *Nature*, vol. 517, no. 7535, pp. 460–465, 2015.

[129] H.-F. Renard, M. Simunovic, J. Lemière, E. Boucrot, M. D. Garcia-Castillo, S. Arumugam, V. Chambon, C. Lamaze, C. Wunder, A. K. Kenworthy, *et al.*, "Endophilin-a2 functions in membrane scission in clathrin-independent endocytosis," *Nature*, vol. 517, no. 7535, pp. 493–496, 2015.

[130] H. Noguchi, "Membrane tubule formation by banana-shaped proteins with or without transient network structure," *Scientific reports*, vol. 6, p. 20935, 2016.

[131] C. Tozzi, N. Walani, A.-L. Le Roux, P. Roca-Cusachs, and M. Arroyo, "A theory of ordering of elongated and curved proteins on membranes driven by density and curvature," *Soft Matter*, 2021.

[132] D. Kaurin and M. Arroyo, "Surface tension controls the hydraulic fracture of adhesive interfaces bridged by molecular bonds," *Physical review letters*, vol. 123, no. 22, p. 228102, 2019.

[133] J. Feng, C. V. Chaubal, and L. G. Leal, "Closure approximations for the doi theory: Which to use in simulating complex flows of liquid-crystalline polymers?," *Journal of Rheology*, vol. 42, no. 5, pp. 1095–1119, 1998.

[134] M. Simunovic, E. Evergren, I. Golushko, C. Prévost, H.-F. Renard, L. Johannes, H. T. McMahon, V. Lorman, G. A. Voth, and P. Bassereau,

"How curvature-generating proteins build scaffolds on membrane nanotubes," *Proceedings of the National Academy of Sciences*, vol. 113, no. 40, pp. 11226–11231, 2016.

[135] M. Rahimi and M. Arroyo, "Shape dynamics, lipid hydrodynamics, and the complex viscoelasticity of bilayer membranes," *Physical review E*, vol. 86, no. 1, p. 011932, 2012.

[136] F. Campelo and A. Hernández-Machado, "Model for curvature-driven pearling instability in membranes," *Physical review letters*, vol. 99, no. 8, p. 088101, 2007.

[137] I. Tsafrir, D. Sagi, T. Arzi, M.-A. Guedeau-Boudeville, V. Frette, D. Kandel, and J. Stavans, "Pearling instabilities of membrane tubes with anchored polymers," *Physical review letters*, vol. 86, no. 6, p. 1138, 2001.

[138] M. Simunovic and G. A. Voth, "Membrane tension controls the assembly of curvature-generating proteins," *Nature communications*, vol. 6, no. 1, pp. 1–8, 2015.

[139] C. Prévost, F.-C. Tsai, P. Bassereau, and M. Simunovic, "Pulling membrane nanotubes from giant unilamellar vesicles," *JoVE (Journal of Visualized Experiments)*, no. 130, p. e56086, 2017.

[140] M. Simunovic, C. Mim, T. C. Marlovits, G. Resch, V. M. Unger, and G. A. Voth, "Protein-mediated transformation of lipid vesicles into tubular networks," *Biophysical journal*, vol. 105, no. 3, pp. 711–719, 2013.

[141] G. S. Ayton, E. Lyman, V. Krishna, R. D. Swenson, C. Mim, V. M. Unger, and G. A. Voth, "New insights into bar domain-induced membrane remodeling," *Biophysical journal*, vol. 97, no. 6, pp. 1616–1625, 2009.

[142] I. Raote, M. Chabanon, N. Walani, M. Arroyo, M. F. Garcia-Parajo, V. Malhotra, and F. Campelo, "A physical mechanism of tango1-mediated bulky cargo export," *Elife*, vol. 9, p. e59426, 2020.

[143] R. Capovilla and J. Guven, "Stresses in lipid membranes," *Journal of Physics A: Mathematical and General*, vol. 35, pp. 6233–6247, July 2002.